

Universität
Rostock



Traditio et Innovatio

Dissertation

Hyperfine interactions in nanostructured iron oxide composites

Kerstin Witte

born 10/21/1985 in Finsterwalde

University of Rostock
Faculty of Mathematical and Natural Sciences
Institute of Physics - Physics of New Materials

Rostock, 2015

Reviewer:

Professor Dr. Eberhard Burkel, University of Rostock, Faculty of Mathematical and Natural Sciences, Institute of Physics - Physics of New Materials

Prof. Dr. Mohsen Abd-Elmeguid, University of Cologne, Faculty of Mathematics and Natural Sciences, Department of Physics - High Pressure Group

Date of submission: 23rd of January 2015

Date of defense: 11th of May 2015

Abstract

The grain sizes within a permanent magnetic material determine the coercivity of the material. It increases with decreasing grain sizes. Since nowadays, the rather novel field assisted sintering technology is offering the unique possibility to consolidate materials while maintaining the nanostructures of the precursor materials, this method can be used to tailor the grain sizes in sintered permanent bulk magnets. Since the physical properties of the bulk material changes, these changes have to be originated by variations of the electronic structure of the material. In the case of iron rich magnetic materials, Mößbauer spectroscopy is an ideal tool to detect such variations in the electronic environment. It is demonstrated that in the case of nanostructured iron oxide bulk materials, the hyperfine interactions of magnetite change due to the small sizes of the grains below 80 nm.

Zusammenfassung

Die Korngrößen von permanentmagnetischen Materialien bestimmen dessen Koerzitivfeld. Es nimmt mit abnehmender Korngröße zu. Die eher neue Technologie des feld-gestützten Sinterns eröffnet die einzigartige Möglichkeit, Materialien zu verdichten während die Nanostruktur des Ausgangsmaterials erhalten bleibt, sodass die Korngrößen in den Permanentmagneten maßgeschneidert werden können. Aufgrund der Tatsache, dass sich die physikalischen Eigenschaften des Festkörpers ändern, muss es zu Modifikationen in der elektronischen Struktur des Materials kommen. Im Fall von eisenhaltigen magnetischen Materialien ist die Mößbauer Spektroskopie ein ideales Werkzeug, um diese Veränderungen der elektronischen Struktur zu detektieren. Es wird gezeigt, dass es zu Veränderungen der Hyperfeinparameter für nanostrukturierte Eisenoxidfestkörper aufgrund der Reduzierung der Korngröße unter 80 nm kommt.

Contents

1	Introduction	3
1.1	Motivation	3
1.2	Iron oxides	5
1.3	Field assisted sintering technique	7
1.3.1	Sintering mechanisms	8
2	Experimental methods and set-ups	9
2.1	Scanning electron microscopy	9
2.2	X-ray diffraction	10
2.2.1	Theoretical background	10
2.2.2	Rietveld refinement combined with Fourier analysis	13
2.2.3	Experimental set-up	15
2.3	Möbbauser spectroscopy	16
2.3.1	Möbbauser effect	16
2.3.2	Hyperfine interactions	18
2.3.3	Line shape	23
2.3.4	Experimental set-up	24
3	Interpretation of Möbbauser spectra	27
3.1	Comparison of fitting models	27
3.1.1	Interpretation of Möbbauser spectra from magnetite	27
3.1.2	High energy X-ray diffraction study	28
3.1.3	Möbbauser spectroscopy	29
3.1.4	Lorentz model	31
3.1.5	Voigt model	33
3.1.6	Extended Voigt based model	34
3.2	Magnetite bulk material	41
3.3	Time dependant hyperfine interactions	42
3.3.1	Hyperfine interactions of magnetite in the blocked state	47
3.3.2	Hyperfine interactions of magnetite in the superparamagnetic state	50
3.4	Time independent hyperfine interactions	52
4	Nanostructured iron oxide composites	53
4.1	Systematics	53
4.2	Composites sintered from hematite and iron	55
4.2.1	Initial particle size $d = 190$ nm	55
4.2.2	Initial particle size $d = 26$ nm	60
4.3	Composites sintered from magnetite	61
4.3.1	Initial particle size $d = 120$ nm	61
4.3.2	Initial particle size $d = 27$ nm	66

5	Discussion	73
6	Conclusions	85
7	Outlook	87
A	Reference sample and nanoparticles	89
A.1	Reference sample	89
A.2	Nanoparticles	89
B	Precursor materials	91
C	Composites sintered from hematite and iron precursor	95
C.1	Initial particle size $d = 190$ nm	95
C.2	Initial particle size $d = 26$ nm	95
D	Composites sintered from magnetite precursor	109
D.1	Initial particle size $d = 120$ nm	109
D.2	Initial particle size $d = 27$ nm	109
	References	127

Chapter 1

Introduction

1.1 Motivation

Nanostructured materials attracted a lot of attention in the last years due to their unusual chemical and physical properties which are promising for further technological development [1–3]. The properties of these nanostructured materials differ from those of normal bulk materials due to the small particle- or grain sizes which are in the nanometer regime leading to the presence of size and surface effects [1]. For nanoparticles and thin films a broad range of interesting effects like superparamagnetism [4], giant magnetoresistance [5] or increased energy products [6] have been observed.

One major reason for the research in the area of nanostructured magnets originates from the size dependence of the coercivity, which is illustrated in Fig. 1.1. It shows a significant change of the coercivity when the particle size of the material is reduced to the nanometer regime. When the particle size becomes smaller, it is energetically unfavourable to build several domains within the particle. At this point a single domain transition takes place and the particle has its highest coercivity. For a further reduction of the particle size the coercivity decreases drastically until it becomes zero in the superparamagnetic regime.

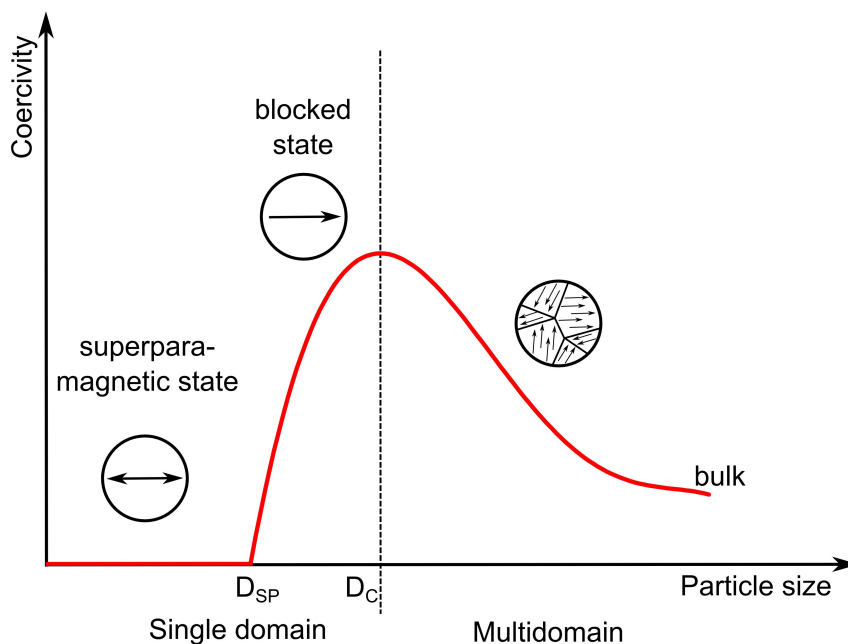


Figure 1.1: Coercivity of magnetic nanoparticles in dependence of the particle size.

This behaviour is well known for magnetic nanoparticles while the behaviour of nanostructured bulk materials is widely unknown. To study changes in the behaviour of

magnetic materials, soft magnetic iron oxides are ideal systems due to their metastability, as well as, due to their large single domain sizes of magnetite and maghemite [7].

The rather novel field assisted sintering technique (FAST) is a promising tool for the consolidation and synthesis of such nanostructured bulk materials. During FAST a pulsed directed current and a mechanical load are applied on precursor powders placed in a graphite die, leading to rapid heating of the powders [8]. Advantages of FAST are short process times and the possibility of maintaining nanostructured grains [8, 9].

First studies on iron oxide systems already showed changes in the coercivity and the saturation magnetisation of the iron oxides for different grain sizes [10–14]. Nevertheless, when the macroscopic properties of a nanostructured composites show modifications compared to the typical bulk behaviour, the local structure in the material has to change. These changes can be originated by the excessive increase of the grain boundaries, which is illustrated in Fig. 1.2. When the grain size of the material is reduced to the nanometer regime, the areas of interfaces increase by several orders of magnitude.

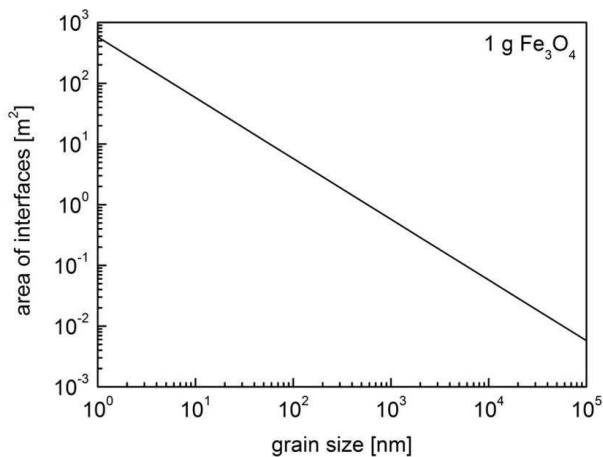


Figure 1.2: Area of interfaces in in one gram magnetite in dependence of grain size.

To study local changes due to an increasing amount of grain boundaries, especially in iron oxides, Mößbauer spectroscopy is the ideal tool since it is sensitive to the local electronic structure at the Mößbauer nucleus [15]. The Mößbauer effect is the recoil-free emission and absorption of γ -rays by a nucleus bound in a solid and it is the basis of Mößbauer spectroscopy. Mößbauer spectroscopy is a local atomic probe tool, which is highly sensitive to the atomic structure and the electric and magnetic properties of the investigated sample. Due to this, it is an excellent

tool to investigate nanostructured materials [15].

Since the interpretation of Mößbauer spectra is not trivial, a detailed discussion of different fitting models of magnetic iron oxide nanoparticles is given and the time dependent spectra of a series of coprecipitated nanoparticles are discussed.

To synthesise nanostructured iron oxides the novel field assisted sintering technique was applied. The iron oxide of interest in this studies was magnetite. For the synthesis of magnetite two different attempts are presented. In the first series, magnetite was synthesised from hematite and iron. In the second series, it was obtained directly from magnetite precursors. All composites were characterised by their composition, crystal unit edges, grain sizes, as well as, by their hyperfine interaction parameters as functions of the sintering temperature. Additionally, the influence of the initial particle sizes used during the consolidation process was investigated. First results of changed hyperfine interaction parameters of nanostructured iron oxide composites in form of bulk materials are presented.

1.2 Iron oxides

Iron oxides are common compounds and widespread in nature and they are of interest in many scientific disciplines. Iron oxides can be described as closed packed arrays of anions where octahedral and tetrahedral interstices are partially filled with iron in di- or trivalent states. The oxides differ mainly in the structural arrangements of their units $\text{Fe}(\text{O}/\text{OH})_6$ or FeO_4 [16]. The compounds of interest in this work are magnetite, hematite, maghemite and wustite, as well as, an additionally used precursor iron. A general overview of these iron oxides and of iron at room temperature is presented in Tab. 1.1.

iron oxide	formula unit	crystal structure	space group	cell parameters [Å]	density [g·cm ⁻³]	magnetism
magnetite	Fe_3O_4	cubic	Fd3m	a=8.39	5.18	ferrimagnetic
hematite	$\alpha\text{-Fe}_2\text{O}_3$	hexagonal	R $\bar{3}c$	a=5.03 c=13.75	5.26	antiferromagnetic (spin canting)
maghemite	$\gamma\text{-Fe}_2\text{O}_3$	cubic	Fd3m	a=8.34	4.87	ferrimagnetic
	$\gamma\text{-Fe}_2\text{O}_3$	tetragonal	P422	a=8.34 c=25.02	4.87	ferrimagnetic
wustite	FeO	cubic	Fm3m	a=4.31	5.95	paramagnetic
iron	Fe	cubic	Im3m	a=2.86	7.87	ferromagnetic

Table 1.1: General overview of iron oxides of interest and iron - formula unit, crystal structure, space group, cell parameters, density and magnetism at room temperature [16–20].

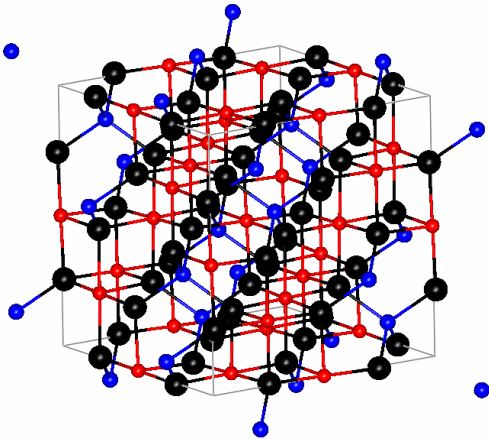


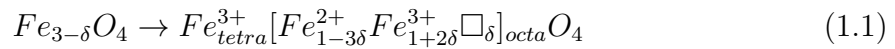
Figure 1.3: Crystal structure of magnetite. Black - oxygen ions, blue - tetrahedral positions of iron ions (A-sites), red - octahedral positions (B-sites).

Magnetite has a cubic unit cell belonging to the space group $\text{Fd}\bar{3}\text{m}$ [18] and a crystal unit edge of $a = 8.39 \text{ \AA}$ [16]. In the stoichiometric spinel, the unit cell contains 32 oxygen atoms. It has 8 equivalent tetrahedral and 16 equivalent octahedral sites which can be occupied by iron atoms, see Fig. 1.3. Magnetite is occupied not only by trivalent but also divalent iron on the octahedral sites. The formula of Fe_3O_4 can also be presented as $(\text{Fe}^{3+})_{\text{tetra}}[\text{Fe}^{3+} + \text{Fe}^{2+}]_{\text{octa}}\text{O}_4^{2-}$. Due to the fast electron hopping of magnetite above the Verwey transition temperature ($\sim 120 \text{ K}$) it can also be presented as $(\text{Fe}^{3+})_{\text{tetra}}[\text{Fe}^{2.5+}]_{\text{octa}}\text{O}_4^{2-}$ [21]. The tetrahedral sites (A-sites, presented in Fig. 1.3 in blue) are only occupied by Fe^{3+} -ions and the octahedral sites (B-sites, presented in Fig. 1.3 in red) are occupied by Fe^{3+} -ions and Fe^{2+} -ions. Due to the rapid electron hopping on magnetite B-sites, a mixed valence state of 2.5+ is observed. This is the origin of the conductivity of magnetite [21].

Furthermore, magnetite can have a wide range of oxidation states which depend on the Fe^{2+} -ion content present in the structure [22]. Therefore, the oxidation state of magnetite directly depends on its stoichiometry and it can be expressed by $x = Fe^{2+}/Fe^{3+}$. For stoichiometric magnetite, $x = 0.5$. When magnetite becomes *nonstoichiometric* x decreases and, for $x = 0$, it is completely oxidised and called *maghemite*. It is worth mentioning that the nonstoichiometric magnetite is also often described as a *solid solution of magnetite and maghemite*.

Maghemite is also characteristic of a cubic unit cell, space group $Fd\bar{3}m$, but the crystal unit edge $a \simeq 8.33 \text{ \AA}$ is slightly smaller than the one of magnetite [16]. It was reported that maghemite can also occur in a different structure as a result of the ordering of the vacancies on the B-sites [23]. Such maghemite with ordered vacancies is characteristic of a tetragonal unit cell belonging to the space group $P422$, with the crystal unit edges $a = 8.33 \text{ \AA}$ and $c \approx 3a$ [23].

The formula unit of nonstoichiometric magnetite is often described as $Fe_{3-\delta}O_4$, with δ ranging from 0 (magnetite) to $1/3$ (maghemite) [24]. Assuming that the vacancies occur only on the octahedral sites, the formula unit of magnetite can be expressed by



where \square represent the vacancies [22, 24].

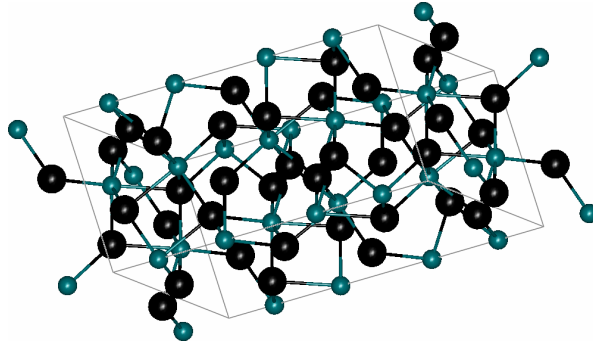


Figure 1.4: Crystal structure of hematite. Black - oxygen ions, green - iron ions.

Hematite has the same crystal structure as corundum and, therefore, it belongs to the space group $R\bar{3}c$ [17]. The unit cell is hexagonal with crystal unit edges of $a = 5.034 \text{ \AA}$ and $c = 13.752 \text{ \AA}$ [16].

The structure can be described as hexagonal closed packed with oxygen ions stacked along the $[001]$ direction and Fe^{3+} -ions filling two thirds of the sites regularly with two filled one vacant. With this the iron ions form a ring like structures as presented in Fig. 1.4.

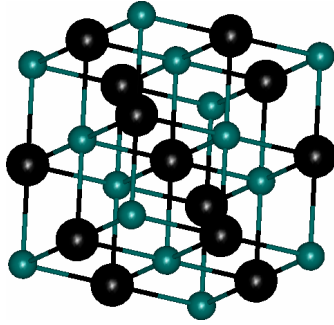


Figure 1.5: Crystal structure of wustite. Black - oxygen ions, green - iron ions.

Wustite has the nominal structure of FeO belonging to the space group $Fm\bar{3}m$ [19], but the stoichiometric phase cannot exist at low pressures [16]. The structure of wustite can be interpreted as two interpenetrating lattices of iron and oxygen as presented in Fig. 1.5. The cubic unit cell contains four formula units FeO and depending on the amount of Fe^{2+} missing in the structure, the crystal unit edge a is changing from 4.28 Å to 4.31 Å [16].

Iron belongs to the space group $Im\bar{3}m$ and has a crystal unit edge of $a = 2.86$ Å [20]. Metallic iron has a closed packed body centered structure at room temperature.

1.3 Field assisted sintering technique

Field Assisted Sintering Technique (FAST), also known as Current-Activated Pressure-Assisted Densification (CAPAD) technique or Spark Plasma Sintering (SPS), is a relatively new powder consolidation technique applying a pulsed direct current and an uniaxial pressure onto a sample which shall be densified.

Fig. 1.6 shows the schematic set-up of a FAST unit. The sample is placed in a vacuum chamber inside a graphite die fixed in a graphite plunger system. The plunger system can apply pressure. It also forces the pulsed direct current from the electrodes through the graphite die and if the sample is conducting also through the sample, itself [8, 9, 25–28].

The advantages of FAST compared to traditional sintering techniques are short process times, the possibility of sintering powders which are difficult to sinter and the elimination of sintering aids. FAST does not only provide the possibility of consolidating a material but also of synthesising the powder during the process. However, the main advantages of FAST lie in the short process times, as well as, the drastically reduction of grain growth, thus, keeping a nanostructure inside the bulk material. This nanostructure alters the properties of the consolidated material [8, 9, 25].

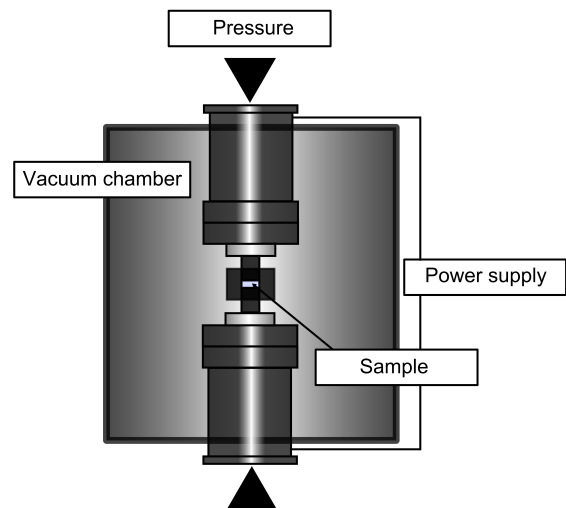


Figure 1.6: Schematic set-up of a FAST unit.

1.3.1 Sintering mechanisms

Sintering refers to the consolidation of powders below the melting point by thermal activation of mass transport processes driven by the reduction of surface and grain boundary energies [8, 25, 27].

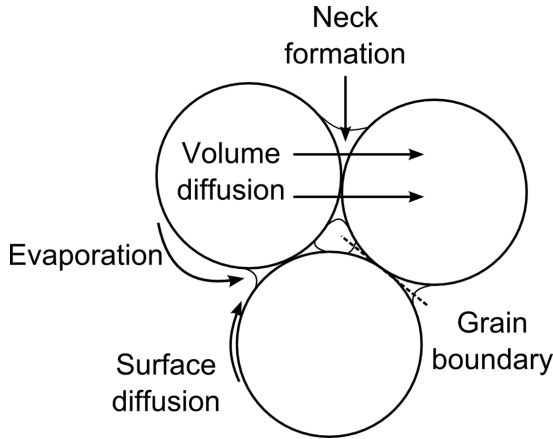


Figure 1.7: Illustration of the sintering mechanisms in a three particle array.

the precursor powders.

The enhancements of densification under the influence of an electric field or a current are attributed to different phenomena - Joule heating, alteration of the grain boundary characteristics, electromigration, electrostatic interaction with grain boundary charges and cleaning of surface impurities [8, 25, 29]. Also, the last effect is related to the generation of plasma during the sintering process, the absence of plasma is rather probable [30]. Other effects of the electric field and of the applied current on the sample like the influence on the solid-state reaction and the diffusion between oxides [31], the mobility of the grain boundaries [32] or the retardation of grain growth [33] have been shown.

Fig. 1.7 illustrates the underlying transport mechanisms which lead to the consolidation of the material. All the shown transport mechanisms, namely evaporation, surface diffusion and volume diffusion lead to the formation of necks between the particles. But actually not all mechanisms lead to a densification of the material. Evaporation and surface diffusion do not bring the particle centers closer together and, therefore, do not cause an actual densification [8]. These processes rather result in the coarsening of the particles. Therefore, a sintering process leads to densification and to coarsening of

Chapter 2

Experimental methods and set-ups

2.1 Scanning electron microscopy

Scanning electron microscopy (SEM) is a technique to image surfaces of samples mostly with secondary electrons. The basic principles of the scanning electron microscope are presented in Fig. 2.1. Electrons originated by a thermionic or a field emission cathode are accelerated by a voltage in the region from 1 kV to 50 kV. The smallest beam cross section at the gun is demagnified by a two- or three-stage electron lens system [34, 35]. Here the electron probe with a diameter of around 1 nm to 10 nm carrying a current of 10^{-12} A to 10^{-10} A is formed at the sample surface [36] and is moved over the sample surface. For different operation modes higher current is needed and due to this reason an increase in the electron-probe diameter from $0.1 \mu\text{m}$ to $1 \mu\text{m}$ is necessary.

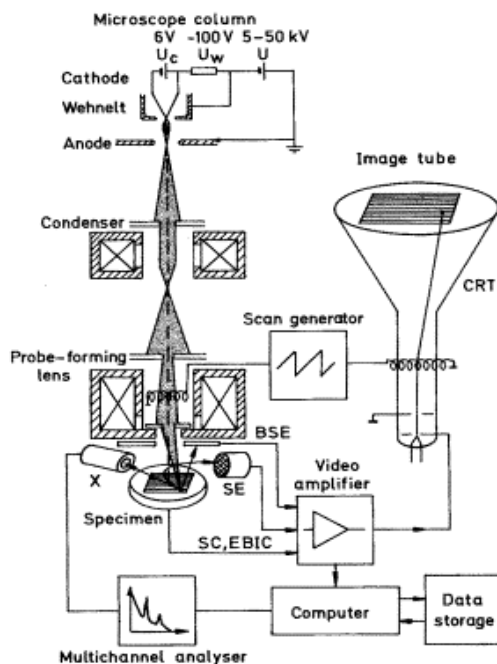


Figure 2.1: Principle of the scanning electron microscope (BSE - backscattered electrons, SE - secondary electrons, SC - specimen current, EBIC - electron beam induced current, X - X-rays, CRT - cathode-ray tube) [36].

The final probe-forming lens has to operate at relatively long working distances, because various particles and quanta emitted from the sample can be collected at the site of the sample. Due to this, the spherical aberration increases and it defines the smallest electron-probe size [36]. A deflection coil system in front of the last lens scans the electron current which leaves the sample. This signal is collected, amplified and modulates the brightness of a cathode-ray tube [34]. When the electron beam is moved over the sample, the collected signal varies. The movement of the electron beam is in correspondence with the spot of the cathode ray tube moving over a screen [34]. If any properties of the sample cause a change of the electron beam which is moved from point to point, a picture is built up on the cathode-ray tube.

Other beam-deflection modes involve rocking of the electron beam when the probe is at a rest. The angle of incidence is rastered to form electron channeling patterns for crystal analysis. Periodic changes of the angle are necessary for recording

stereo images and periodic blanking of the electron beam for stroboscopic modes and time resolved signals [36].

Elastic and inelastic scattering of the electrons from the probe at the sample are the elementary interaction processes. The final detected signal nevertheless is not a result of a single scattering process but mainly a result of several interaction processes and with this a gradual loss of electron energy is observed. The most important interaction products are secondary electrons (SE), backscattered electrons (BSE), Auger electrons (AE) and X-rays [36]. SE are the most important due to the fact that they are easy to collect with a positively biased collector grid placed on one side of the sample due to their low exit energy of a few electron volts depending on the material and the topography of the sample [36, 37].

In the presented study, the mean grain size of the samples was calculated from the scanned pictures from the scanning electron microscope Carl Zeiss DSM 960A. Before the samples were introduced into the vacuum chamber of the microscope, they were sputtered with an additional layer of graphite to ensure conductivity.

2.2 X-ray diffraction

2.2.1 Theoretical background

In condensed matter, atoms are located at distances of typically several ångströms. To resolve details of such structures in scattering experiments, the wavelength λ of the scattering probe has to be in the same order of magnitude. Therefore, X-rays are a suitable probe for resolving such structures. Classically, X-rays are generated in X-ray tubes, but the effectiveness of these tubes is smaller than 1% [38]. Stronger sources of X-rays are synchrotrons. The X-rays are part of the spectrum emitted by charged particles which are accelerated on circular orbits. Due to the high energy E_{el} and, therefore, the high velocity ($v/c \approx 1$) of the particles, the radiated power P is proportional to

$$P \simeq \frac{2e^2c}{R^2} \left(\frac{v}{c}\right)^4 \left(\frac{E_{el}}{mc^2}\right)^4 \sim \frac{\gamma^4}{R^2}, \quad (2.1)$$

where R is the radius of the storage ring and m the mass of the resting particle [38]. The power of the emitted radiation is proportional to the fourth power of the reduced energy ($\gamma = E_{el}/mc^2$). Furthermore, the angular distribution of the emitted radiation is no longer described by a dipolar distribution. The relativistic transformation causes a distortion of the radiation into cone shapes in the direction of motion of the particles. The coherent scattering of radiation on a periodic structure is called diffraction. The general overview of a scattering experiment is shown in Fig. 2.4. The scattering intensity is described by the double differential cross section $d^2\sigma/(d\Omega d\omega_f)$. It is given by the removal rate of particles out of the incident beam due to scattering into the solid angle $d\Omega$ with a frequency range of $d\omega_f$ ($dE_f = \hbar d\omega_f$). In the presented X-ray diffraction studies, the transferred energy is smaller than the photon energy ($E \ll E_i$) and the momentum transfer $\hbar Q$ is connected to the scattering angle θ by

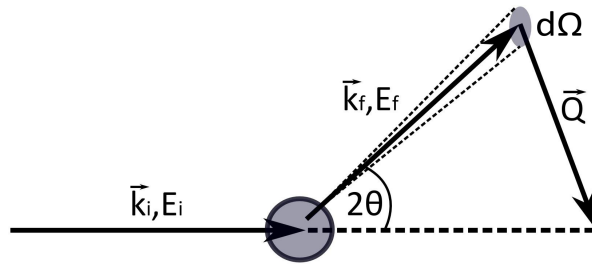


Figure 2.2: Scattering geometry. The incident beam with the wave vector \vec{k}_i and the energy E_i is scattered into the solid angle element $d\Omega$ under the scattering angle 2θ . The scattered beam is characterised by the wave vector \vec{k}_f and the energy E_f . \vec{Q} is the scattering vector.

$$\hbar Q = 2\hbar k_i \sin \theta. \quad (2.2)$$

The double differential cross section can be presented as

$$\frac{d^2\sigma}{d\Omega d\omega_f} = \left(\frac{d\sigma}{d\Omega} \right)_0 S(\vec{Q}, \omega) \quad (2.3)$$

according to [39]. Here, the double differential cross section is separated into two parts. The coupling of the beam to the scattering system is the intrinsic cross section $(d\sigma/d\Omega)_0$ and the properties of the sample without the perturbation of the scattering probe is presented as the scattering function $S(\vec{Q}, \omega)$.

In the case of elastic X-ray scattering, Eq. (2.3) can be simplified into the single differential cross section $d\sigma/d\Omega$:

$$\frac{d\sigma}{d\Omega} = \left(\frac{d\sigma}{d\Omega} \right)_0 S(\vec{Q}). \quad (2.4)$$

During the scattering process a plane wave with the wave vector \vec{k}_i is elastically scattered at the position 0 which leads to the superposition of the original plane wave by a spherical wave with \vec{k}_f and to the scattering amplitude $f(\Omega)$ at large distances. Therefore, the scattering intensity can be described by [38]

$$\left(\frac{d\sigma}{d\Omega} \right)_0 = |f(\Omega)|^2. \quad (2.5)$$

With this the total cross section, taking into account the scattering from all particles, is

$$\sigma = \int \left(\frac{d\sigma}{d\Omega} \right)_0 d\Omega \int_0^{2\pi} d\phi \int_0^\pi \sin \theta d\theta |f(\phi, \theta)|^2. \quad (2.6)$$

Assuming that the incoming electromagnetic radiation has a high energy, the electrons

in the sample are vibrating out of phase without further frequency dependence, with this the frequency independent Thomson cross section can be described by

$$\left(\frac{d\sigma}{d\Omega}\right)_{Th} = \frac{1}{2}r_e^2(1 + \cos\theta), \quad (2.7)$$

where r_e is the classical electron radius [40].

The scattering of the sample can be described by the atomic structure factor. It basically describes the the scattering of the X-rays at the electrons in the sample and, therefore, from every atom f_n . If the atoms arrange in a crystal lattice, the incoming electromagnetic waves are reflected at the parallel lattice planes by the periodically arranged atoms

$$2d \sin\theta = n\lambda, \quad (2.8)$$

with d being the lattice spacing and n an integer [41]. The scattering amplitudes of each atom have to be added with the correct phase

$$F'(\vec{Q}) = \sum_n^N f_n e^{i\vec{Q}\cdot\vec{r}_n} \quad (2.9)$$

$$= f(\vec{Q}) \left(\frac{\sin[\frac{1}{2}N_1\vec{Q}\cdot\vec{a}]}{\sin[\frac{1}{2}\vec{Q}\cdot\vec{a}]} \right) \left(\frac{\sin[\frac{1}{2}N_2\vec{Q}\cdot\vec{b}]}{\sin[\frac{1}{2}\vec{Q}\cdot\vec{b}]} \right) \left(\frac{\sin[\frac{1}{2}N_3\vec{Q}\cdot\vec{c}]}{\sin[\frac{1}{2}\vec{Q}\cdot\vec{c}]} \right). \quad (2.10)$$

For constructive interference, each factor has to be non-zero, therefore \vec{Q} has to satisfy the Laue conditions

$$\vec{Q}\cdot\vec{a} = 2\pi h, \quad \vec{Q}\cdot\vec{b} = 2\pi k, \quad \vec{Q}\cdot\vec{c} = 2\pi l \quad (2.11)$$

with h , k and l being integers [42]. The solution for \vec{Q} is $\vec{Q} = h\vec{A} + k\vec{B} + l\vec{C}$, with \vec{A} , \vec{B} and \vec{C} being reciprocal lattice vectors. Therefore, X-ray scattering gives an image of the reciprocal lattice.

To identify the scattering from a crystal structure, the lattice positions \vec{r}_n and the basis location \vec{r}^α have to be considered. The complete scattering amplitude from atoms with the atomic form factors $f_\alpha(\vec{Q})$ in the crystal is given by [38]

$$F'(\vec{Q}) = \sum_{n,\alpha} f_\alpha(\vec{Q}) e^{i\vec{Q}\cdot(\vec{r}_n + \vec{r}^\alpha)} \quad (2.12)$$

$$= \sum_n \left(\sum_\alpha f_\alpha(\vec{Q}) e^{i\vec{Q}\cdot\vec{r}^\alpha} \right) e^{i\vec{Q}\cdot\vec{r}_n}. \quad (2.13)$$

Here, the structure amplitude

$$F(\vec{Q}) = \sum_\alpha f_\alpha(\vec{Q}) e^{i\vec{Q}\cdot\vec{r}^\alpha} \quad (2.14)$$

describes the scattering of the unit cell.

The complete amplitude $F'(\vec{Q})$ of the scattered wave is obtained by the phase correct superposition of all partial waves originated from the electrons with the electron density $n_e(\vec{r})$ is

$$F'(\vec{Q}) = \int_{sample} d^3\vec{r} n_e(\vec{r}) e^{i\vec{Q}\cdot\vec{r}}. \quad (2.15)$$

The measured intensity I is

$$I \propto S(\vec{Q}) = |F'(\vec{Q})|^2 = \frac{1}{N} \left| \int_{sample} d^3\vec{r} n_e(\vec{r}) e^{i\vec{Q}\cdot\vec{r}} \right|^2 = \frac{1}{N} \left| \tilde{n}_e(\vec{Q}) \right|^2. \quad (2.16)$$

The scattering function is defined by the Fourier transformed of the electron density function $\tilde{n}_e(\vec{Q})$ [38]. Basically, $n_e(\vec{Q})$ can be determined from the experimentally obtained $S(\vec{Q})$ by back transformation. Two problems appear with this transformation. First, the experiment only yield to finite range of \vec{Q} with a finite resolution and second, only the magnitude and not the phase is determined during the experiment. To determine the structure of a system, it is therefore necessary to start with certain assumptions for the electron density function which is compared to the experimental data. One approach to realise this is the Rietveld refinement procedure [43].

2.2.2 Rietveld refinement combined with Fourier analysis

Rietveld refinement is a structure refinement method directly employing the profile intensities obtained from step-scanning measurements [43]. In polycrystalline samples a loss of information is inevitable due to the random orientation of the crystallites as well as through the overlap of diffraction peaks [43]. By the use of profile intensities instead of integrated quantities in a refinement procedure, a least square method allows the maximum extraction of information of a powder diffractogram [44]. In the Rietveld refinement procedure, the background and the peak profiles for all phases present in the sample are evaluated. The background is usually described by a polynomial function. For each diffraction peak, the profile is defined by the angular position, the intensity and the peak shape [45].

The positions and the intensities are analysed from the crystal structures and phase compositions. The refinements can be easily extended to include microstructural information i.e. crystallite sizes, microstrains and defect concentrations by introducing line-broadening analysis [46]. The stress fields modify the peak positions, the textures of samples affect the integrated intensities of the diffractions and the microstructures change the shapes of the profiles [45].

Therefore, a model was developed which connects the profile widths and the shapes directly to the crystallite sizes (column length) and microstrains along the crystallographic directions, using conditions of cosine Fourier coefficients and their derivatives [46, 47]. Crystallite sizes, shapes as well as microstrains can be determined by the angular dependence of the peak widths replacing the peak shape formula of Caglioti

[47, 48].

The full width half maximum (FWHM) of the diffraction peaks is supposed to follow the equation

$$FWHM = (U \tan^2 \theta + V \tan \theta + W)^{1/2} \quad , \quad (2.17)$$

with U, V, W being half width parameter [48]. The integrated intensities of the peaks are supposed to be a function of the structural parameters. Therefore, the least square fitting procedure tries to minimise [47]

$$R_{wp} = \left[\frac{\sum_i w_i (Y_{io} - Y_{ic})^2}{\sum_i w_i Y_{io}^2} \right]^{1/2} \quad . \quad (2.18)$$

Y_{io}, Y_{ic} are the experimental and calculated X-ray diffraction intensities at the angle $2\theta_i$, respectively, and w_i are the statistical weights. The goodness of the fit can be obtained comparing R_{wp} with R_{exp} [47], where R_{exp} is defined as

$$R_{exp} = \left[\frac{N - P}{\sum_i w_i Y_{io}^2} \right]^{1/2} \quad , \quad (2.19)$$

where N is the number of observations and P the number of parameters.

During the Rietveld refinement, first a pseudo Voigt function ($pV(2\theta)$), which is corrected for asymmetry, is convoluted by an exponential function, according to

$$pV(2\theta) = I \left(\frac{1 - \eta}{1 + S^2} + \eta \exp(-\ln 2S^2) \right) \quad (2.20)$$

$$S = \frac{2\theta - 2\theta_0}{HWHM} \quad (2.21)$$

$$A(2\theta) = \exp[-a_s |2\theta - \theta_0| \tan(2\theta_0)] \quad , \quad (2.22)$$

with η being the gaussianity, θ_0 being the Bragg angle of the used wave length and a_s being the asymmetry parameter [47]. The pseudo-Voigt function is a linear combination of Lorentzian and Gaussian components in the ratio $\nu/(1-\nu)$, where ν is a pseudo-Voigt mixing parameter. Furthermore, the shape functions of $FWHM$ according to Caglioti [48] are taken into account [47, 49].

The profile of a diffractogram can be described by a convolution

$$Y_c(2\theta) = [B \cdot (I \cdot A)](2\theta) + bkg \quad , \quad (2.23)$$

where B is the true line broadening, I the symmetric part of the instrumental function and bkg is a polynomial function determining the background. B and I can both be assumed to be pseudo Voigt functions and their convolution can be calculated analytically [47]. Then the convolution with the asymmetric function $A(2\theta)$ has to be determined numerically.

The mean crystallite size M and the microstrain $\langle \epsilon^2 \rangle^{1/2}$ can be derived by a fitting procedure adopted from Nandi [50] according to the single peak method for Fourier

analysis T

$$\frac{dT_{pV}}{dL}\Big|_{L=0} = -\frac{1}{M} \quad (2.24)$$

$$T_{pV}\Big|_{L=M/2} = [1 - \pi^2\langle\epsilon^2\rangle M^2/(2d^2)]e^{-1/2}. \quad (2.25)$$

Here L is the column length normal to the diffraction plane. By assuming a Gaussian microstrain distribution [47], Eq. (2.25) can be rewritten as

$$T_{pV}\Big|_{L=M/2} = \exp[-\pi^2\langle\epsilon^2\rangle M^2/(2d^2) - 1/2] \quad (2.26)$$

Here d is the interplanar distance. This approach for the evaluation of the size-strain does not need any further assumption about the trend of the microstrain in dependence of the crystallite size, which makes it more suitable for the profile refinement. Additionally it is possible to include anisotropic crystallite sizes [46, 47, 49].

2.2.3 Experimental set-up

High energy X-ray diffraction experiments were performed at the High Energy Material Science (HEMS) beamline P07 located at the high brilliance synchrotron radiation storage ring PETRA III, DESY Germany. The basic design parameters of the storage ring are an energy of 6 GeV and a current of 100 mA. The source of X-rays for HEMS is a 2 m long standard PETRA undulator.

The investigations were performed in the test facility EH1 using an indirectly water-cooled single bounce monochromator with a Si(220) Laue single-crystal leading to monochromatic synchrotron radiation with a wavelength $\lambda = 0.1424 \text{ \AA}$ [51, 52]. The experiments were carried out in Debye-Scherrer geometry with a sample to detector distance of 1200 mm. The diffraction patterns were collected with a Perkin Elmer image plate detector. The experimental set-up used at the beamline is presented in Fig. 2.3.

The diffraction patterns were integrated in 5° steps and each of the obtained spectra was processed applying Rietveld refinement procedure [43] as implemented in the MAUD code [53, 54] following the guideline for structure refinement [55] concerning data collection, background contributions, peak shape functions, refinement of profile and structure parameters as well as Fourier analysis and the interpretation of the refinement values.

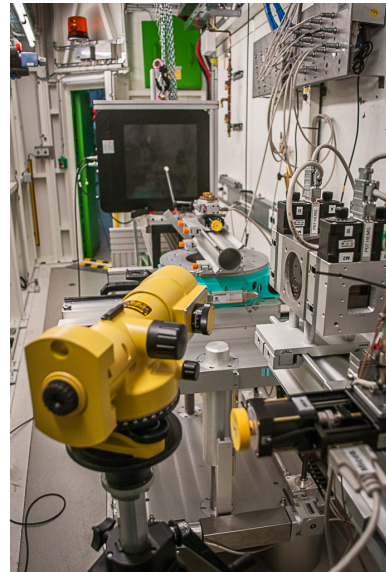


Figure 2.3: Layout of the experiment at the P07 Experimental Hutch 1. In the foreground the slit system, in the middle the sample holder and in the background the Perkin Elmer detector with the beamstop in the center is place.

2.3 Mößbauer spectroscopy

2.3.1 Mößbauer effect

Nuclear resonant absorption of γ -quants describes the absorption and emission of a photon by a nucleus. An important issue concerning this effect is the recoil of the nucleus after emission and absorption of the γ -quant.

First a free nucleus is considered. The energetically lowest state of the nucleus (ground state, E_g) can be excited by electromagnetic radiation or as well as by the decay of a radioactive mother isotope into an excited state (E_e). The excited state will afterwards decay by emitting electromagnetic radiation into the ground state after a characteristic time depending on the half life τ_0 . The difference in energy is therefore $E_0 = E_e - E_g$. The lifetime of the excited states and the energetic width Γ_0 (full width at half maximum) of the Lorentzian shaped energy distribution $N(E)$ are correlated by Heisenberg's uncertainty principle

$$\Gamma_0 = \frac{\hbar}{\tau_0} \quad . \quad (2.27)$$

Due to momentum conservation, the emitting nucleus with the mass m has to balance the momentum from the emitted photon $p = E_\gamma/c$. The nucleus recoils with a recoil energy $E_R = p^2/(2m) = E_\gamma^2/(2mc^2)$. Therefore, the energy distribution of the emitted photons is centered around a reduced value $E_\gamma = E_0 - E_R$:

$$N(E) = N_0 \frac{\left(\frac{\Gamma_0}{2}\right)^2}{(E - (E_0 - E_R))^2 + \left(\frac{\Gamma_0}{2}\right)^2} \quad . \quad (2.28)$$

The same appears for the absorption of the photon by a nucleus. Photons need the energy $E_\gamma = E_0 + E_R$ to be absorbed by the nucleus with a energy dependent absorption cross section $\sigma(E)$, with

$$\sigma(E) = \sigma_0 \frac{\left(\frac{\Gamma_0}{2}\right)^2}{(E - (E_0 + E_R))^2 + \left(\frac{\Gamma_0}{2}\right)^2} \quad . \quad (2.29)$$

Resonance is only possible when both distributions Eq. (2.28) and Eq. (2.29) at least partially overlap with the resonance condition

$$\frac{\Gamma_0}{2E_R} > 1 \quad . \quad (2.30)$$

In the case of ^{57}Fe at rest, the photon energy is $E_\gamma = 14.4$ keV, which leads to a recoil energy $E_R = 1.95 \cdot 10^{-3}$ eV. The half life of the excited state in ^{57}Fe is $\tau_0 = 98.1$ ns, which leads to a natural half width $\Gamma_0 = 4.65 \cdot 10^{-9}$ eV [56–58]. With this the resonance condition is not fulfilled and there is no overlap between the absorption and emission spectra.

When the nucleus is not at rest but in motion, due to thermal fluctuations like in a

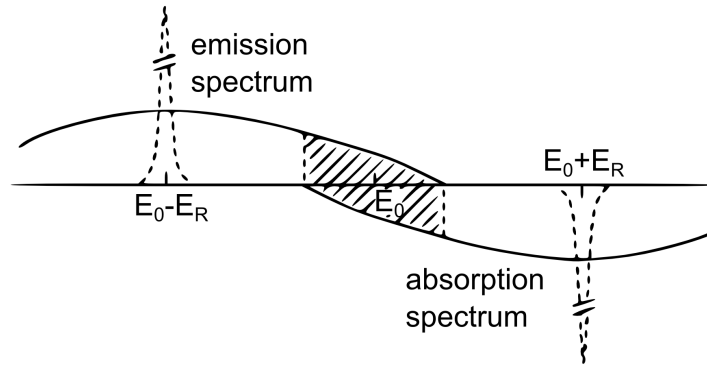


Figure 2.4: Schematics of an emission and absorption spectra of a free nucleus [56].

liquid or in a gas, the Doppler shift leads to a broadening of Eq. (2.28) and Eq. (2.29). The thermal velocities correspond to a kinetic energy in the region of E_R and they are distributed over a wide range according to the Maxwell distribution. With this, a partial overlap of Eq. (2.28) and Eq. (2.29) can be observed, but still the overlap is small [56–58].

The situation changes, when the nucleus is not free but bound in a solid. When the nucleus absorbs a photon it cannot recoil freely because the recoil energy is typically smaller than the binding energy (\sim eV). Additionally, the recoil does not only concern a single nucleus, but the whole mass of the lattice has to be taken into account. This reduces the recoil energy drastically ($\sim 10^{-20}$ eV). This effect was first described by Rudolf Mößbauer, who investigated the resonant absorption of an ^{191}Ir solid [59]. The nucleus in a solid is not bound rigidly. It is free to vibrate and phonons can exchange energy with the lattice. This results in the creation and annihilation of phonons. The probability of transitions without phonon interactions is called Lamb-Mößbauer factor f_{LM} [60].

Assuming the Einstein model, only one vibrational frequency ω is present in the lattice [61]. The lattice can receive or release energy as multiples of $\hbar\omega$ ($0, \pm\hbar\omega, \pm 2\hbar\omega, \dots$). If $E_R < \hbar\omega$, the lattice cannot absorb the recoil energy meaning a zero-phonon process and the γ -quant is emitted without recoil. The probability of this event is described by the Lamb-Mößbauer factor with

$$f_{LM} = e^{-k^2\langle x^2 \rangle} \quad . \quad (2.31)$$

$\langle x^2 \rangle$ is the square displacement of the nucleus along the wavevector \vec{k} of the emitted γ -ray. To have a significant value for f_{LM} , $-k^2\langle x^2 \rangle$ needs to be much smaller than one. This can be achieved, when the nucleus is bound in a crystalline or an amorphous solid. Furthermore, the wavevector \vec{k} should not be too large, which limits the energy $E_\gamma = \hbar ck$ for the γ -quant for a typical Mößbauer experiment to around 150 keV [57].

2.3.2 Hyperfine interactions

The nuclear resonant absorption process was described as an excited state E_e decaying into a ground state E_g with an energy difference E_0 . The only influence on the energy taken into account was the Doppler shift from thermal motion and lattice vibrations. Furthermore, there can be other interactions which influence the transition and also lead to a splitting of degenerated nuclear levels. The nucleus is charged and composed out of particles with spins. The presence of the atomic electron cloud and internal as well as external magnetic fields are influencing the nuclear levels. These influences are small and can be interpreted as perturbations. The possible perturbations which can be observed are summarised as hyperfine interactions [56–58, 62]. In the case of Mößbauer spectroscopy three hyperfine interactions, also schematically presented in Fig. 2.5, are mainly observed:

- *Electric monopole interaction*, causing an *isomer shift* IS of the whole resonance spectrum,
- *Electric quadrupole interaction*, causing a *quadrupole splitting* QS of the resonance spectrum and
- *Magnetic dipole interaction*, causing a Zeeman splitting of the resonance spectrum with the *magnetic hyperfine field* $\mu_0 H_{hf}$,

which shall be briefly introduced.

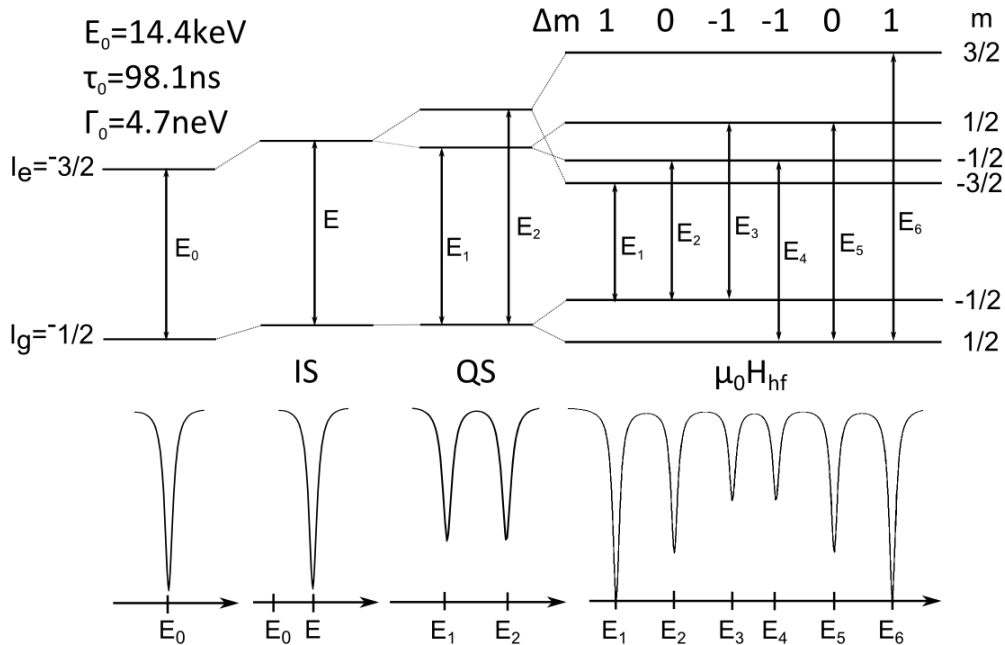


Figure 2.5: Schematics of the nuclear levels and the influences of the isomer shift IS, the quadrupole splitting QS and the magnetic hyperfine field $\mu_0 H_{hf}$ on the nuclear levels for ^{57}Fe .

The Hamiltonian of a perturbed nucleus is shown in Eq. (2.32) [56–58, 62].

$$\hat{H} = \hat{H}_0 + \hat{H}_{hf} \quad (2.32)$$

$$= \hat{H}_0 + \hat{H}_{el} + \hat{H}_{mag} \quad (2.33)$$

It is assumed, that the influences of the electric and the magnetic field can be treated separately. The interaction between the charged nucleus and the surrounding electric fields can be expressed as

$$E_{el} = \int_n \rho_n(\vec{r}) V(\vec{r}) d^3r \quad . \quad (2.34)$$

Here, $\rho_n(\vec{r})$ is the charge density, the protons, and $V(\vec{r})$ the scalar potential of all surrounding charges, the electrons. As the potential does not vary drastically inside the small volume of the nucleus, the potential can be developed into a Taylor series at $r = 0$:

$$V(\vec{r}) = V_0 + \sum_{i=1}^3 \frac{\partial V}{\partial x_i} \Big|_{r=0} \cdot x_i + \frac{1}{2} \sum_{i,j=1}^3 \frac{\partial^2 V}{\partial x_i \partial x_j} \Big|_{r=0} \cdot x_i x_j + \dots \quad (2.35)$$

$$\begin{aligned} E_{el} = V_0 \underbrace{\int_n \rho_n(\vec{r}) d^3r}_{eZ} + \sum_{i=1}^3 \frac{\partial V}{\partial x_i} \Big|_{r=0} \cdot \underbrace{\int_n \rho_n(\vec{r}) x_i d^3r}_{=0} \\ + \frac{1}{2} \sum_{i,j=1}^3 \frac{\partial^2 V}{\partial x_i \partial x_j} \Big|_{r=0} \cdot \int_n \rho_n(\vec{r}) x_i x_j d^3r + \dots \end{aligned} \quad (2.36)$$

The first term $V_0 eZ$ represents the interaction between a point-like nucleus and the surrounding charges. It is independent of the nucleus being in the excited or the ground state. Therefore, it is not of further interest. The second term is zero due to the reason that $\rho_n(\vec{r})$ is an even function with respect to \vec{r} . The third term can be rearranged, adding and subtracting $\frac{1}{3} \delta_{ij} \rho_n(\vec{r}) r^2$ leading to

$$E_{el} = \underbrace{\frac{1}{6} \sum_{i=1}^3 V_{ii} \int_n \rho_n(\vec{r}) r^2 d^3r}_{E_{IS}} + \underbrace{\frac{1}{6} \sum_{i,j=1}^3 V_{ij} \int_n \rho_n(\vec{r}) (3x_i x_j - \delta_{ij} r^2) d^3r}_{E_{QS}} \quad (2.37)$$

The first part of Eq. (2.37) represents the *isomer shift* [56–58, 62]. It is assumed, that the scalar potential V obeys the Poisson equation. Therefore, at the nucleus $r = 0$, the following equation can be adopted

$$V(r = 0) = \sum_{i=1}^3 V_{ii} \Big|_{r=0} = -4\pi \rho_e(0) = 4\pi e |\Psi(0)|^2 \quad . \quad (2.38)$$

$-e|\Psi(0)|^2$ is the charge density of the electrons and $\Psi(0)$ is the probability of finding a charge at the center of the nucleus. For the nucleus, furthermore, a spherical charge

density is assumed, $\rho_n(\vec{r}) = Ze\frac{3}{4\pi R^3}$. This leads to

$$E_{IS} = \frac{2\pi}{5}e|\Psi(0)|^2R^2 \quad . \quad (2.39)$$

It is worth to mention, that the nuclear radii of the ground state and the excited state are not equal. Thus an energy shift can be derived, assuming, that the radii are almost equal, it is approximated that $R_e - R_g = \delta R$ and $R_e + R_g = 2R$

$$\Delta E_{IS} = \frac{4\pi}{5}e|\Psi(0)|^2\frac{\delta R}{R}R^2 \quad . \quad (2.40)$$

In the experiment, the nuclear radii are mainly the same for the source S and the absorber A, but the electron density at the nucleus is different. s-electrons have a probability to penetrate the nucleus and to spend a certain fraction of time there as they do not have an angular momentum. Additionally, p_{1/2}-electrons can penetrate the nucleus, if relativistic effects are taken into account [62]. The electron density at the nucleus changes, depending on the valence state and the chemical bonding. These changes can be directly attributed to changes in the population of the s-electron density or indirectly by p-, d- and f- electrons by shielding the s-electrons [57, 62]. Thus, the *isomer shift* is defined between the absorber and the source by:

$$IS = \Delta E_{ISA} - \Delta E_{IS}^S = \frac{4\pi}{5}eS(Z)[|\Psi^A(0)|^2 - |\Psi^S(0)|^2]\frac{\delta R}{R}R^2 \quad . \quad (2.41)$$

Here, $S(Z)$ is a relativistic dimensionless correction factor, which is 1.29 and $\frac{\delta R}{R}$ is approximately $-0.9 \cdot 10^{-3}$ for ⁵⁷Fe [57, 62].

The second part of Eq. (2.37) is the *quadrupole splitting* [56–58, 62]. For further explanation, the classical description is replaced for the quantum mechanical by replacing $\rho(\vec{r})$ for the density operator $\hat{\rho}(\vec{r}) = \sum_p e\delta(\vec{r} - \vec{r}_p)$, where \sum_p represents the sum over all nucleons p :

$$\hat{H}_{QS} = \frac{1}{6}e \sum_{i,j=1}^3 V_{ij} \sum_p (3x_{p_i}x_{p_j} - \delta_{ij}r_p^2) \quad . \quad (2.42)$$

It is necessary to determine the eigenstates I of the ground state (I_g) as well as the eigenstates of the excited state (I_e) by calculating the matrix elements of $\langle I, m | \hat{H}_{QS} | I, m \rangle$. The sum presents the nuclear quadrupole moment. Applying the Wigner-Eckart theorem [57], the tensor can be replaced by a tensor operator for the angular momentum, Eq. (2.42) leads to

$$\langle I, m | \sum_p (3x_{p_i}x_{p_j} - \delta_{ij}r_p^2) | I, m' \rangle = C \cdot \langle I, m | 3\frac{I_i I_j + I_j I_i}{2} - \delta_{ij}I^2 | I, m' \rangle \quad . \quad (2.43)$$

Considering a nuclear state with the spin I and a degeneration of $(2I + 1)$, the multiplet of $(2I + 1)$ partial states of the degenerated nuclear state I all have a symmetrical tensor with the rank two and trace zero, which are proportional to the tensor of the

angular momentum [56–58, 62]. The constant of proportionality C can be determined, considering the case $m = m' = I$ and $i = j = z$.

$$\underbrace{\langle I, I | \sum_p (3z_p^2 - r_p^2) | I, I \rangle}_Q = C \cdot \underbrace{\langle I, I | 3I_z^2 - I^2 | I, I \rangle}_{I(2I-1)} \quad (2.44)$$

The left side shows the angular momentum of the nuclear charge distribution. To define a value Q only an axial symmetry is of importance [56–58, 62]. Here, the quadrupole moment is positive for a cigar shaped nucleus and negative for an oblate shaped nucleus. The Hamiltonian of the electric quadrupole interaction follows

$$\hat{H}_{QS} = \frac{eQ}{6I(2I-1)} \sum_{i,j} \left[\frac{3}{2} (I_i I_j + I_j I_i) - \delta_{ij} I^2 \right] \quad (2.45)$$

\hat{H}_{QS} vanishes, when the nuclear charge density $\rho_n(\vec{r})$ is spherical or when $Q = 0$. Q is zero, if $I = 0$ and $I = \frac{1}{2}$. Furthermore, if the crystal is cubic, \hat{H}_{QS} vanishes.

Additionally, the contributions from s - and $p_{1/2}$ -electrons can be neglected, due to the fact that they lead to potentials with spherical symmetry. Excluding these electrons, the charge density at $r = 0$ equals zero. To simplify Eq. (2.45), the Laplace equation with $\sum_i V_{ii} = 0$ has to be taken into account and a coordinate system is defined in which V_{ij} diagonalises with the axis: $V_{zz} \geq V_{xx} \geq V_{yy}$:

$$\hat{H}_{QS} = \frac{eQV_{zz}}{4I(2I-1)} \left[3\hat{I}_z^2 - I^2 + \frac{\eta}{2} (\hat{I}_+^2 + \hat{I}_-^2) \right] \quad (2.46)$$

V_{zz} is the electric field gradient ($\vec{\nabla} \vec{E} = -\vec{\nabla} \vec{\nabla} V$) and $\eta = \frac{V_{xx} - V_{yy}}{V_{zz}}$ the asymmetry parameter. With the Hamiltonian, it is possible to determine the eigenstates of the system, leading to

$$E_{QS} = \frac{eQV_{zz}}{4I(2I-1)} [3m_I^2 - I(I+1)] \sqrt{1 + \frac{\eta^2}{3}} \quad (2.47)$$

This equation is correct for all cases with $\eta = 0$, for $I = \frac{3}{2}$ also with $\eta \neq 0$ and for $I = 2$ with $m = 0$ and $m = +2$. For all other cases, only numerical results exist.

In the case of ^{57}Fe , the ground state does not have a quadrupole moment. If the electric field gradient V_{zz} at the nucleus does not vanish, the excited state splits into two two-fold degenerated sublevels:

$$E(\pm \frac{1}{2}) = -\frac{eQV_{zz}}{4} \sqrt{1 + \frac{\eta^2}{3}} \quad (2.48)$$

$$E(\pm \frac{3}{2}) = +\frac{eQV_{zz}}{4} \sqrt{1 + \frac{\eta^2}{3}} \quad (2.49)$$

The quadrupole moment of ^{57}Fe is $Q = 0.15(2)$ barn [63]. With this, there are two possible transitions from the excited to the ground state as presented in Fig. 2.5. The

electric field gradient V_{zz} itself depends on two factors. The first contribution is originated by surrounding ions which are not coordinated in a cubic lattice and is called the lattice contribution V_{zz}^{lat} . The second origin is the Mößbauer atom itself, when the valence electrons are distributed anisotropically. This is called valence contribution V_{zz}^{val} . V_{zz}^{lat} is normally enhanced by the polarisation of the electron shells from distant ions, while V_{zz}^{val} is diminished by shielding from core electrons, leading to

$$V_{zz} = (1 - \gamma_\infty)V_{zz}^{lat} + (1 - R)V_{zz}^{val} \quad . \quad (2.50)$$

Here, γ_∞ is the Sternheimer anti-shielding factor and R the Sternheimer shielding factor. For ^{57}Fe $\gamma_\infty \sim -9$ and $R = [0.25\dots 0.35]$ [57, 62].

A nucleus in a state with a spin quantum number bigger than zero will interact with a magnetic field via its magnetic dipole moment $\vec{\mu}$. This magnetic dipole interaction or the so called *nuclear Zeeman effect* [64] can be described by the Hamiltonian

$$\hat{H}_{mag} = -\mu_0 \hat{\vec{\mu}} \cdot \hat{\vec{H}} = -g_n \mu_n \mu_0 \hat{I} \cdot \hat{H} \quad . \quad (2.51)$$

Here, \vec{H} is the magnetic field, G_n the nuclear Landé factor, $\mu_n = e\hbar/2m_p c$ the nuclear magneton (m_p proton mass) and μ_0 the vacuum permeability. The eigenstates E_{mag} of can be determined diagonalising the Hamiltonian matrix [56–58, 62], leading to

$$E_{mag} = -\frac{\mu\mu_0 H m}{I} = -g_n \mu_n \mu_0 H m \quad . \quad (2.52)$$

This shows that the nuclear Zeeman effect splits the nuclear states with the spin quantum number I into $2I + 1$ equally spaced nondegenerated sublevels $|I, m\rangle$, where m is the magnetic quantum number representing the z -axis of I . Normally, the z -axis is chosen to be parallel to the magnetic field $H_z = H_{hf}$. The transition from the excited to the ground state can take place, when $\Delta I = 1$ and $\Delta m = 0, \pm 1$. For ^{57}Fe , six possible transitions are observed from $I = \frac{3}{2}$ with four sublevels to $I = \frac{1}{2}$ with two sublevels, which are presented in Fig. 2.5. The relative line intensities taken from left to right are 3:2:1:1:2:3 for an isotropic distribution of the magnetic field with respect to the γ -quant propagation. The intensities can be determined by the square of the Clebsch-Gordan coefficients [62].

The determination of the magnetic hyperfine splitting allows the determination of the effective magnetic field at the nucleus or the *magnetic hyperfine field* H_{hf} , which is normally a superposition of an applied field H_{ext} and an internal field H_{int} , which arises from the magnetic moment of the valence electrons [56, 62].

$$H_{hf} = H_{ext} + H_{int} \quad (2.53)$$

$$= H_{ext} + H_{fermi} + H_{orb} + H_{dip} + H_{thf} \quad (2.54)$$

The internal magnetic field is mainly originated by the isotropic Fermi contact field H_{fermi} , which is caused by the net spin-up or spin-down s -electron density at the nucleus as a consequence of spin-polarisation of s -electrons by unpaired valence electrons [65].

Even for closed s -shells the net spin density differs from zero, because the spin of the s -electrons interacts with the outer p -, d - and f -electron shells. s -electrons which have a spin antiparallel to the outer shells experience a stronger repulsion than s -electrons with a parallel spin. Therefore, they stay closer to the nucleus and dominate over the other s -electrons.

Furthermore, the orbital motion of valence electrons H_{orb} contribute to the internal magnetic field at the nucleus. Not completely filled shells possess an angular momentum which interacts with the nuclear magnetic moment. The spin-dipolar field H_{dip} describes the interaction of the nuclear angular moment with spins of valence electrons. Half filled shells, as well as atoms in a local cubic symmetry, have H_{dip} equal to zero. The transferred hyperfine field H_{thf} is originated by distant magnetic ions which can polarise core electrons, in case of non-metallic system, or the conduction electrons, in case of metallic systems [56–58, 62].

2.3.3 Line shape

The line shape of the Mößbauer lines expresses the energetic distribution of the γ -quants in the Mößbauer spectrum. Since the distribution of the γ -quants and with this the energetic environment of the Mößbauer nuclei is important for the interpretation of each Mößbauer spectrum, the basic line shape of the spectrum is introduced.

From the source emitted photons can be described by the intensity [57]:

$$I_e = W_e \frac{\Gamma}{2\pi} \cdot \int_0^\infty d(\xi) e^{-(n_e a_e \sigma_e + \mu_e) \cdot \xi} d\xi, \quad (2.55)$$

where $d(\xi)$ is the density of emitting nuclei in dependence of the depths ξ , μ_e the coefficient for electronic absorption in the source, n_e number of nuclei per volume unit, a_e the amount of resonant nuclei, σ_e absorption cross section of the source, W_e the emission probability and $\Gamma/2\pi$ the normalisation factor with:

$$f_s = \frac{\Gamma}{2\pi} \int_0^\infty W_e(\omega_{\lambda'}) d\omega_{\lambda'}(\vec{k}') \quad (2.56)$$

being the energy integral of the spectrum normalised to the Lamb-Mößbauer factor. Here it is worth to mention that the emission probability also depends on the velocity of the source.

The emitted photons from the source in direction of the sample are partially absorbed. This absorption can be resonant and non-resonant. The general form of the Mößbauer line shape in transmission geometry can be described by:

$$I(v) = e^{-\mu_a t_a} \left\{ (1 - f_s) \int_0^\infty d(\xi) e^{-\mu_e x_i} d\xi + \frac{\Gamma \hbar}{2\pi} \int_{-\infty}^\infty d\omega_{\lambda'}(\vec{k}') e^{-n_a \sigma_a t_a a_a} W_a \int_0^\infty d(\xi) e^{-(n_e a_e \sigma_e + \mu_e) \cdot \xi} d\xi \right\}, \quad (2.57)$$

with n_a being the number of nuclei in the absorber per volume unit, a_a the amount

of resonant nuclei in the absorber, W_a the emission probability of the absorber σ_a absorption cross section of the absorber, μ_a the coefficient for electronic absorption in the absorber and t_a the absorber thickness [57]. The normalisation conditions are:

$$f_s = \frac{\Gamma}{2\pi} \int_0^\infty W_e(v) dv \quad (2.58)$$

$$\sigma_a \left\{ \omega_{\lambda'}(\vec{k}') = \frac{E_0}{\hbar} \right\} = \sigma_0 f_a, \quad (2.59)$$

where f_a is the Lamb-Mössbauer factor of the absorber.

The first term in Eq. (2.57) describes the reduction of the intensity due to nonresonant photons absorbed in the sample. The second term in Eq. (2.57) describes the resonant photons which can be absorbed resonantly and nonresonantly in the sample. It is to be seen that the line shape depends on numerous properties of the source and the absorber itself. First of all, it depends on the velocity of the source, the energy difference of the transitions in the nuclei in the source and the absorber, the thickness of the source and the absorber, the Mössbauer nuclei density, as well as microscopic properties of the source and the absorber, described by the emission and absorption probabilities.

The emission and absorption probability of a system, can be described in general by the transition probability W , assuming $f_s = 1$ [57]:

$$W = \frac{2}{\Gamma \hbar} \text{Re} \int_0^\infty \exp \left\{ i\omega t - \frac{\Gamma}{2\hbar} t \right\} \langle \hat{H}_{nucleus}(0) \hat{H}_{nucleus}^+(t) \rangle dt. \quad (2.60)$$

The correlation function $\langle \hat{H}_{nucleus}(0) \hat{H}_{nucleus}^+(t) \rangle$ shows an explicit time dependence which in many cases cannot be neglected.

When the nucleus is fixed in a lattice and the electronic environment does not show a time dependence $\hat{H}_{nucleus}$, the correlation function can be determined as a sum of Lorentzian lines with the width Γ .

2.3.4 Experimental set-up

The ^{57}Fe Mössbauer spectroscopy experiments were performed in transmission geometry at room temperature.

The γ -ray source was 25 mCi ^{57}Co in a Rh - matrix. ^{57}Co has a half-life of 270 d and decays under electron capturing in the excited state $I = \frac{5}{2}$ of ^{57}Fe . This state has a short half-life of 8.8 ns and can further decay directly into the ground state of the isotope or decay to the excited state $I = \frac{3}{2}$, what occurs in 91% of all cases. The excited state $I = \frac{3}{2}$ has a longer half-life of 98.1 ns leading to a narrow line

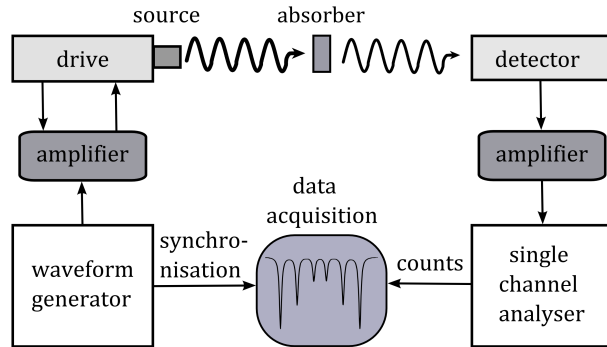


Figure 2.6: Schematics of experimental set-up of the Mössbauer spectroscopy in transmission geometry.

width [56–58], which can excite the Mößbauer nucleus in the absorber as illustrated in Fig. 2.6. The source is mounted in a FAST Comtec Mößbauer drive unit working in constant acceleration mode. The Doppler shift changes the frequency and with this the energy of the emitted γ -quants according to

$$\Delta E = E - E_0 = E_0 \frac{v}{c} \cos \theta \quad , \quad (2.61)$$

where θ is the angle between the relative velocity of the drive and the direction of emitted γ -quant. It ensures that the resonance frequencies in the absorber which are shifted due to hyperfine interactions can be excited. To accumulate the Mößbauer spectrum, the electric pulses delivered to the detector transmitted through the sample must be recorded synchronously to the sweep of the velocity of the source. This is achieved with a multichannel analyser, in which a function generator triggers a digital counter, the channel, one by one. Mößbauer transmission spectra were all collected in a velocity range ± 11 mm/s with 1024 channels before folding. For the need of calibration, a standard α -Fe foil was used.

Details about the fitting procedure and the applied fitting model of the Mößbauer spectra, are introduced in the following chapter.

Chapter 3

Interpretation of Mößbauer spectra - from bulk materials to nanoparticles

To interpret Mößbauer spectra different models can be used. For a further discussion of the nanostructured bulk materials, an introduction to the most common models will be given. Also two examples, which show the possibilities and the limits of the most suitable model will be discussed.

3.1 Comparison of models for the interpretation of the Mößbauer spectra

For the comparison of the different Mößbauer models a sample of magnetic BNF nanoparticles has been investigated. These nanoparticles are characteristic of a multicore, built of ferrimagnetic iron oxide crystallites. This core is covered by a plain starch shell with a hydrodynamic diameter of 80 nm. The BNF particles have been characterised by high energy X-ray diffraction and Mößbauer spectroscopy at room temperature.

3.1.1 Interpretation of Mößbauer spectra from magnetite

In order to interpret Mössbauer spectra of nonstoichiometric magnetite above the Verwey transition temperature, different models are proposed. The first approach assumes that nonstoichiometric magnetite is a direct mixture of magnetite and maghemite [66]. Therefore, three independent sextets should be observed i.e. one for maghemite and two sextets for magnetite belonging to the A- and B-sites.

The second approach assumes that within nonstoichiometric magnetite the electron hopping process is a pair-localized phenomenon, which mainly takes place between octahedral pairs of Fe^{3+} and Fe^{2+} ions [67]. Here, the Mößbauer spectra of nonstoichiometric magnetite above the Verwey transition temperature is interpreted as two independent sextets. The first one corresponds to the iron ions with the mixed valence state $2.5+$ located at the octahedral sites. The second one is originated by the Fe^{3+} ions located at the tetrahedral sites and the Fe^{3+} ions located at the octahedral sites screening the vacancies.

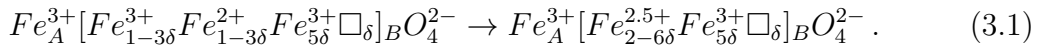
The third approach assumes that the electron hopping process is a completely delocalised phenomenon [68]. Here, a pool of electrons is supposed to be shared by all iron ions placed at the octahedral sites. In this case, the Mößbauer spectra of nonstoichiometric magnetite above the Verwey transition temperature is interpreted also as

an overlap of two Zeeman sextets. One sextet corresponds to the Fe^{3+} ions located at tetrahedral sites and second one to iron ions placed at the octahedral sites, but with the valence state $z+$ and $2.5 \leq z \leq 3.0$.

Furthermore, some approaches assume that a combination of the pair-localised and the band-delocalised mechanisms occur [22, 69].

For the needs of further discussion, the pair-localised model was assumed for the fitting of the spectra which does not suggest that the band-delocalised model is neglected. By assuming the pair-localised model, the amount of vacancies present in the magnetite structure can be determined from the relative intensity ratio $\beta = I(3+)/I(2.5+)$ of the Mößbauer spectrum. Parameter β equals $1/2$ for the stoichiometric Fe_3O_4 and ∞ for $\gamma\text{-Fe}_2\text{O}_3$.

Every vacancy located at the octahedral sites traps five Fe^{3+} ions:



Assuming that the Lamb-Mößbauer factor for Fe^{3+} and Fe^{2+} ions at both nonequivalent crystallographic sites are equal [24], β can be expressed by:

$$\beta = \frac{1 + 5\delta}{2 - 6\delta}, \quad (3.2)$$

where δ is the number of vacancies per formula unit.

3.1.2 High energy X-ray diffraction study

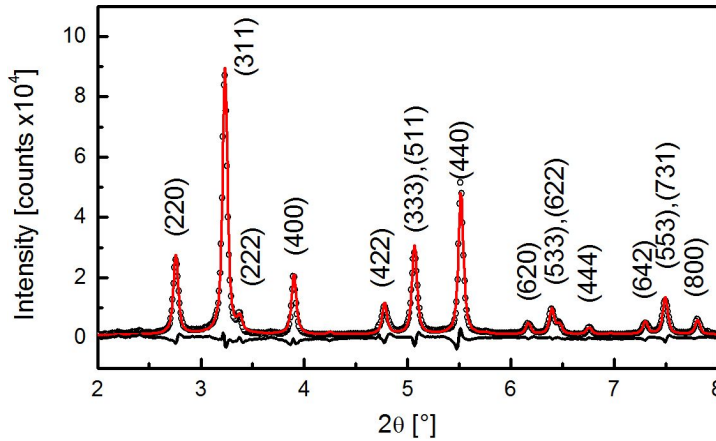


Figure 3.1: The high energy X-ray diffraction pattern of the BNF nanoparticles. Additionally, the fitted and the differential patterns are presented. Main peaks of Fe_3O_4 are labeled by corresponding Miller indices.

Fig. 3.1 presents the obtained experimental diffractogram, as well as, the fitted and the differential patterns for the investigated BNF nanoparticles. The main diffraction peaks of magnetite are labeled by corresponding Miller indices. It is worth mentioning that a small amount of goethite was detected in the sample, but due to its small fraction, this phase can be neglected. The weight fraction of magnetite and goethite, the crystal

unit edge for magnetite and its average crystallite size, as well as the Rietveld reliability factors [43], are collected in Tab. 5.1.

Fe_3O_4 wt%	FeOOH wt%	a [Å]	d [nm]	R_w	R_b
99.9 ± 0.6	0.1 ± 0.5	8.3720 ± 0.0002	22.4 ± 0.9	3.05	2.00

Table 3.1: Weight fractions of magnetite and goethite, crystal unit edge a and crystallite size d of magnetite, as well as Rietveld reliability factors R_w and R_b of the BNF nanoparticles.

Since magnetite has a cubic crystal structure, first the Popa model [70] was applied to derive the crystallite size. The Popa model describes the deviation of the crystallite shape from an ideal sphere using spherical harmonics in dependence of the Laue group. For the investigated nanoparticles, it was found that the deviation from an ideal spherical shape is insignificant to the extent allowing the assumption of spherical crystallites.

3.1.3 Mößbauer spectroscopy

For the ^{57}Fe Mößbauer spectroscopy investigation, the sample was prepared following the assumptions of the thin absorber approximation theory [56, 57].

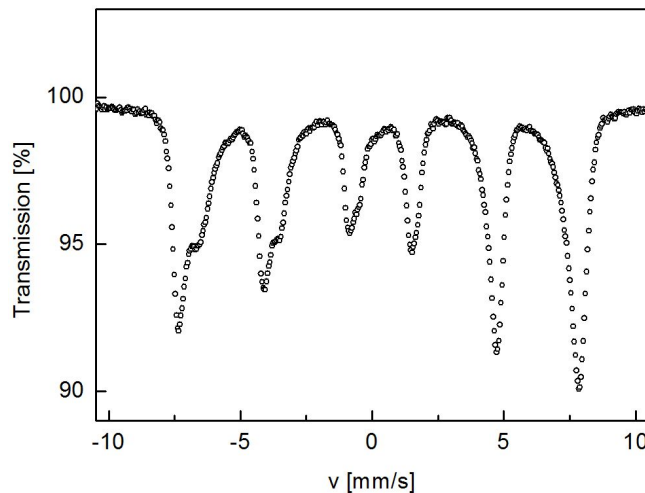


Figure 3.2: Transition Mößbauer spectrum of the blocked magnetic iron oxide nanoparticles at room temperature.

The obtained transmission Mößbauer spectrum of the BNF nanoparticles is presented in Fig. 3.2. The spectrum is a result of overlapping Zeeman sextets with a line broadening typical for BNF particles. Satisfactory statistics of counts was achieved with a signal to noise ratio (S/N) greater than 3000. Here, the signal is defined as the deepest minimum in the spectrum and the noise as the square root of the standard deviation from the background counts. It is worth to mention, that the goodness of the fit χ^2 for the Mößbauer spectra with a low S/N is smaller than for the one with a high S/N. But with a low S/N it is not possible to resolve different models [71].

The Mößbauer spectrum of the BNF nanoparticles was processed with the software Recoil [72] with implemented nonlinear least square fitting procedure. This software offers multiple number of fitting models which are realised with very efficient fitting routines. The spectrum was analysed according to the described structural model, taking into account the composition derived by high energy X-ray diffraction. For magnetite a set of two Zeeman sextets according to the pair-localised model and for goethite one sextet [73] was fitted. The resulting hyperfine parameters are collected in Tab. 3.2 and are explained in the following sections.

It is worth to mention that for the Voigt based fitting models the half width of the line obtained from the calibration ($\Gamma = 0.148(1)$ mm/s) was used as the minimal half width. Furthermore, the hyperfine parameters of goethite are presented only for the Lorentzian model. Despite the fact that the content of goethite is very small, it was included during all of the fitting procedures. However, its hyperfine parameters for different models had to be kept constant.

model	c	RI	Γ	IS	QS	$\mu_0 H_{hf}$	ρ_{IS-z}	ρ_{QS-z}	ρ_{IS-QS}
χ^2		[%]	[mm/s]	[mm/s]	[mm/s]	[T]			
Lorentz 9.01	A	44.3(1)	0.251(4)	0.307(2)	-0.015(2)	47.3(1)			
	B	54.2(1)	0.463(7)	0.530(4)	-0.027(3)	43.9(1)			
	G	1.5(5)	0.250 (fixed)	0.325(42)	-0.243(42)	38.8(9)			
Voigt 22.79	A	46.4(2)		0.271(2)	-0.000(2)	47.1(1) 1.1*			
	B	51.5(2)		0.561(4)	-0.048(4)	44.1(1) 2.7*			
xVoigt1 8.03	A	40.0(1)		0.296(2) 0.137*	-0.020(2)	47.3(1) 0.03*	-1		
	B	57.7(2)		0.514(5) 0.370*	-0.028(4)	43.9(1) 1.4*	-0.03		
xVoigt2 7.86	A	40.3(2)		0.296(2)	-0.017(2)	47.3(1) 0.136* 0.06*		0.76	
	B	57.8(2)		0.517(4)	-0.027(4)	43.9(1) 0.366* 1.3*		-0.06	
xVoigt3 7.53	A	40.9(1)		0.299(2) 0.085*	-0.022(2)	47.3(2) 0.3*	-0.81	0.64	-0.08
	B	56.7(1)		0.513(5) 0.069*	-0.023(4)	43.9(1) 0.346* 1.8*	0.15	-0.04	-0.47

Table 3.2: Composition and hyperfine parameters of the BNF nanoparticles obtained by different fitting models: c- component (A - magnetite A-sites, B - magnetite B-sites and G - Goethite), RI - relative intensity, Γ - half width of the line, IS - (mean) isomer shift, QS - (mean) quadrupole splitting, $\mu_0 H_{hf}$ - (mean) magnetic hyperfine field. Standard deviations of the mean value are indicated by *. ρ_{IS-z} , ρ_{QS-z} and ρ_{IS-QS} are the correlation parameters between the isomer shift and the magnetic hyperfine field, the quadrupole splitting and the magnetic hyperfine field, and the isomer shift and the quadrupole splitting, respectively. Additionally, the goodness of the fit χ^2 is given below the name of the fitting model.

3.1.4 Lorentz model

Lorentz model assumes that the Mößbauer spectrum is a superposition of n Lorentzian lines with

$$y(v_i, \mathbf{c}) = (E + F \cdot v_i + G \cdot v_i^2) + \sum_{k=1}^n \frac{A_k}{1 + \left(\frac{v_i - V_k(0)}{\Gamma_k/2}\right)^2}, \quad i = 1, 2, 3, \dots, N, \quad (3.3)$$

where v_i is the Doppler velocity, N is the number of data points in the spectrum, term $(E + F \cdot v_i + G \cdot v_i^2)$ describes the baseline and \mathbf{c} are $3n+3$ parameters (A_k , $v_k(0)$, Γ_k and E , F , G) to be determined [56]. A_k , $v_k(0)$ and Γ_k are the height, position and Lorentzian line width, respectively. A set of Lorentzian lines is fitted to the experimental data by minimising

$$\chi^2 = \sum_{i=1}^N w_i [y(v_i, \mathbf{c}) - y_i]^2 \rightarrow \min, \quad (3.4)$$

where w_i is indirectly proportional to y_i . A necessary condition is that

$$\frac{\partial \chi^2}{\partial c_j} = 0, \quad j = 1, 2, \dots, 3n + 3, \quad (3.5)$$

leading to a set of nonlinear simultaneous equations, which cannot be solved analytically [56]. Most commonly, \mathbf{c} is estimated and y approximated by a Taylor expansion taking into account only the linear term in \mathbf{c} . y is substituted in Eq. (3.4) obtaining a new set \mathbf{c} iteratively minimising χ^2 until a satisfactory convergence is reached.

The Mößbauer spectrum of magnetic nanoparticles can be interpreted by assuming two states of the magnetic hyperfine fields with the same size but opposite sign [74, 75]. The line shape does not change, but it shows a broadening $\Delta\Gamma$ proportional to the probability W of the transition between the two states.

$$\Delta\Gamma \simeq 2W \quad (3.6)$$

The Mößbauer spectrum of the BNF nanoparticles processed according to the Lorentz model is presented in Fig. 3.3. The experimental spectrum (dots), as well

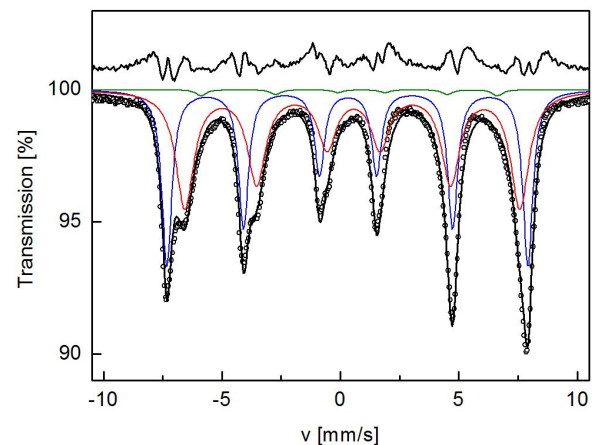


Figure 3.3: Transmission Mößbauer spectrum of the BNF nanoparticles at room temperature processed according to the Lorentz model. The fitted spectrum and the particular subspectra are presented by lines: blue - tetrahedral positions (A-sites) of magnetite, red - octahedral positions (B-sites) of magnetite and green - goethite. Additionally, the differential pattern is shown above the spectra.

as the fitted spectrum (black line) and particular subspectra (coloured lines), are indicated. Additionally, the differential pattern is shown above the spectra. Parameters resulting from the fitting procedure i.e. relative intensities, line widths and the hyperfine parameters are collected in Tab. 3.2.

Here, it is worth to mention that the ratios of particular lines A_3/A_2 and A_2/A_1 were treated as free parameters during the fitting procedure in order to compensate possible thickness effects. In the fitting procedures based on Voigt model, these ratios were kept constant.

For the stoichiometric bulk magnetite the hyperfine parameters are well known. More precisely, the isomer shifts with respect to α -iron at room temperature are 0.26 mm/s and 0.67 mm/s, the quadrupole splittings are 0.02 mm/s and 0.02 mm/s, and the magnetic hyperfine fields are 49.2 T and 46.1 T for A-sites and B-sites, respectively [73]. The hyperfine parameters obtained for the studied BNF nanoparticles differ from their counterparts known for the bulk magnetite. One reason for the changes of the hyperfine parameters is the stoichiometry of magnetite. The amount of vacancies per formula unit, according to Eq. (3.2), is $\delta = 0.064(5)$. If $\delta < 0.14$, the magnetic hyperfine field and the isomer shift are independent of the stoichiometry [24]. Therefore, the changes in the hyperfine parameters must result from the sizes of the nanoparticles. The changes in the isomer shift can be explained by the probability of the transition between two minimum energy states, following

$$\Delta IS \simeq \frac{W(2W + \frac{\Gamma}{2})}{2\alpha}, \quad (3.7)$$

where α is the isomer shift in the static case [74].

The reduction of the magnetic hyperfine fields can be explained by fluctuations of the magnetisation direction

$$M(V, T) = M_{bulk}(T) \langle \cos \vartheta \rangle_T, \quad (3.8)$$

$$\langle \cos \vartheta \rangle_T = \frac{\int_0^{\pi/2} \exp[-E(\vartheta)/kT] \cos \vartheta \sin \vartheta d\vartheta}{\int_0^{\pi/2} \exp[-E(\vartheta)/kT] \sin \vartheta d\vartheta}, \quad (3.9)$$

around one of the energy minima [76].

At temperatures far below the magnetic blocking temperature, $\langle \cos \vartheta \rangle_T$ can be approximated by $1 - kT/2KV$. Since the fluctuations of the magnetisation direction are fast as compared to the life time of the excited state of the Mößbauer nuclei, the magnetic hyperfine field should also be proportional to $\langle \cos \vartheta \rangle_T$ [76].

Applying the Lorentz model, all features of the spectrum can be reproduced and the changes of the hyperfine parameters can be explained taking into account the pair-localised model. The differential pattern for each line shows deviations from random noise, which are more pronounced for the magnetite A-sites. This suggests, that the desired line shape cannot be properly reproduced assuming only superpositions of single Lorentzian lines.

3.1.5 Voigt model

Since a system of nanoparticles consists not only of particles with a single particle size, it always shows a particle size distribution. According to Eq. (3.8), a particle size distribution leads to a distribution of the magnetisation, which results in a distribution of the magnetic hyperfine field.

In the simple Voigt model only the distribution of the magnetic hyperfine field is taken into account. Basically, Lorentzian lines occur only if a set of static hyperfine parameters is given which are completely determined regardless of experimental artifacts. However, when the electronic environment shows a time variation, the hyperfine parameters in the Hamiltonian can show an explicit time dependence, as well [77]. Extracting meaningful hyperfine parameter distributions is complex. The most widely used method is to describe these distributions via a step function method with smoothing, end point restrictions, as well as, positive value restrictions [77]. Taking into account that a great variety of distributions are Gaussians in the first approximation, it can be assumed that the true distribution of hyperfine parameters can be described by a set of Gaussian distributions $P(z)$ of the nuclear Zeeman splitting z , with different positions z_{0i} , widths σ_{zi} and weighting factors p_i [77]. In this case, the distribution of the magnetic hyperfine field is

$$P(z) = \sum_{i=1}^N p_i G_i(z_{0i}, \sigma_{zi}, z), \quad (3.10)$$

$$G_i(z_{0i}, \sigma_{zi}, z) = \frac{1}{(2\pi)^2 \sigma_{zi}} \exp \left\{ \frac{-(z - z_{0i})^2}{2\sigma_{zi}^2} \right\}. \quad (3.11)$$

The shape of the Mössbauer line $H(v)$ is given as a convolution of a Lorentzian and a Gaussian lines:

$$H(v) = \int_{-\infty}^{+\infty} S(v) P(z) dz, \quad (3.12)$$

$$S(v) = \sum_{i=1}^6 L_i(v_i, \Gamma, h_i, v), \quad (3.13)$$

with $S(v)$ being the elemental sextet with the Lorentzian line shape L characteristic of the center v_i , width Γ and the height h_i . With this the shape $H(v)$ can be approximated by

$$H(v) = \sum_{i=1}^N \sum_{k=1}^6 p_i V_{ik}(A_k + B_k Z_{0i}, |B_k| \sigma_{zi}, \Gamma, h_k, v), \quad (3.14)$$

where V_{ik} is the Voigt line profile defined as [77]:

$$V_i(z_{0i}, \sigma_{zi}, \Gamma, h, v) = \int_{-\infty}^{+\infty} L(z, \Gamma, h, v) G_i(z_{0i}, \sigma_{zi}, z) dz. \quad (3.15)$$

It is worth mentioning, that the analytic expression for the Voigt line profile is unknown,

but analytic approximations have been developed [78].

In the easiest approach, the Mößbauer spectrum was reconstructed as a set of only two Gaussian distributions of the magnetic hyperfine field for magnetite A- and B-sites. The Mößbauer spectrum of the BNF nanoparticles processed according to the Voigt model is shown in Fig. 3.4. The experimental spectrum (dots), as well as the fitted spectrum (black line) and particular subspectra (coloured lines), are indicated. Additionally, the differential pattern is presented above the spectra. Parameters resulting from the fitting procedure i.e. relative intensities, the hyperfine parameters and the widths of the Gaussian distributions, are collected in Tab. 3.2.

Application of the simple Voigt model with a distribution only of the magnetic hyperfine field does not lead to a satisfactory fit. The goodness of the fit χ^2 is 22.79 and strong deviations of the calculated spectrum from the experimental one can be observed. Moreover, in order to realize the desired line shape, the number of Gaussian distributions of the magnetic hyperfine field per site was increased to four. Neither in this case a satisfactory result was achieved and the goodness of the fit χ^2 was reduced only to 13.51.

Here the main problem becomes evident i.e. the application of only a distribution of the magnetic hyperfine field is not sufficient. It is due to the fact that in a small particle the surface to volume ratio is large and, therefore, the atoms located on the surface and close to it have a different chemical and physical environment than those in the center of the nanoparticle [15].

3.1.6 Extended Voigt based model

The extended Voigt based model is a generalised Voigt model which introduces independent distributions of all three hyperfine parameters, with any degree of correlations [79]. The assumptions are quite similar as in the case of the basic Voigt model. The Mößbauer spectrum corresponding to a set of hyperfine parameters $\vec{\mu}$ with a probability distribution function $P(\vec{\mu})$ can be described by [79]

$$H(v) = \int d\vec{\mu} P(\vec{\mu}) S(\vec{\mu}, v), \quad (3.16)$$

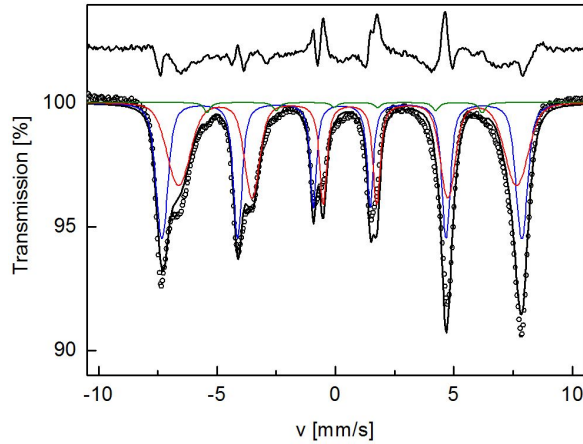


Figure 3.4: Transmission Mößbauer spectrum of the BNF nanoparticles at room temperature processed according to the Voigt model. The fitted spectrum and the particular subspectra are presented by lines: blue - tetrahedral positions (A-sites) of magnetite, red - octahedral positions (B-sites) of magnetite and green - goethite. Additionally, the differential pattern is shown above the spectra.

where $S(\vec{\mu}, v)$ is the elementary line shape which is normally described by a set of Lorentzians, as in Eq. (3.13) with the specific areas A_i . The generalised three dimensional probability density distribution is a function of the isomer shift IS , the quadrupole splitting QS and the Zeeman splitting z , leading to

$$H(v) = \sum_{i=1}^6 A_i \int_{-\infty}^{+\infty} dIS \int_{-\infty}^{+\infty} dQS \int_{-\infty}^{+\infty} dz P(IS, QS, z). \quad (3.17)$$

$$L_i(v - IS - \alpha_i QS - \beta_i z, \Gamma) \\ L(x, \Gamma) = \frac{\Gamma}{\pi} \frac{1}{x^2 + \Gamma^2}. \quad (3.18)$$

The probability density distribution for the analytical Mößbauer signal can be described by

$$P(IS, QS, z) = \sum_{i=1}^{n_{IS}} \sum_{j=1}^{n_{QS}} \sum_{k=1}^{n_z} \frac{P_{IS} P_{QS} P_z}{(2\pi)^{3/2} \sigma_{IS} \sigma_{QS} \sigma_z (1 - \rho_0)^{1/2}} \\ \exp \left\{ -\frac{1}{2(1 - \rho_0)} \left((1 - \rho_{QSz}^2) \frac{(IS - IS_{0i})^2}{\sigma_{ISi}^2} \right. \right. \\ \left. \left. + (1 - \rho_{ISz}^2) \frac{(QS - QS_{0j})^2}{\sigma_{QSj}^2} + (1 - \rho_{ISQS}^2) \frac{(z - z_{0k})^2}{\sigma_{zk}^2} \right. \right. \\ \left. \left. - 2(\rho_{ISQS} - \rho_{ISz} \rho_{QSz}) \frac{(IS - IS_{0i})(QS - QS_{0j})}{\sigma_{ISi} \sigma_{QSj}} \right. \right. \\ \left. \left. - 2(\rho_{ISz} - \rho_{ISQS} \rho_{QSz}) \frac{(IS - IS_{0i})(z - z_{0k})}{\sigma_{ISi} \sigma_{zk}} \right. \right. \\ \left. \left. - 2(\rho_{QSz} - \rho_{ISQS} \rho_{ISz}) \frac{(QS - QS_{0j})(z - z_{0k})}{\sigma_{QSj} \sigma_{zk}} \right) \right\}, \quad (3.19)$$

where ρ_{ISz} , ρ_{QSz} and ρ_{ISQS} are the correlation parameters smaller or equal one with

$$\rho_0 = \rho_{ISz}^2 + \rho_{QSz}^2 + \rho_{ISQS}^2 - 2\rho_{ISz} \rho_{QSz} \rho_{ISQS} \quad (3.20)$$

and the restriction $\rho_0 \leq 1$. σ_{ISi} , σ_{QSj} and σ_{zk} are the standard deviations of each distribution component [79]. The partially integrated probability densities of each hyperfine parameter are equal to a sum of Gaussian components, which do not depend on the correlation parameters between the hyperfine parameters. This leads to an arbitrary shape of the probability distribution which can be presented as a sum of Voigt functions [79]. It is worth to mention that in the extended Voigt based model the assumption of hyperfine parameters without a distribution leads to a Dirac delta function in the partially integrated probability distribution, which proves the consistency of the applied model [79].

The form of a Mößbauer spectra of nanoparticles is to a great extent influenced by the particle size distribution [76, 80]. Moreover, the contribution from the surface and the core of a crystallite of iron oxide nanoparticles should lead to different sets of observed hyperfine parameters and consequently, correlations between particular pairs

of hyperfine parameters should be observed.

Distributions of isomer shift and magnetic hyperfine field. The motivation to use a Voigt based model with distributions of the isomer shift and the magnetic hyperfine field is straightforward and there is no additional need for further discussion of different chemical and physical surroundings of the probed Mößbauer isotope in the particle.

Changes of the magnetisation direction are proportional to the magnetic hyperfine field of nanoparticles (Eq. (3.8)) and they also induce changes of the isomer shift (Eq. (3.7)) taking into account the particle size distribution [74, 75]. Therefore, a direct correlation between the two parameters should always be considered. The Mößbauer spectrum of the BNF nanoparticles processed according to the extended Voigt based model is presented in Fig. 3.5 with a correlation between the isomer shift and the magnetic hyperfine field. The experimental spectrum (dots), as well as, the fitted spectrum (black line) and particular subspectra (coloured lines), are indicated. Additionally, the differential pattern is shown above the spectra. Parameters resulting from the fitting procedure are collected in Tab. 3.2. In this case, the goodness of the fit $\chi^2 = 8.03$ and the differential pattern shows smaller deviations than for the Lorentzian model. The mean values of the hyperfine parameters are comparable to the one of the Lorentzian model, although small deviations subsist.

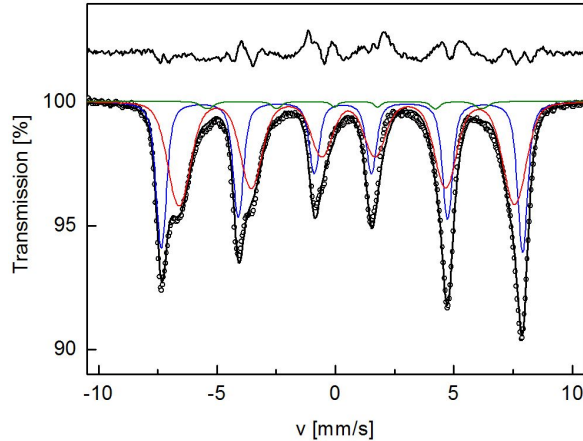


Figure 3.5: Transmission Mößbauer spectrum of the BNF nanoparticles at room temperature processed according to the extended Voigt model with a correlation between the isomer shift and the magnetic hyperfine field. The fitted spectrum and the particular subspectra are presented by lines: blue - tetrahedral positions (A-sites) of magnetite, red - octahedral positions (B-sites) of magnetite and green - goethite. Additionally, the differential pattern is shown above the spectra.

The derived correlation parameters are -1.00 and -0.03 for magnetite A- and B-sites, respectively. For a correlation value of ± 1 a complete correlation is present, while for a correlation value of 0 no correlation between these two hyperfine parameters is observed. Fig. 3.6 demonstrates the influence of the correlation parameters on the probability density distributions for magnetite A- and B-sites. For magnetite A-sites a strong correlation between the isomer shift and the magnetic hyperfine field was found, while there is no significant correlation observed for magnetite B-sites. Therefore, changes in the isomer shift and in the magnetic hyperfine field cannot only be a result of the particle size or the particle size distribution.

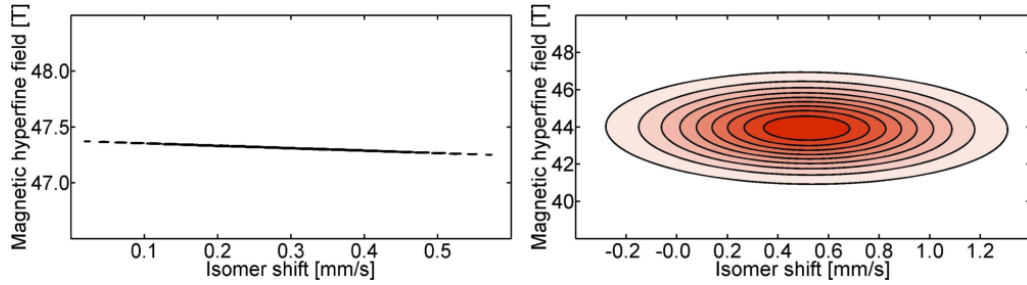


Figure 3.6: Maps of the probability density distributions of the isomer shift and the magnetic hyperfine field for magnetite A- and B-sites (left and right, respectively).

Distributions of quadrupole splitting and magnetic hyperfine field. Since magnetite is characteristic of a cubic structure, no quadrupole splitting should be observed. The BNF particles have a multicore structure with mainly one easy axis of magnetisation, leading to an effectively uniaxial anisotropy. In this case, there is a random angle ϑ between the magnetisation direction and the symmetry axis of the electric field gradient. When the electric quadrupole interaction is significantly smaller than the magnetic hyperfine interaction the quadrupole splitting is independent of m_I [81]

$$\epsilon = \frac{e^2qQ}{8}(3\cos^2\vartheta - 1). \quad (3.21)$$

For a multicore particle every ϑ is possible, therefore an averaging over all ϑ is necessary. This makes it difficult to determine the actual quadrupole splitting. Furthermore, the relatively large surface of the magnetite crystallites can show disorder and a break of the symmetry, therefore additional changes in the quadrupole splitting should be observed. The fluctuation of the magnetisation direction for different particle sizes should lead to an additional broadening of the magnetic hyperfine field distribution. Hence, a direct correlation between the quadrupole splitting and the magnetic hyperfine field should be observed.

The Mößbauer spectrum of the BNF nanoparticles processed according to the extended Voigt based model is presented in Fig. 3.7 with a correlation between the quadrupole splitting and the magnetic hyperfine field. The experimental spectrum (dots), as well as, the fitted spectrum (black line) and particular subspec-

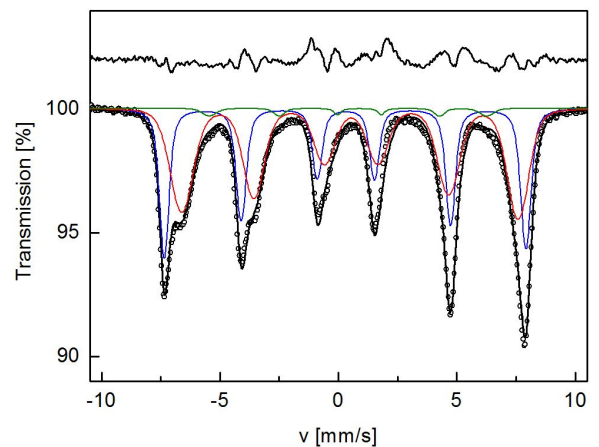


Figure 3.7: Transmission Mößbauer spectrum of the BNF nanoparticles at room temperature processed according to the extended Voigt model with a correlation between the quadrupole splitting and the magnetic hyperfine field. The fitted spectrum and the particular subspectra are presented by lines: blue - tetrahedral positions (A-sites) of magnetite, red - octahedral positions (B-sites) of magnetite and green - goethite. Additionally, the differential pattern is shown above the spectra.

tra (coloured lines), are indicated. Additionally, the differential pattern is shown above the spectra. Parameters resulting from the fitting procedure are collected in Tab. 3.2. In this case, the goodness of the fit $\chi^2 = 7.86$. The mean values of the hyperfine parameters are comparable to the one of the Lorentzian model, though small deviations subsist.

The obtained correlation parameters between the quadrupole splitting and the magnetic hyperfine field are 0.76 and -0.06 for magnetite A- and B-sites, respectively. The resulting probability density distributions are presented in Fig. 3.8. The A-sites of magnetite again shows a strong correlation between the two hyperfine parameters, whilst the B-sites barely shows any correlation between the the two parameters.

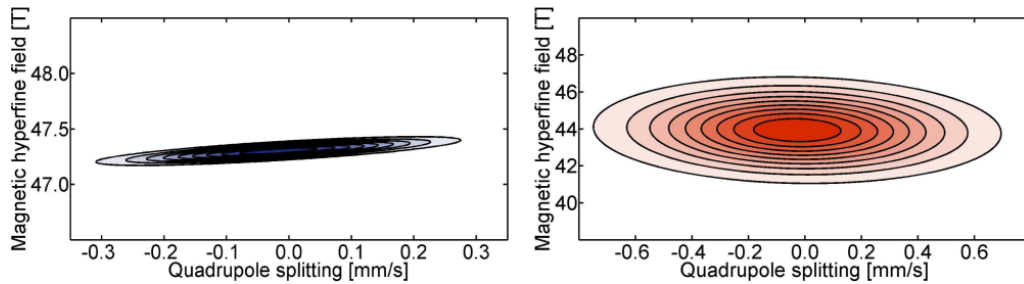


Figure 3.8: Maps of the probability density distributions of the quadrupole splitting and the magnetic hyperfine field for magnetite A- and B-sites (left and right, respectively).

Distributions of all hyperfine parameters. In this case of distributions of all hyperfine interaction parameters i.e. isomer shift, quadrupole splitting and magnetic hyperfine field, each distribution is described by one Gaussian. Furthermore, correlations between all three pairs of hyperfine parameters were taken into account.

The Mößbauer spectrum of the BNF nanoparticles processed according to the extended Voigt based model with a correlation between all hyperfine parameters, is presented in Fig. 3.9. The experimental spectrum (dots), as well as the fitted spectrum (black line) and particular subspectra (coloured lines), are indicated. Additionally, the differential pattern is shown above the spectra. Parameters resulting from the fitting procedure are collected in Tab. 3.2. In this case, the goodness of the fit $\chi^2 = 7.53$. The mean values of the hyperfine parameters are comparable to the one of the Lorentzian model, even though small deviations subsist. The resulting differential pattern is quite similar to the other presented cases, nevertheless the χ^2 is smaller.

The probability density distribution is actually a three dimensional function. In order to present the probability density distributions and to visualise accurately the correlations between all hyperfine parameters, two dimensional projections of the probability density distributions are presented in Fig. 3.10. Magnetite A-sites shows again a strong correlation between the isomer shift and the magnetic hyperfine field, as well as, a strong correlation between the quadrupole splitting and the magnetic hyperfine field. The correlation between the isomer shift and the quadrupole splitting is neglectable. Magnetite B-sites shows the exact opposite behaviour. The isomer shift and the magnetic hyperfine field show only a weak correlation while the correlation between the quadrupole splitting and the magnetic hyperfine field is insignificant. The correlation between the isomer shift and the quadrupole splitting appears to be dominant for magnetite B-sites.

The resulting correlations are ambiguous. The results discussed in the previous sections showed that correlations between the isomer shift and the magnetic hyperfine field, as well as the correlation between the quadrupole splitting and the magnetic hyperfine field, should be present. This was only observed for magnetite A-sites. It was indicated that magnetite B-sites are more affected by the surface to volume ratio of a crystallites and, therefore, also affected by the induced lattice strain, than magnetite A-sites [82]. This should also result in a bigger quadrupole splitting on the B-sites below the tem-

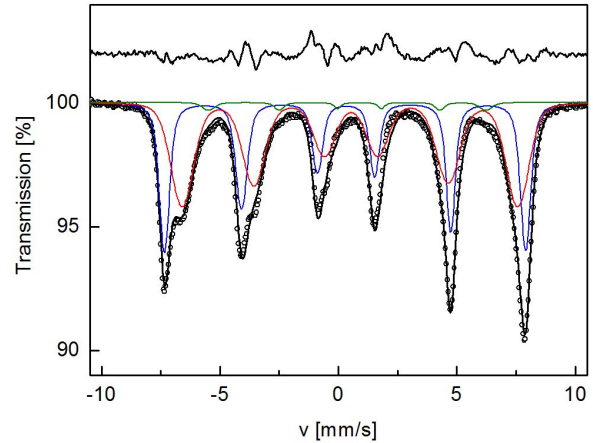


Figure 3.9: Transmission Mößbauer spectra of the BNF nanoparticles processed according to the extended Voigt based model with correlation between all hyperfine parameters. Additionally, the fitted spectrum, differential spectrum and the corresponding subspectra are presented. Blue - tetrahedral positions of iron ions (A-sites) of magnetite, red - octahedral positions (B-sites) of magnetite and green - goethite.

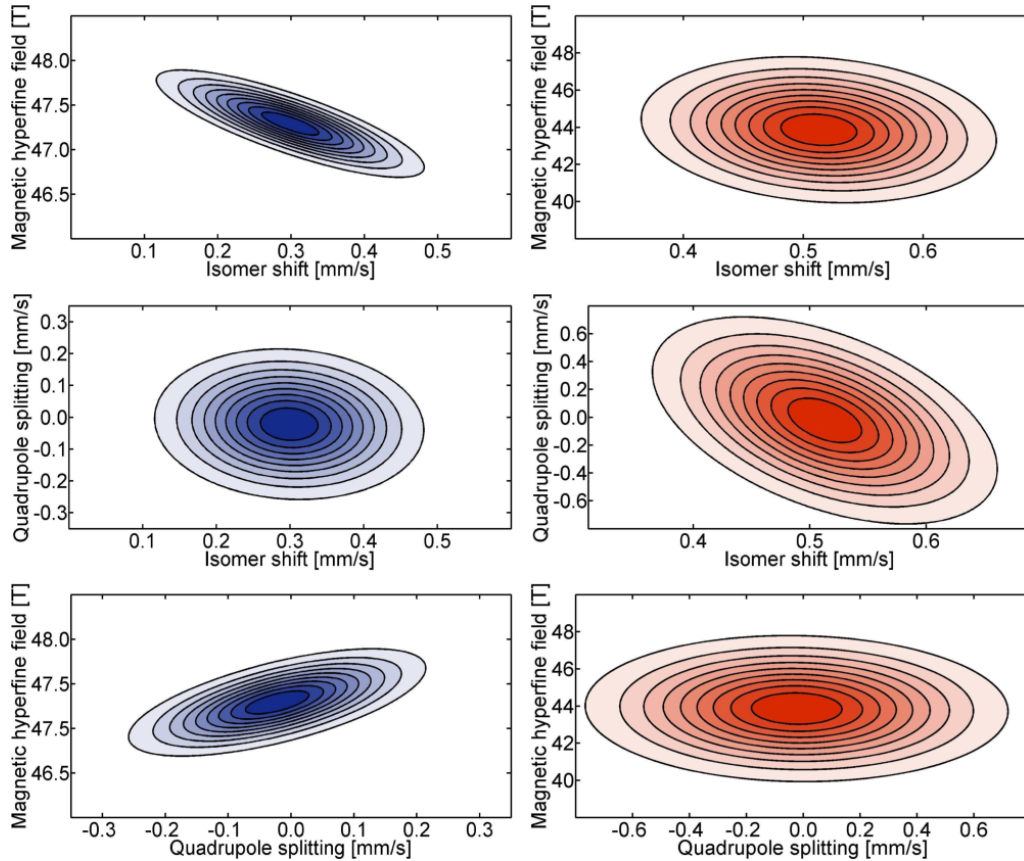


Figure 3.10: Maps of the probability density distributions as 2D projections of isomer shift and magnetic hyperfine field (top), isomer shift and quadrupole splitting (middle) and quadrupole splitting and magnetic hyperfine field (bottom). Left column: magnetite A-sites, right column: magnetite B-sites.

perature of the transition to the superparamagnetic state. It was observed, that the partially integrated probability distribution is significantly bigger for magnetite B-sites than for the A-sites. This indicates, that different effects are dominant at two different sites of magnetite. At magnetite B-sites, a pair-localised electron hopping is observed above the Verwey transition temperature. Here, intrinsic effects like lattice strain, stoichiometry, disorder, as well as surface effects appearing in nanoparticles can be dominant. At the A-sites (including iron ions excluded from the pair-localised hopping process) the behaviour can be dominated by whole-particle effects creating a possibility of observing changes in the hyperfine parameters due to particle size distributions.

3.2 Magnetite bulk material

As a reference sample, a theoretically pure magnetite powder from Puratronics with bulk like properties and a purity of magnetite with 99.95% was chosen. Fig. 3.11 shows the high energy X-ray diffraction pattern of the studied sample. Additionally to the cubic magnetite structure, a hexagonal structure corresponding to hematite was found in the powder.

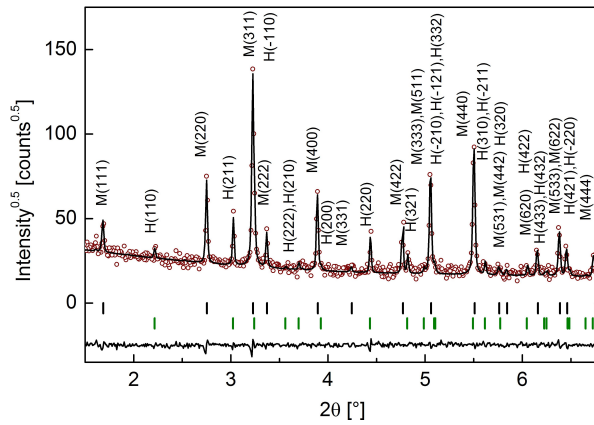


Figure 3.11: High energy X-ray diffraction patterns of the reference sample. Additionally, the fitted patterns and the differential patterns are presented. The main peaks of magnetite and hematite are labeled by corresponding Miller indices (magnetite - M, hematite - H) and furthermore Bragg reflexes of these phases are presented (magnetite - black, hematite - green).

tions of all hyperfine parameters and possible correlations between all of the hyperfine parameters. For this sample not only the experimental data but also the calculated one and the corresponding subspectra for magnetite are presented.

The volume fraction of magnetite is 89.4(5)%, while 10.6(5)% of the sample are oxidised to the stable α -phase of Fe_2O_3 , hematite. The derived crystal unit edges for magnetite and hematite are $a = 8.39115(7)$ Å and $a = 5.0327(7)$ Å, $c = 13.729(3)$ Å, respectively. The crystal unit edges derived for the reference sample are in good agreement with the values reported in literature [16]. The lines do not show broad peaks and the mean size of the crystallites was determined to be 286(8) nm for magnetite and 295(50) nm for hematite, which correspond to the particle sizes observed with the TEM (see Fig. A.1 in the appendix).

The corresponding Mößbauer spectra of the reference sample is presented in Fig. 3.12. The sample was fitted assuming the extended Voigt model with distribu-

sites	relative intensity [%]	IS [mm/s]	$\mu_0 H_{hf}$ [T]	QS [mm/s]	ρ_{ISQS}	ρ_{ISz}	ρ_{QSz}
hematite	8.0(5)	0.338(8) (0.002)	51.41(7) (0.03)	-0.091(8) (0.001)	0.989	-0.182	-0.031
magnetite A	36.7(4)	0.271(3) (0.001)	49.05(3) (0.14)	-0.009(3) (0.001)	-0.054	0.003	0.002
magnetite B	55.3(3)	0.668(2) (0.013)	45.96(2) (0.41)	-0.016(2) (0.001)	-0.004	0.000	-0.001
hematite*		0.370	51.75	-0.100			
magnetite A*		0.260	49.00	-0.002			
magnetite B*		0.670	46.00	0.000			

Table 3.3: Corresponding relative intensities, hyperfine parameters, variance of the distribution and correlation parameters of the corresponding sites of the reference sample as well as hyperfine parameters from literature marked by * [16, 73, 83].

The relative intensity can be interpreted as the fraction of the corresponding material when it is assumed that the Lamb-Mößbauer-factors for the different sites are equal at room temperature. The calculated relative intensities, the calculated hyperfine interactions, the variance of the hyperfine parameters as well as the correlation between the hyperfine parameters at room temperature are presented in Tab. 3.3. Furthermore, the hyperfine parameters from literature are summarized in Tab. 3.3 for comparison. The relative intensity of hematite was derived to 8.0% in the composition. Magnetite A-sites have a relative intensity of 36.7%, while the B-sites have 55.3% leading to the conclusion of non-stoichiometric magnetite with 0.110 as the number of vacancies per formula unit. For magnetite only the mean magnetic hyperfine fields and the mean isomer shift for magnetite B-sites show a small variance which can be related to the nonstoichiometry and the electron hopping process on the B-sites, which is often discussed as a broadening of the width of the lines of magnetite B-sites assuming a Lorentzian model [84].

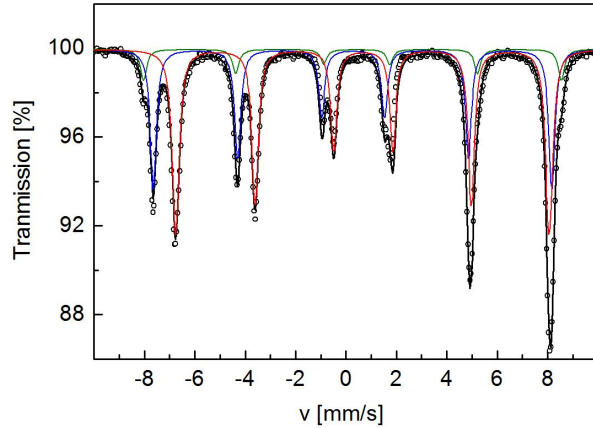


Figure 3.12: Mößbauer spectrum of the studied reference sample taken at room temperature. Additionally, the fitted spectra and the corresponding subspectra are presented. Blue - tetrahedral positions of iron ions in magnetite, red - octahedral positions of iron ions in magnetite and green - hematite.

3.3 Time dependant hyperfine interactions

To show the influence of size effects on the hyperfine interactions, a series of nanoparticles have been synthesised. Therefore, mixtures of ferrous chloride tetrahydrate ($\text{FeCl}_2 \cdot 4\text{H}_2\text{O}$) and ferric chloride hexahydrate ($\text{FeCl}_3 \cdot 6\text{H}_2\text{O}$) were blended in an excess of sodium hydroxide (NaOH) [85]. All the reagents were weighted using a precise laboratory balance and an overview of the used materials for each sample is presented in the appendix, Tab. A.1. For each sample the weight fraction of initially used Fe^{3+} -ions, defined as

$$\zeta(\text{Fe}^{3+}) = \frac{m(\text{Fe}^{3+})}{m(\text{Fe}^{3+}) + m(\text{Fe}^{2+})}, \quad (3.22)$$

was changed.

The iron chlorides and the sodium hydroxide were grinded separately for several minutes and afterwards the powders were blended together constantly during the whole reaction. A lot of heat and vapor was released. The mixture cooled down and was washed with water several times, until a pH-value of around 7 was reached. Afterwards the mixture was dried. The obtained powders were studied in a transmission electron microscope Libra 120, Carl Zeiss AG. To illustrate the changes in the morphology and

the particle size, exemplary pictures of each sample are presented in the appendix Fig. A.2. With an increasing amount of Fe^{3+} ions a significant decrease of the particle size of the powder was observed.

Fig. 3.13 shows the experimental and calculated diffraction pattern, as well as the differential pattern. The synthesised powders are composed not only of magnetite but they also contain smaller amounts of goethite and iron. The main peaks of the corresponding phases in Fig. 3.13 are labeled by Miller indices. The resulting composition, the crystal unit edge and the crystallite size for magnetite are presented in Tab. 3.4. A drastic increase in the line width of the spectra can be seen in Fig. 3.13 for large ζ . With the reduction of the particle size, the diffraction peaks show significant broadening. This makes the interpretation of the diffractogram for the nanoparticles with $\zeta = 1$ especially challenging.

The obtained Mößbauer spectra were fitted by the least square method assuming the extended Voigt based model where every hyperfine interaction parameter can show a distribution and correlations between all pairs of hyperfine parameters are possible.

The spectra are shown in Fig. 3.14. Additionally, the calculated spectra are presented for each sample. According to the high energy X-ray diffraction study, the spectra were fitted assuming a three component system. Goethite is antiferromagnetic [16, 73] and iron ferromagnetic at room temperature, both showing a single sextet. Magnetite shows two sextets which are related to different positions (A- and B-sites) in the crystal lattice [16, 73, 86]. The observed doublet was identified as the superparamagnetic state of magnetite.

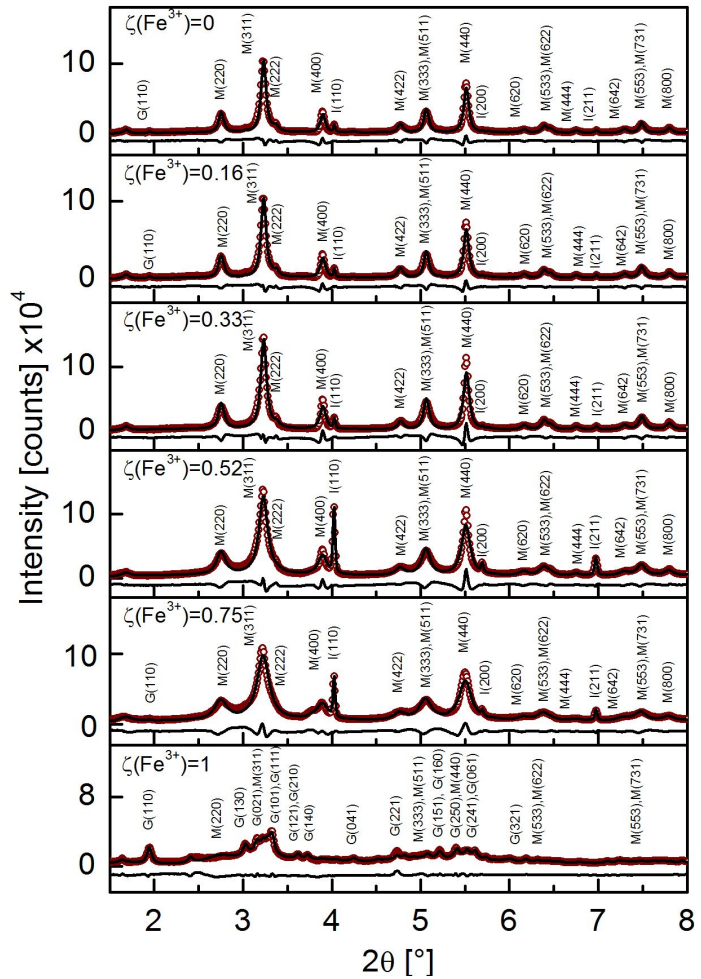


Figure 3.13: High energy X-ray diffraction patterns of the precipitated nanoparticles. Additionally, the fitted patterns and the differential patterns are presented. The main peaks of magnetite, goethite and iron are labeled by corresponding Miller indices (magnetite - M, goethite - G and iron - I).

$\zeta(\text{Fe}^{3+})$	weight fraction [%]			a [Å]	d_{XRD} [nm]	d_{TEM} [nm]	δ
	Fe_3O_4	FeOOH	Fe				
0	98.7(0.6)	0.9(0.3)	0.4(0.1)	8.3744(2)	16.3(0.3)	19.3(1.5)	0.126(12)
0.16	97.2(0.5)	2.0(0.2)	0.8(0.3)	8.3744(2)	15.8(0.4)	16.7(1.5)	0.121(9)
0.33	98.2(0.7)	0.0(0.2)	1.8(0.2)	8.3733(3)	14.0(0.1)	15.7(2.0)	0.164(15)
0.52	95.0(0.2)	0.0(0.2)	5.0(0.3)	8.3820(2)	8.5(0.1)	7.4(0.9)	0.144(22)
0.75	97.7(0.2)	0.9(0.4)	1.4(0.3)	8.3918(3)	5.8(0.1)	3.9(0.5)	-
1.00	62.6(0.4)	37.4(0.4)	-	8.4158(9)	2.1(0.3)	-	-

Table 3.4: Determined phase composition as well as crystal unit edges (a) and particle sizes (d_{XRD} and d_{TEM}) of magnetite for the precipitated powders derived by X-ray diffraction and transmission electron microscopy as well as the number of vacancies per formula unit of magnetite (δ).

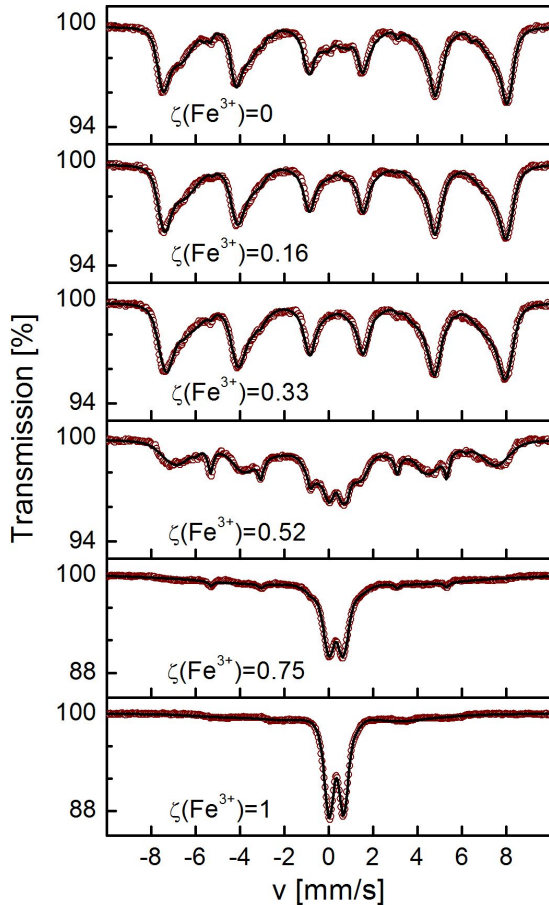


Figure 3.14: Mößbauer spectra of the coprecipitated nanoparticles derived at room temperature. Additionally, the fitted spectra are presented.

The composition was calculated from the XRD pattern as well as from the Mößbauer spectra. The results from the X-ray diffraction are presented in Tab. 3.14 and the composition calculated from the Mößbauer spectra in Fig. 3.15. The resulting compositions derived from both methods show the same behaviour and are in good agreement with one another. The main compound in every sample is magnetite. For the samples with $\zeta = 0, 0.16, 0.33, 0.52$ and 0.75 over 90% of the powder is magnetite. Two additional phases, namely goethite and iron, are present in each of these samples. For $\zeta = 1.0$, the volume fraction of magnetite is significantly smaller and only goethite was observed as an additional phase.

As shown in Fig. 3.15 applying Mößbauer spectroscopy, another feature becomes visible. Two regimes of magnetite can be distinguished - the blocked magnetic state and the state in which superparamagnetic relaxation occurs. This state appears when the magnetic anisotropy energy, mostly approximated by an uniaxial model according to

$$E_a = KV \sin^2 \vartheta, \quad (3.23)$$

where K is the effective anisotropy constant, V the volume and ϑ the angle between the magnetisation vector and the easy direction of magnetisation, is in the regime of the thermal energy. In this case, the thermal energy is sufficient to induce a reversal of the magnetisation between directions close to $\vartheta = 0^\circ$ and $\vartheta = 180^\circ$ [4, 87]. The typical

relaxation time can be described by

$$\tau = \tau_0 \cdot \exp \frac{KV}{kT}, \quad (3.24)$$

where τ_0 is in the order of 10^{-10} to 10^{-13} s, k is the Boltzmann constant and T the temperature. Superparamagnetic relaxation is observed when the time scale of the used experimental technique is bigger than the relaxation time τ . A sample of particles always consists of particles with a size distribution, therefore, some particles can be in the superparamagnetic state and others still in the blocked state.

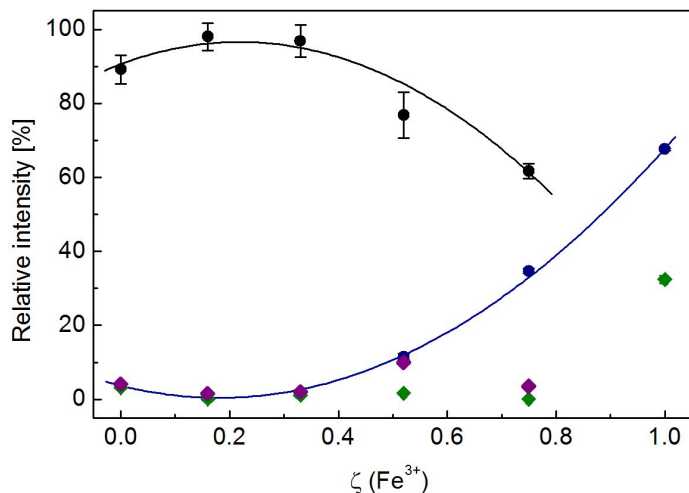


Figure 3.15: Relative area of the corresponding phases as a function of the weight fraction of Fe^{3+} -ions (black dots - ferromagnetic magnetite A- and B-sites, blue dots - superparamagnetic magnetite, green diamond - goethite, purple diamond - iron).

It is also possible to distinguish between blocked ferromagnetic and superparamagnetic fraction of magnetite in each Mößbauer spectra. The amount of magnetite in the stable ferromagnetic and the superparamagnetic state as functions of the weight fraction of Fe^{3+} ions can be described by parabolas. The stable ferromagnetic fraction of magnetite can be described by $f = (90.62 + 54.65 \cdot \zeta - 124.88 \cdot \zeta^2)\%$ and the superparamagnetic fraction by $f = (3.67 - 36.12 \cdot \zeta + 100.21 \cdot \zeta^2)\%$. Since, as a rule, the numerical parameters in the fitted formulae have no physical significance, these formulae should be treated only as a way to obtain approxi-

mate tabular data on the studied physical parameters.

Further details on the crystal unit edges and particle size of Fe_3O_4 are presented, see Fig. 3.16. The crystal unit edge of magnetite is approximately constant for small weight fraction of Fe^{3+} ions and increases exponentially with increasing ζ . The change in the crystal unit edge can be described by an exponential function according to $a = (8.37367 + 7.03995 \cdot 10^{-4} \cdot \exp[\zeta/0.23689]) \cdot \text{Å}$. The change of the crystal unit edge of magnetite with decreasing particle size can be induced by excessive lattice strain [82, 88]. But in this case, instead of an decrease in a crystal unit edge [82, 88, 89] a slight increase was observed.

Additionally presented in Fig. 3.16 are the crystallite sizes of magnetite derived from the X-ray diffractograms and the mean particles sizes derived by transmission electron microscopy. The results from both methods are in good agreement with one another, leading to the conclusion of monocrystalline nanoparticles. The particle size as a function of ζ can be described by a linear function, where the particle size decreases with increasing amount of Fe^{3+} ions used in the synthesis. The particle sizes derived from XRD can be described by the function $d = (17.7 - 15.6 \cdot \zeta) \cdot \text{nm}$ and the mean particle diameter from TEM by $d = (19.5 - 20.9 \cdot \zeta) \cdot \text{nm}$. It is worth to mention that the $\zeta = 1.0$ was excluded from the evaluation, because the granulation of the background was in the same size regime as the particle size of the sample. Furthermore, a strong agglomeration of the particles in this sample was observed.

A similar behaviour was discussed in [85]. A decrease in the particle size from 10 nm to 3 nm was noticed for an increasing amount of Fe^{3+} ions used in the synthesis process.

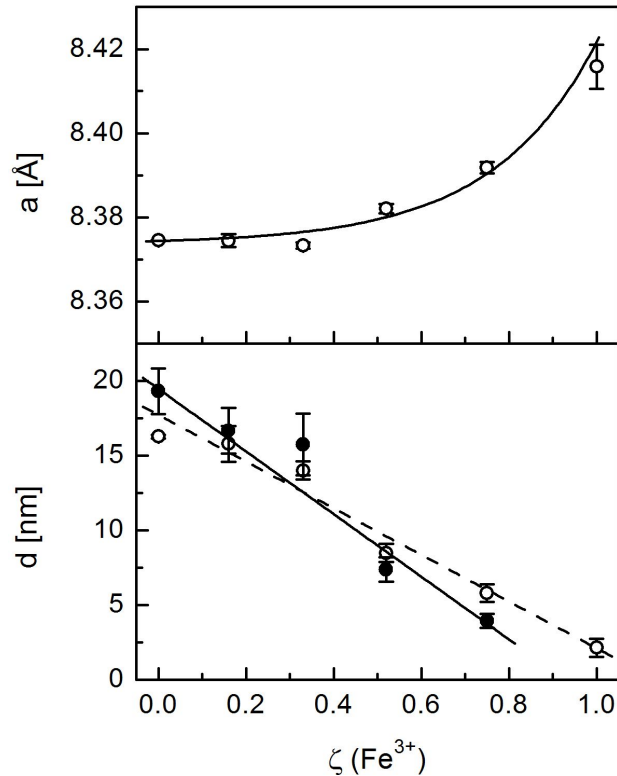


Figure 3.16: The crystal unit edge of magnetite and the mean particle diameter as a function of the weight fraction of Fe^{3+} ions (derived by TEM and XRD: open dots - XRD, black dots - TEM

3.3.1 Hyperfine interactions of magnetite in the blocked state

The investigated precipitated nanoparticles show a gradual change from sextets to a doublet with very broad lines. This is characteristic for the intermediate state between blocked ferrimagnetic and superparamagnetic state. For long relaxation times ($\tau = 5 \cdot 10^{-8}$ s), clear sextets are observed corresponding to a blocked ferro- or ferrimagnetic state, while for short relaxation times ($\tau = 1 \cdot 10^{-10}$ s) a superparamagnetic doublet can be observed [76]. Fig. 3.17 presents the calculated mean hyperfine parameters of the ferromagnetic blocked phase of magnetite.

The mean isomer shift of magnetite A-sites is constant and it only shows a tendency to increase. It can be presented as $IS_A = (0.2999 + 0.0871 \cdot \zeta) \cdot mm/s$. The change in the B-sites is rather pronounced and can be described also by a linear function according to $IS_B = (0.4416 - 0.0800 \cdot \zeta) \cdot mm/s$. The isomer shift of the B-sites shows a decrease from $\zeta = 0$ to $\zeta = 0.52$. This can be an influence of the nonstoichiometry of magnetite, where the vacancies predominantly occur on the B-sites of magnetite [67], or it can be interpreted as an influence of the particle size where the surface to volume ratio drastically increases [90]. A tendency of the vacancies to increase in dependence of ζ was observed and is shown in Tab. 3.4.

The mean magnetic hyperfine field of magnetite A- and B-sites are both decreasing with an increasing ζ . The diminishment in the magnetite B-sites is stronger than in the A-sites. In these cases, the behaviour can be described by logistic functions according to $(\mu_0 H_{hf})_A = (48.025 / (1 + [\zeta / 0.943]^{4.415})) \cdot T$ and $(\mu_0 H_{hf})_B = (44.148 / (1 + [\zeta / 0.579]^{6.171})) \cdot T$ for A- and B-sites, respectively. All the observed mean magnetic hyperfine fields for the two sextets are smaller compared to bulk magnetite [16]. This reduction in the mean magnetic hyperfine field can be explained by fast fluctuations of the magnetisation vector near the easy axis. These fluctuations are fast compared to the life time of an excited state in the Mößbauer experiment. The magnetic hyperfine field is proportional to the average value of the fluctuating magnetic hyperfine field [76], as shown in Eq. (3.8). The mean magnetic hyperfine field of magnetite B-sites decreases faster than the mean magnetic hyperfine field of the A-sites, which was explained in [82] as a strong electric

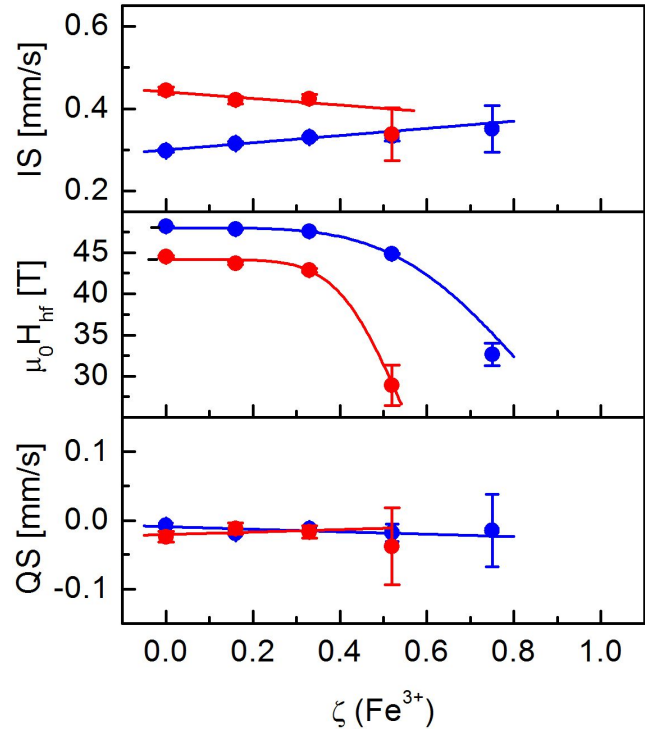


Figure 3.17: Hyperfine parameters, i.e. isomer shift - IS, magnetic hyperfine field - $\mu_0 H_{hf}$ and quadrupole splitting - QS of magnetite as functions of the weight fraction of Fe^{3+} ions. Magnetite A-sites is presented with blue dots, B-sites with red dots.

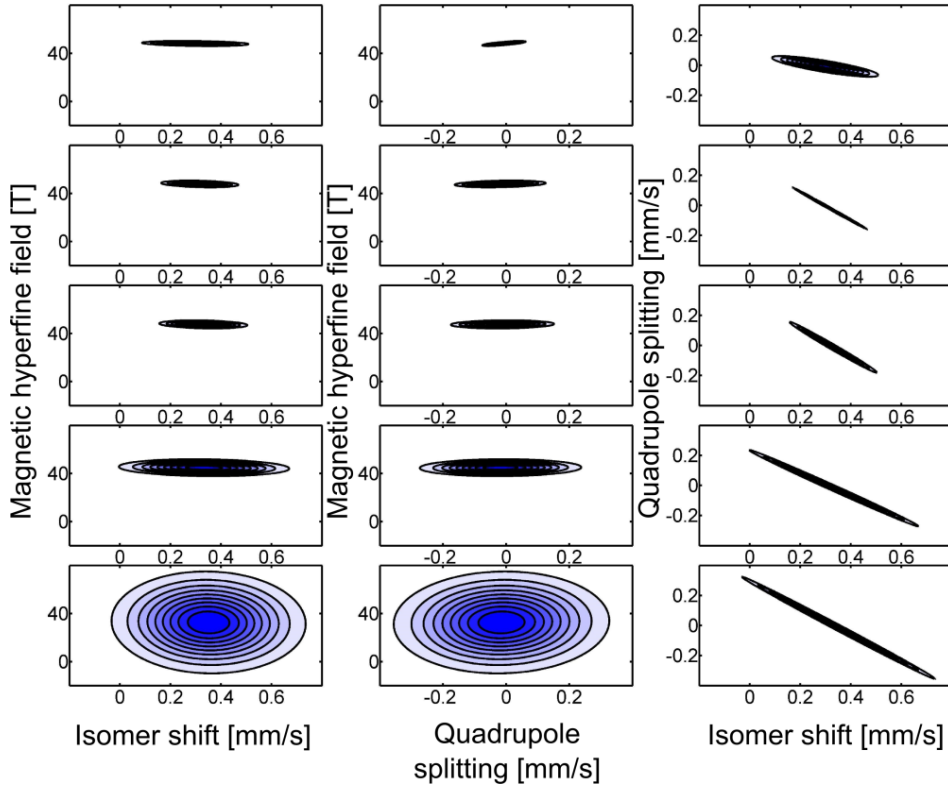


Figure 3.18: Maps of the probability density distributions as 2D projections of isomer shift and magnetic hyperfine field (left) and quadrupole splitting and magnetic hyperfine field (middle) isomer shift and quadrupole splitting (right) for magnetite A-sites. First line: $\zeta = 0$, second line: $\zeta = 0.16$, third line: $\zeta = 0.33$, fourth line: $\zeta = 0.52$ and fifth line: $\zeta = 0.75$.

field gradient due to the huge surface to volume ratio, which influences the B-sites more than the A-sites. Here, it is worth mentioning that the spectra for $\zeta = 0.75$ was fitted assuming only a single sextet for magnetite, which would correspond to magnetite A-sites.

The mean quadrupole splitting for both sites is constants and shows only a tendency to decrease or increase. The quadrupole splitting of magnetite A-sites can be expressed by $QS_A = (-0.0090 - 0.0184 \cdot \zeta) \cdot mm/s$ and the quadrupole splitting of the B-sites by $QS_B = (-0.0207 + 0.0186 \cdot \zeta) \cdot mm/s$.

Two dimensional projections of the probability density distributions are presented in Fig. 3.18 and Fig. 3.19 for magnetite A- and B-sites, respectively.

For magnetite A-sites the isomer shift and the magnetic hyperfine field as well as the quadrupole splitting and the magnetic hyperfine field show only weak or no correlation for the whole series, while a strong correlation can be observed between the isomer shift and the quadrupole splitting. The partially integrated probability distribution for the magnetic hyperfine field shows a drastic broadening with increasing ζ , which is related to the reduction of the particle size as well as the broadening of the size distribution of the nanoparticles. For magnetite B-sites stronger correlations between the isomer shift and the magnetic hyperfine field, as well as, the quadrupole splitting

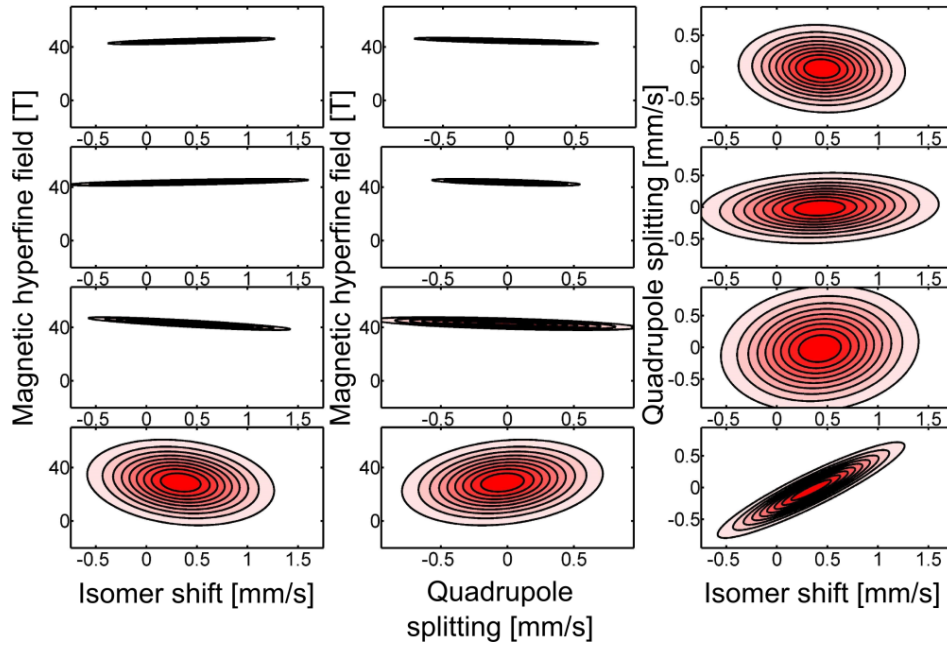


Figure 3.19: Maps of the probability density distributions as 2D projections of isomer shift and magnetic hyperfine field (left) and quadrupole splitting and magnetic hyperfine field (middle) isomer shift and quadrupole splitting (right) for magnetite B-sites. First line: $\zeta = 0$, second line: $\zeta = 0.16$, third line: $\zeta = 0.33$ and fourth line: $\zeta = 0.52$.

and the magnetic hyperfine field are visible, while only a weak correlation is seen for the isomer shift and the quadrupole splitting. Only for the sample with $\zeta = 0.52$ a stronger correlation is observed. The samples $\zeta = 0.52$ and 0.75 are in the transition state from the blocked ferrimagnetic state into the superparamagnetic, therefore, the assumption of an effectively static Hamiltonian to fit the spectra is not valid what is also to be seen in the overstated broadening of the partially integrated probability distributions for the samples with $\zeta = 0.52$ and 0.75 for magnetite B- and A-sites, respectively. Nevertheless, the tendencies of the hyperfine parameters can still be seen and also used to interpret the spectra.

It was indicated that magnetite B-sites are more affected by the surface to volume ratio of a crystallite and, therefore, also affected by the induced lattice strain than magnetite A-sites [82]. This should also result in a bigger quadrupole splitting on the B-sites below the transition temperature to the superparamagnetic state. It was observed that the partially integrated probability distribution is significantly bigger for magnetite B-sites than for the A-sites. Together with the different correlation behaviour of the two sites, this also supports the assumption that different effects are dominant at two different sites of magnetite.

3.3.2 Hyperfine interactions of magnetite in the superparamagnetic state

Fig. 3.20 presents the calculated mean hyperfine parameters of the superparamagnetic state of magnetite. The influence of the superparamagnetic state increases with increasing amount of Fe^{3+} ions used during the coprecipitation process. The mean hyperfine parameters of the observed doublet were interpreted as superparamagnetic magnetite which actually consists of two overlapping doublets of A- and B-sites [82]. The changes in the mean hyperfine parameters for the superparamagnetic magnetite are shown in Fig. 3.18. It is worth to mention that only the mean hyperfine parameters for the superparamagnetic magnetite for $\zeta = 0.52, 0.75$ and 1 are shown, since the fraction of magnetite in this state is significantly bigger than in the other samples and the hyperfine parameters are reliable.

The mean isomer shift shows a tendency to increase. This behaviour can be described by the linear function $IS_{SP} = (0.2642 + 0.0826\zeta) \cdot \text{mm/s}$. The changes of the mean value for the quadrupole splitting can be described by an exponential function according to $QS_{SP} = (0.6605 - 4.2428 \cdot \exp[-\zeta/0.1474]) \cdot \text{mm/s}$. The derived parameters are in good agreement with the parameters reported in [88], while smaller quadrupole splitting was reported in [82]. This can be a result of the nonstoichiometry of the magnetite sample. Whereas a small quadrupole splitting of around 0.4 mm/s is related to a more magnetite like behaviour, a bigger quadrupole splitting can be interpreted as a more maghemite like behaviour.

The probability density distributions for the isomer shift and for the quadrupole splitting are presented in Fig. 3.21. For $\zeta = 0.52$ and 0.75, the quadrupole splitting shows a bigger broadening, which is probably related to the transition into the superparamagnetic state taking place in this regime.

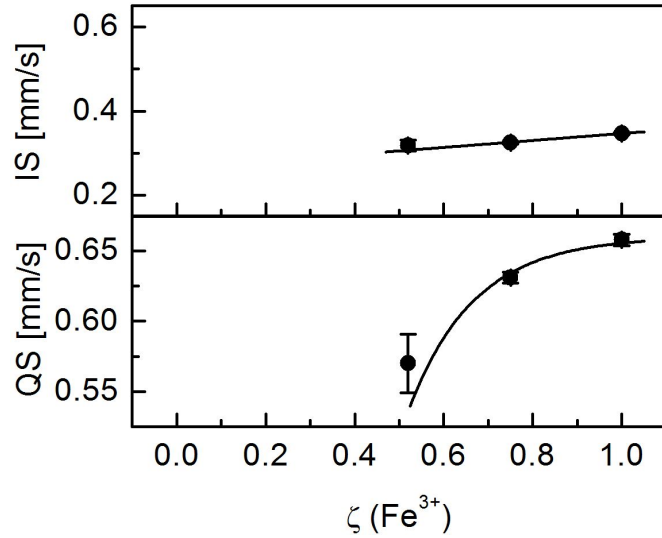


Figure 3.20: Hyperfine parameters, i.e. isomer shift - IS and quadrupole splitting - QS of the superparamagnetic state of magnetite as a function of the weight fraction of Fe^{3+} ions.

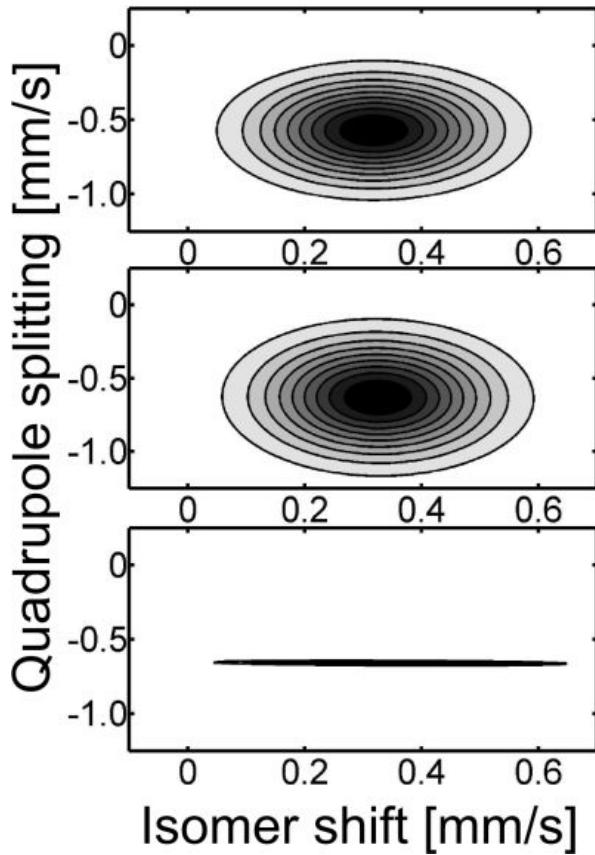


Figure 3.21: Maps of the probability density distributions of the isomer shift and quadrupole splitting for superparamagnetic magnetite. First line: $\zeta = 0.52$, second line: $\zeta = 0.75$ and third line: $\zeta = 1$.

dimensions this information can be lost due to the presence of goethite.

The distribution of the isomer shift stays approximately constant and is relatively broad which is probably related to the two overlapping sites from magnetite, having different chemical surrounding as well as the extremely huge surface to volume ratio. Between the two hyperfine parameters no correlation for all samples was observed.

In the studied series, the additional presence of ferrihydrates cannot be excluded. The hyperfine parameters of ferrihydrates at room temperature [16] are comparable to the observed parameters. The obtained diffractogram also gives the possibility to discuss the presence of ferrihydrates. With the small particle size and extremely broad diffraction peaks the fitting procedure assuming a cubic as well as hexagonal structures lead to comparable goodness of the fit. This presence of ferrihydrates could explain the increase of the lattice parameters instead of the normally observed decrease according to an increasing amount of vacancies in the structure. But since the particles have small

3.4 Time independent hyperfine interactions

As seen in the previous section, the application of the extended Voigt model has limitations. In the case of the transition of magnetic nanoparticles to the superparamagnetic state, the transition cannot properly be described by the extended Voigt model. The assumption of the effectively static Hamiltonian is not valid in this case. Nevertheless, the model can still be used to study the changes of the mean values of the hyperfine parameters.

For the further discussion of nanostructured iron oxide composites, the Hamiltonian can be described as effectively static. In this case, large samples are investigated, which differ from conventional bulk material due to their nanostructured grains. Fig. 3.22 shows schematically the grain boundary between three crystallites. At the boundary of grains, the atoms show a breaking of the symmetry or as well a change in the interatomic distances. Therefore, these atoms have different electronic environments, leading to different hyperfine interaction parameters of the Mößbauer nuclei.

Since the influence of the grain size and the influence of the grain boundary on the electronic structure of iron oxide composites is in the main focus of this work, the extended Voigt model with possible distributions of all hyperfine interactions and possible correlations between all of the hyperfine parameters was applied to interpret the Mößbauer spectra.

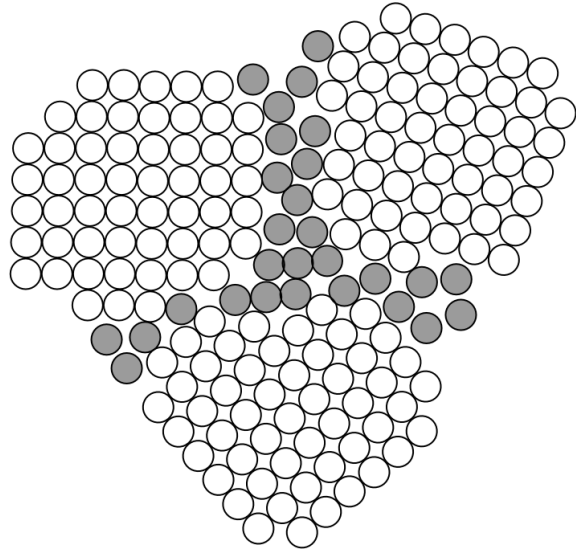


Figure 3.22: Schematics of the grain boundary of three crystallites.

Chapter 4

Nanostructured iron oxide composites

In this chapter different series from iron oxide precursors sintered at different temperatures will be presented to study the influence of the grain structure on the composition of the post-sintered composites and also the hyperfine interaction parameters. In the frame of this work, the main focus is on the hyperfine interaction parameters of magnetite A- and B-sites. Therefore, only these hyperfine interaction parameters and their distributions as well as correlations will be further discussed.

4.1 Systematics

In order to study the influence of the grain size on the hyperfine interactions in nanostructured bulk materials based on magnetite, two different approaches were followed to synthesise magnetite utilising the field assisted sintering technique.

In the first approach, a stoichiometric mixture of hematite and iron was synthesised, following the assumed reaction



In this approach, two different particles sizes of the precursor powders were chosen, which were also determined by TEM and are summarised in Tab. 4.1.

In the second approach, magnetite was directly chosen as a precursor using two different initial grain sizes of the precursor powders. The mean particle sizes of the initially used magnetite nanoparticles were derived by transmission electron microscopy and are summarised in Tab. 4.1.

precursor	hematite and iron		magnetite
	hematite	iron	
d_1 [nm]	190(10)	220(60)	120(35)
d_2 [nm]	26(3)	160(40)	27(2)

Table 4.1: Initial particle sizes for the different precursor materials used for the synthesis process.

Further information on the used precursor materials are summarised in the appendix. All samples were designed to have a thickness of approximately 4 mm. The appropriate amounts of powders were weighted using a precise laboratory balance and in order to ensure homogeneity of the hematite and iron precursor blended in grinding jars for 20 min. The obtained mixtures were placed in graphite dies with an inner diameter of 40

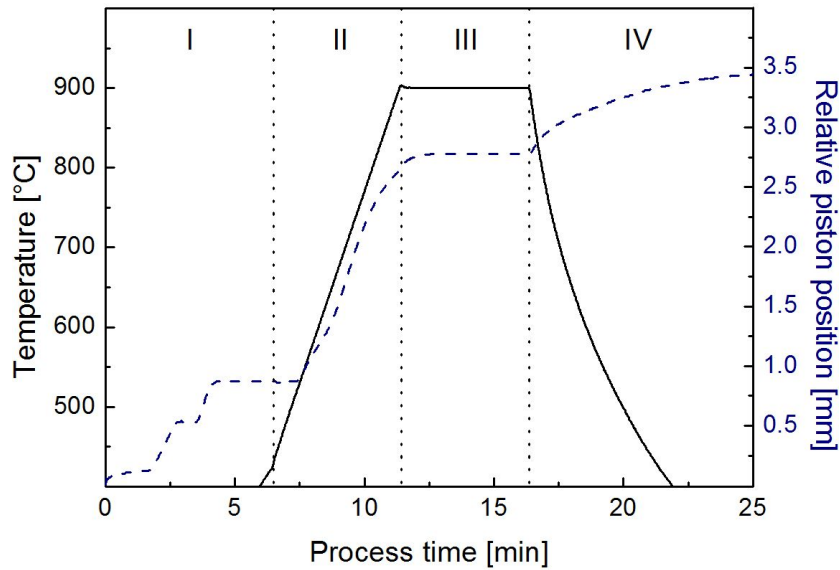


Figure 4.1: Exemplary sintering process of a sample from hematite and iron precursor sintered at 900°C. The black line shows the applied temperature profile, the blue dashed line the relative piston position.

mm. The powder was separated from the graphite punches with a graphite foil in order to prevent material reactions with the die and to ensure an electric contact.

To obtain comparable processes, the overall process time for each sample was kept constant. An exemplary sintering process is shown in Fig. 4.1. A priori four different main phases during the sintering can be distinguished. In Fig. 4.1 these different phases are numbered and separated by dashed black lines.

During the first phase, a vacuum of around 1 mbar in the sintering chamber is built, the sample is prepressed to a defined pressure of 28 MPa and preheated to 420°C. It is worth to mention that the temperature was controlled by an optical pyrometer focused on a surface approximately 4 mm away from the sample in a hole drilled in the upper graphite punch. During the second phase, the actual heating procedure with a constant heating time of 5 min for all samples was applied. Additionally, during this phase the pressure was increased to 50 MPa. The example in Fig. 4.1 shows a process with a sintering temperature of 900°C. Series of samples with temperatures ranging from 450°C to 950°C with a step width of 50 K were sintered. The third phase is a constant holding time of the applied pressure and of the temperature at the defined sintering temperature. After the holding time, the pressure was released and the pulsed directed current was turned off. The samples cooled down for 30 min during the fourth phase.

Furthermore, Fig. 4.1 shows a blue dashed line corresponding to the relative piston position. The relative piston position can normally be interpreted as the state of densification. It is worth to mention that for the magnetite precursor the relative piston position could be interpreted that way. In the case of the hematite and iron precursor, the phase transformation to magnetite with only small changes in density could not lead to further conclusions of the densification state and the transition kinetics.

The post-sintered samples were cleared from the protective graphite foil. For the need of further investigations with scanning electron microscopy, high energy X-ray diffraction and Mößbauer spectroscopy, the samples were broken and prepared separately for each investigation method from the center part of the samples.

For the samples with the bigger initial particles sizes, only samples sintered at 600°C or higher are presented, since the densification for lower temperatures was not sufficient to obtain stable bulk materials.

4.2 Composites sintered from hematite and iron

4.2.1 Initial particle size $d = 190$ nm

For the hematite and iron precursor the same sintering process was used not only to densify but also to synthesise magnetite. For the first series from these precursors the mean particles size of hematite was 190(10) nm and for iron 220(60) nm. Exemplary images of the breaking edges of the post-sintered samples are shown in Fig. 4.2. Fig. C.1 in the appendix presents exemplary SEM images for all samples sintered from this precursor.

From the SEM images the mean values of the grain size can be determined. Fig. 4.3 shows the grain size in dependence of the sintering temperature. The grain growth can be described by an exponential function $d = (243.37 + 0.000397 \cdot \exp(T_{sinter}/81.43/K)) \cdot \text{nm}$.

The X-ray diffractograms of the series sintered from hematite and iron precursors are shown in the appendix Fig. C.2. In addition to the expected hematite, iron and magnetite phase additional wustite is present in the composites. The resulting volume fractions of magnetite, hematite, iron and wustite were derived by Rietveld refinement and are presented in Fig. 4.4. Decreasing amounts of iron and hematite are observed, while the volume fraction of magnetite increases. Additionally, the volume fraction of wustite is increasing and reaches a maximum when the iron phase is disappearing. For high sintering temperatures nearly pure magnetite is observed. The volume fraction of hematite and magnetite phase can be described by logistic functions.

The behaviour of magnetite can be described by $vf_M = (100 - 99.56/[1 + ([T_{sinter} - 273.15K]/677.73/K)^{7.79}]) \cdot \%$. The changes in the volume fraction of hematite can be

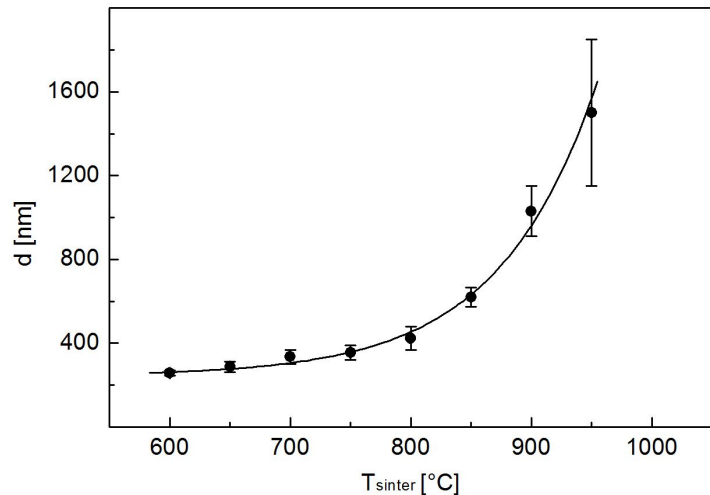


Figure 4.3: Mean grain size d in dependence of the sintering temperature T_{sinter} for the post-sintered samples from hematite and iron precursor powders.

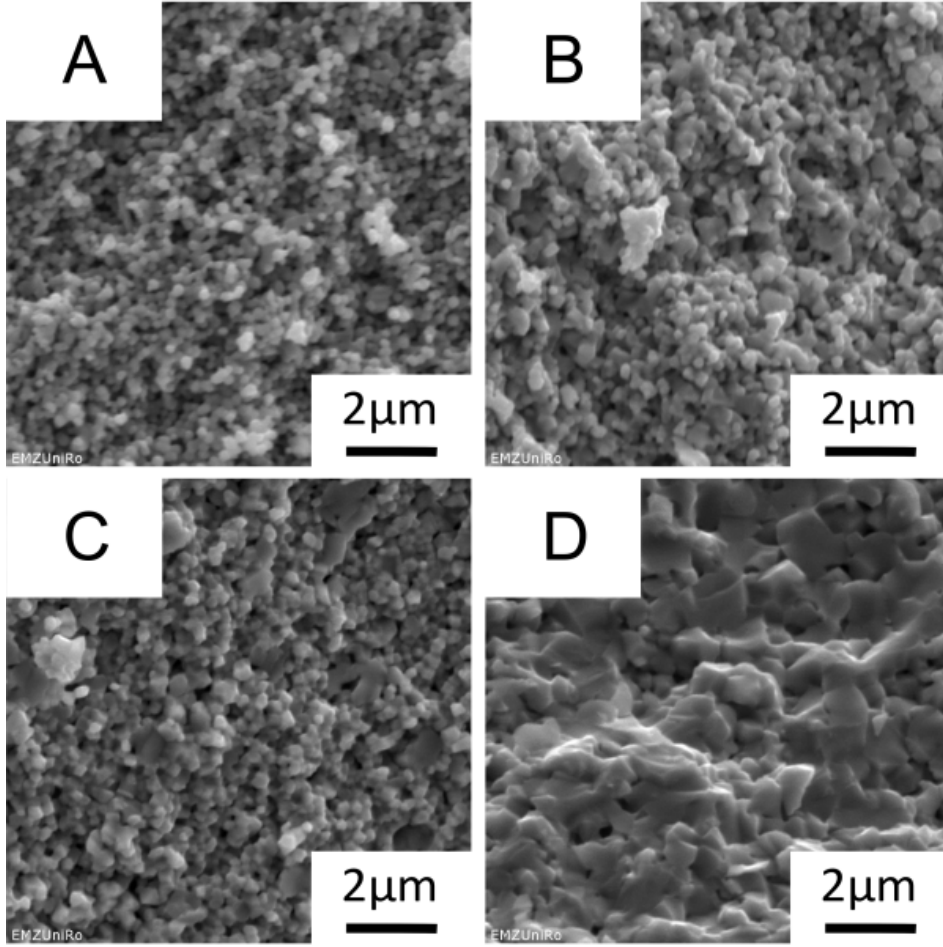


Figure 4.2: Exemplary SEM images of breaking edges of post-sintered composites from hematite and iron precursor powders sintered at A) 600°C, B) 700°C, C) 800°C and D) 900°C.

described by $vf_H = (139.96/[1 + ((T_{sinter} - 273.15K)/601.51/K)^{7.17}]) \cdot \%$. The iron present in the sample can be described by a hyperbola with $vf_I = (0.0221K/[T_{sinter} - 840.17K]) \cdot \%$ and wustite can be described by the formula $vf_W = (2.152 + 10.177 \cdot \exp(-(T_{sinter} - 1007.08K)^2/3510.87/K^2)) \cdot \%$.

The appearance of the additional amount of wustite in the composites leads to the conclusion that the assumed transition to magnetite of the stoichiometric mixture of hematite and iron does not take place in a single step but in a two step procedure with:



In the first step, hematite and iron react to magnetite and wustite and in the second step, hematite and wustite react to magnetite. Therefore, nearly pure magnetite is found for high sintering temperatures.

The crystal unit edge and the mean crystallite sizes derived by Rietveld refinement are shown in Fig. 4.5. The crystal unit edge shows a tendencies to decrease with

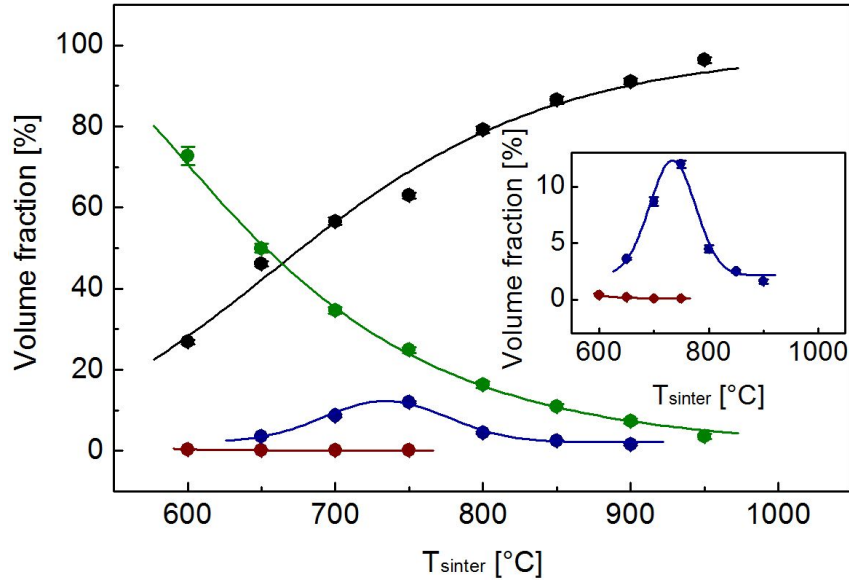


Figure 4.4: Volume fractions of the contributing phase, magnetite (black), hematite (green), iron (red) and wustite (blue) in dependence of the sintering temperature T_{sinter} for the post-sintered composites from hematite and iron precursor powders.

increasing sintering temperature which can be described by a linear function with $a = (8.41421 - 1.05 \cdot 10^{-5} \cdot T_{sinter}/K) \cdot \text{\AA}$. The crystallite size shows also an exponential grain growth which is described by $d_c = (87.94 + 0.00374 \cdot \exp(T_{sinter}/92.90/K)) \cdot \text{nm}$. The observed crystallite growth is in good agreement with the grain growth presented in Fig. 4.3, which leads to the assumption that the observed grains are single crystals.

The Mößbauer spectra of the post-sintered samples from hematite and iron precursor are shown in Fig. C.3 in the appendix. Additionally, the resulting relative intensities are shown in Fig. C.4 in the appendix as well. In the Mößbauer spectra, the additional wustite phase was also observed which had its maximum when the iron phase was disappearing from the post-sintered samples, supporting the assumption of a two-step transition from hematite and iron to magnetite. The resulting relative intensities are in good agreement with the volume fraction determined from high-energy X-ray diffraction studies.

Furthermore, the stoichiometry determined from the Mößbauer spectra utilising the relative intensities from magnetite A- and B-sites are presented by

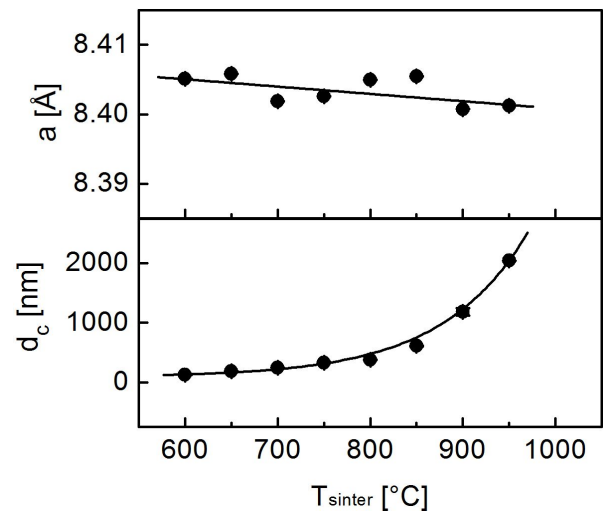


Figure 4.5: Crystal unit edge a and mean crystallite size d_c of magnetite phase in dependence of the sintering temperature T_{sinter} for the post-sintered composites from hematite and iron precursor powders.

the number of vacancies per formula unit in Fig. 4.6.

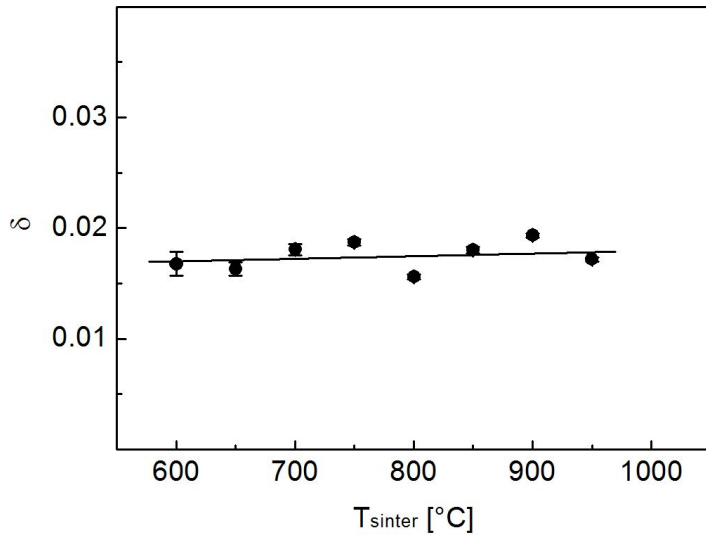


Figure 4.6: Number of vacancies per formula unit of the post-sintered composites in dependence of the sintering temperature T_{sinter} .

For small sintering temperatures the hyperfine interaction parameters differ from typical bulk values.

The changes in the magnetic hyperfine parameters are more pronounced for magnetite A- than for magnetite B-sites. This can have two different origins. It can be related to grain size effects which should only to be seen for the smallest grains in the series. Furthermore, the observed changes in the hyperfine interaction parameters can be related to interaction effects between ferrimagnetic and antiferromagnetic phases.

Nevertheless, the most probable reason for the observed changes in the hyperfine interaction parameters is an artefact of the fitting procedure. For a further discussion of these possibilities, it is necessary to obtain samples with smaller grains and with comparable compositions to rule out artifacts from the fitting procedure.

The changes in the hyperfine parameters for magnetite A- and B-sites can be described by linear and exponential functions. The changes in the mean isomer shift for magnetite A-sites can be described by $IS_A = (0.26029 - 5.316 \cdot 10^4 \cdot \exp(-T_{sinter}/62.84/K)) \cdot \text{mm/s}$. The changes in the mean value of the isomer shift for magnetite B-sites can be described by a linear function with $IS_B = (0.64649 + 1.501 \cdot 10^{-5} \cdot T_{sinter}/K) \cdot \text{mm/s}$.

The mean magnetic hyperfine field can in both cases be described by exponential functions with $\mu_0 H_{hfA} = (48.763 + 3.0986 \cdot 10^4 \cdot \exp(-T_{sinter}/75.64/K)) \cdot \text{T}$ and $\mu_0 H_{hfB} = (45.735 - 1.0378 \cdot 10^3 \cdot \exp(-T_{sinter}/89.28/K)) \cdot \text{T}$ for magnetite A- and B-sites, respectively.

The mean quadrupole splitting for magnetite A-sites can be described by $QS_A = (-0.0170 - 3.9271 \cdot \exp(-T_{sinter}/209.55/K)) \cdot \text{mm/s}$. The mean quadrupole splitting for magnetite B-sites is constant and only shows a tendency to decrease which can be presented by a linear function with $QS_B = (0.00298 - 3.6 \cdot 10^{-6} \cdot T_{sinter}/K) \cdot \text{mm/s}$.

Furthermore, Fig. 4.8 shows exemplarily the maps of the probability density distribu-

It is seen that the number of vacancies per formula unit is very small. This means that the synthesised magnetite is nearly stoichiometric. The number of vacancies per formula unit magnetite can be described by a linear function with $\delta = 0.01495 + 2.349 \cdot 10^{-6} \cdot T_{sinter}/K$. The number of vacancies per formula unit only show a small tendency to increase with the increasing sintering temperature.

The determined hyperfine interaction parameters for magnetite A- and B-sites are shown in Fig. 4.7. It is seen that for

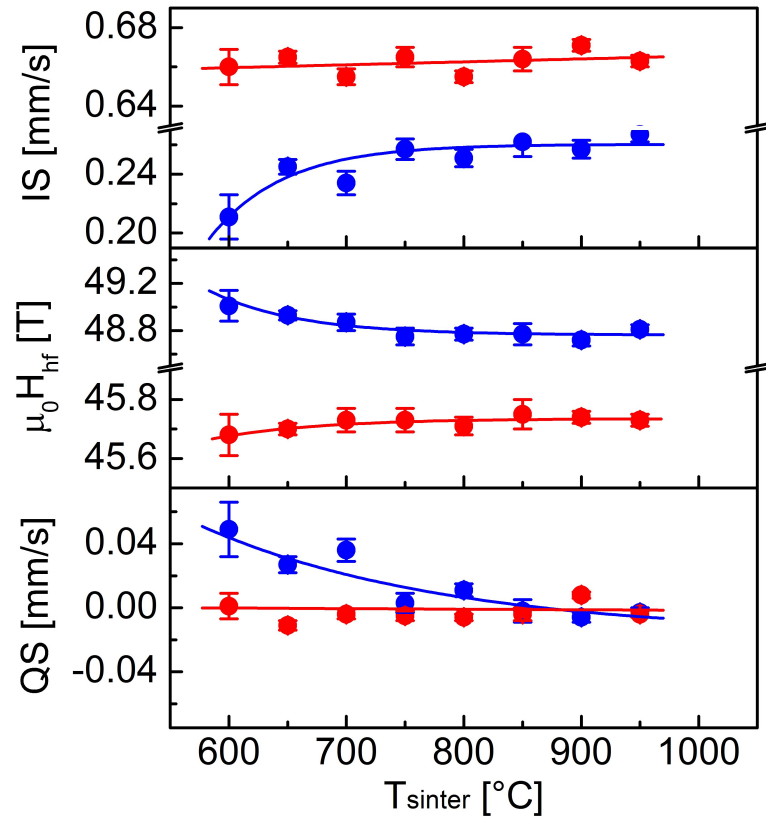


Figure 4.7: Calculated mean values of the hyperfine parameters in dependence of the sintering temperature T_{sinter} for the post-sintered composites from hematite and iron precursor powders. IS - isomer shift, $\mu_0 H_{hf}$ - magnetic hyperfine field and QS - quadrupole splitting. Hyperfine parameters for magnetite A-sites are presented in blue and magnetite B-sites in red.

tions of the hyperfine interaction parameters for the post-sintered composite sintered at 750°C. The probability density distributions do not show any significant changes with changing sintering temperatures.

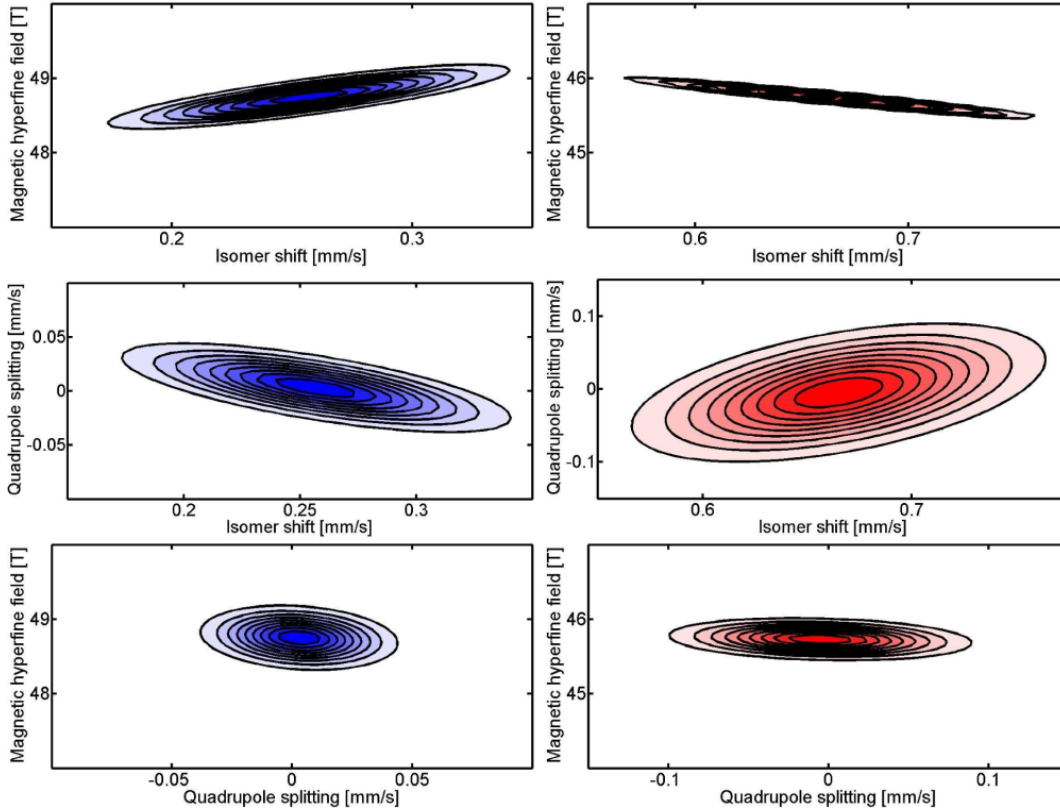


Figure 4.8: Maps of the probability density distributions as 2D projections of isomer shift and magnetic hyperfine field (top), isomer shift and quadrupole splitting (middle) and quadrupole splitting and magnetic hyperfine field (bottom) for the post-sintered sample from hematite and iron precursor sintered at 750°C. Left column: magnetite A-sites, right column: magnetite B-sites.

4.2.2 Initial particle size $d = 26$ nm

The series of post-sintered composites was sintered from a stoichiometric mixture of hematite and iron precursor powders with a mean particles size of 26 nm in the temperature range from 450°C to 950°C. Exemplary SEM images of the post-sintered samples are shown in the appendix Fig. C.5.

Compared to the first series sintered from hematite and iron precursors, the grain sizes of this grains are comparable. The direct dependence of the grain size in dependence of the sintering temperature is shown in Fig. 4.9.

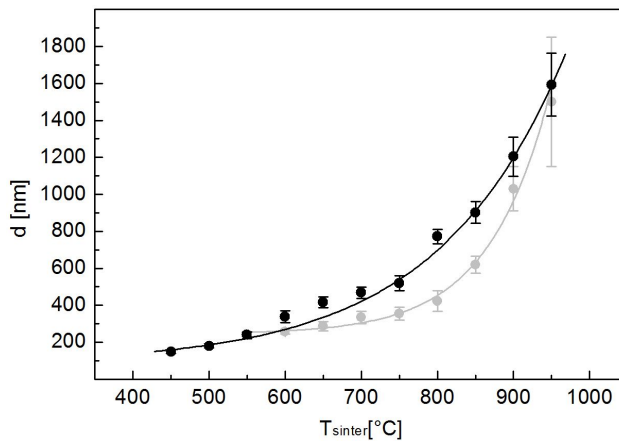


Figure 4.9: Mean grain size d in dependence of the sintering temperature T_{sinter} for the post-sintered composites for both hematite and iron precursor powders. Black - $d_i = 26$ nm and grey - $d_i = 190$ nm.

Additionally, the mean values of the grain size from the other hematite and iron precursor is shown in Fig. 4.9.

The mean grain size is comparable to the mean grain size of the previously presented series. Rather bigger grains are observed than in the series sintered from hematite and iron precursor with a mean particles size of 190 nm. The increase in the grain size can be described by the formula $d = (83.42 + 1.0026 \cdot \exp(T_{sinter}/167.22/K)) \cdot \text{nm}$.

The mean grain size of the samples shows a comparable behaviour to the former series. Due to this, no significant changes in the hyperfine interaction parameters are expected and the results for this series are shown in the appendix.

4.3 Composites sintered from magnetite

4.3.1 Initial particle size $d = 120 \text{ nm}$

The post-sintered samples were first investigated with the scanning electron microscope. Exemplary images from the breaking edges are shown in Fig. D.1 in the appendix. An increase in the mean grain size is observed.

From the SEM images the mean grain sizes of the particles were determined and are shown in Fig. 4.10. The grain size increases exponentially with increasing sintering temperature. This behaviour can be described with the formula $d = (180 + 0.035 \cdot \exp(T_{sinter}/128.7/K)) \cdot \text{nm}$.

It is worth to mention, that with this description the initial particle size of 120 nm was not reproduced in the frame of the error.

The high energy X-ray diffraction patterns of the post-sintered samples of this series are shown in Fig. D.2. The volume fractions of hematite and magnetite were calculated by Rietveld refinement procedure and are presented in Fig. 4.11. During the sintering process magnetite has partially decomposed to hematite.

It is worth to point out that the volume fraction of magnetite slightly increasing with an increasing sintering temperature, while hematite is consequently decreasing. The increase of the volume fraction of magnetite can be described by a linear function $vf_M = (41.7 + 0.027 \cdot T_{sinter}/K) \%$ and, thus, the volume fraction of hematite by the linear function $vf_H = (58.3 - 0.027 \cdot T_{sinter}/K) \%$.

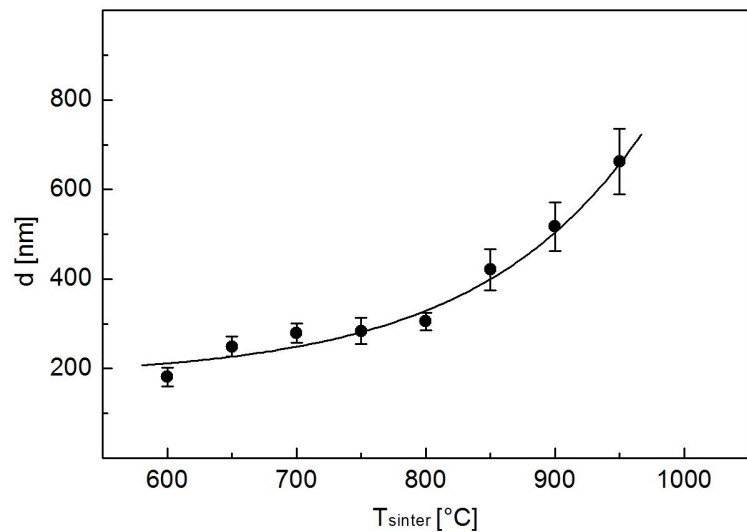


Figure 4.10: Mean grain size d in dependence of the sintering temperature T_{sinter} for the post-sintered composites from magnetite precursor powder.

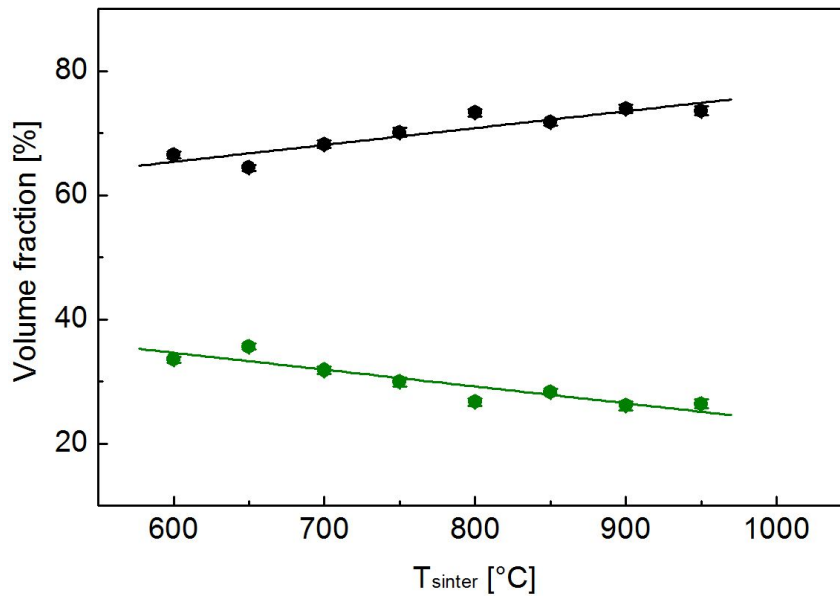


Figure 4.11: Volume fractions of the contributing phase, magnetite (black) and hematite (green) in dependence of the sintering temperature T_{sinter} for the post-sintered composites from magnetite precursor powder.

Furthermore, the refinement procedures lead to the possibility to calculate the crystal unit edges and the mean crystallite size of the nanostructured iron oxide composites. The results of these calculations are presented in Fig. 4.12.

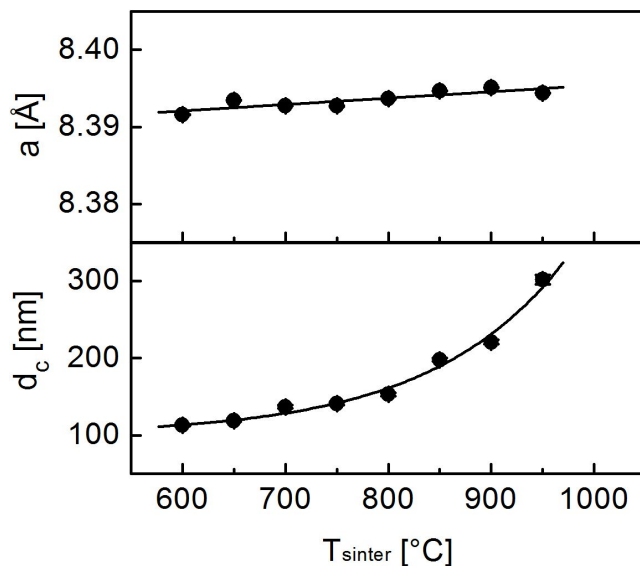


Figure 4.12: Crystal unit edge a and mean crystallite size d_c of magnetite phase in dependence of the sintering temperature T_{sinter} for the post-sintered composites from magnetite precursor powders.

The crystal unit edge of magnetite is mainly constant and only shows a tendency to increase with increasing sintering temperature. The behaviour can be described by the linear function $a = (8.38486 + 8.26 \cdot 10^{-6} \cdot T_{sinter}/K) \cdot \text{Å}$. For the mean crystallite size, the same behaviour as for the mean grain size can be observed. The mean crystallite size increases exponentially with the sintering temperature. It can be described by the formula $d_c = (100 + 0.0167 \cdot \exp(T_{sinter}/130.9/K)) \cdot \text{nm}$. It is worth to point out, that the determined crystallite size is approximately the half of the mean grain size for all composites in this series. This leads to the conclusion that several crystallites built a single grain.

The Mößbauer spectra of the sintered samples are shown in Fig. D.3 in the appendix. All spectra consist of three contributing

subspectra - magnetite A-sites, magnetite B-sites and hematite. The partial decomposition of the magnetite to hematite was also observed in the Mößbauer spectra, the calculated relative intensities of magnetite and hematite phases are presented in Fig. D.4, also in the appendix. The calculated relative intensities from the Mößbauer spectra are in good agreement with the calculated volume fractions from the Rietveld refinement procedures. The magnetite phase has a small tendency to increase with increasing sintering temperature, while the hematite phase is decreasing.

From the relative intensities furthermore the stoichiometry in form of the number of vacancies per formula unit δ can be determined, see Eq. (3.2). The numbers of vacancies per formula unit for the post-sintered composites in dependence of the sintering temperature are presented in Fig. 4.13.

The number of vacancies per formula unit in the sintered series are in the order of 0.025. The initial powder used for the synthesis had 0.125 as the number of vacancies per formula unit. The change in the oxidation state and with this the change in the number of vacancies can be explained by the decomposition of the material into magnetite with nearly no vacancies and into hematite. Considering Eq. (3.1), the number of vacancies per formula unit can be recalculated into a fraction of maghemite in the structure. Using this approach the fraction of maghemite should be 34.9(1.5)%.

The nonstoichiometric magnetite decomposed during the sintering into circa 30% hematite and 70% nearly stoichiometric magnetite, where the stoichiometry, the number of vacancies per formula unit, can be described by the formula $\delta = 0.0484 - 1.84 \cdot 10^{-5} \cdot T_{sinter}/K$.

The determined hyperfine parameters for the post-sintered series are shown in Fig. 4.14. The mean values of the hyperfine parameters do not show significant changes in dependence of the sintering temperatures for magnetite A- and B-sites. All mean values of the hyperfine parameters can be described by constants or linear functions. A constant was assumed, when the slope of the linear function was more than four orders of magnitude smaller than the intercept. The isomer shift of magnetite A- and B-sites can be described by constants with $IS_A = 0.2586\text{mm/s}$ and $IS_B = 0.669\text{mm/s}$, respectively. The magnetic hyperfine fields of magnetite A- and B-sites can be as well described by constants $\mu_0 H_{hfA} = 48.79\text{T}$ and $\mu_0 H_{hfB} = 45.69\text{T}$, respectively. The quadrupole splitting of magnetite A- and B-sites can be described by linear functions

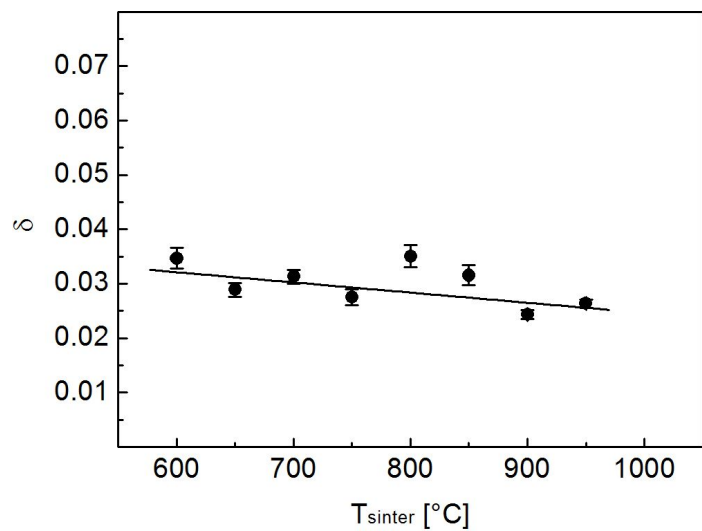


Figure 4.13: Number of vacancies per formula unit of the post-sintered composites in dependence of the sintering temperature T_{sinter} .

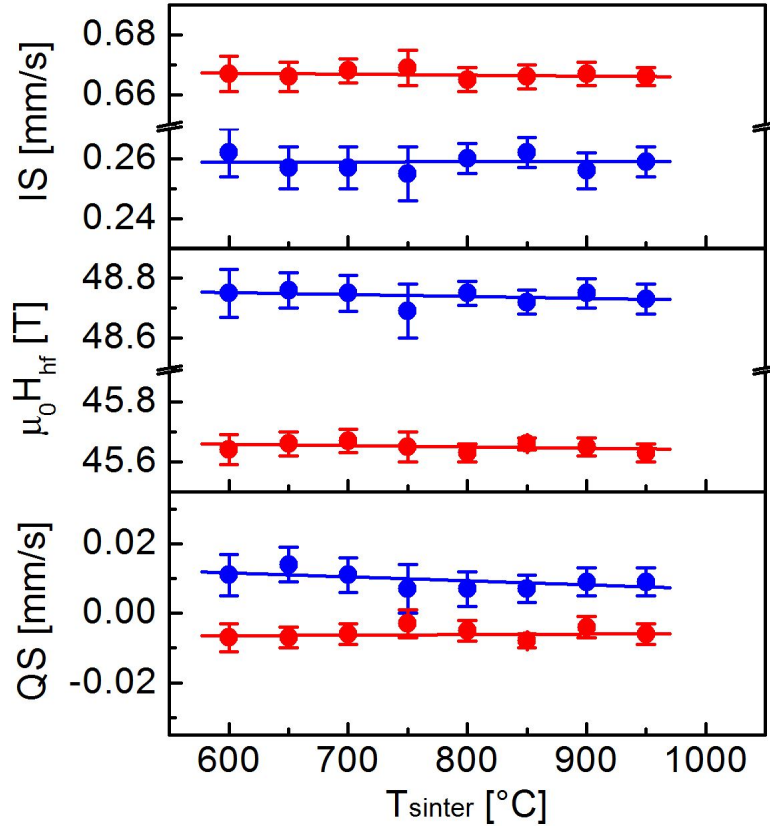


Figure 4.14: Calculated mean values of the hyperfine parameters in dependence of the sintering temperature T_{sinter} for the post-sintered samples from magnetite precursor powders. IS - isomer shift, $\mu_0 H_{hf}$ - magnetic hyperfine field and QS - quadrupole splitting. Hyperfine parameters for magnetite A-sites are presented in blue and magnetite B-sites in red.

with $QS_A = (0.0218 - 1.16 \cdot 10^{-5} \cdot T_{\text{sinter}}/K) \cdot \text{mm/s}$ and $QS_B = (-0.0070 - 0.16 \cdot 10^{-5} \cdot T_{\text{sinter}}/K) \cdot \text{mm/s}$, respectively.

Not only the hyperfine parameters, but also the distributions and the correlations between the hyperfine parameters were constant for all samples sintered from this magnetite precursor and independent of the sintering temperature. Exemplary maps of the probability density distribution functions of the hyperfine parameters are shown in Fig. 4.15 for the sample sintered at 700°C.

The variance of all hyperfine parameters is small. Only the isomer shift of magnetite B-sites shows a broader distribution of the magnetic hyperfine field, which is probably related to the present Fe^{3+} and Fe^{2+} ions present on this sites as described for the bulk reference sample.

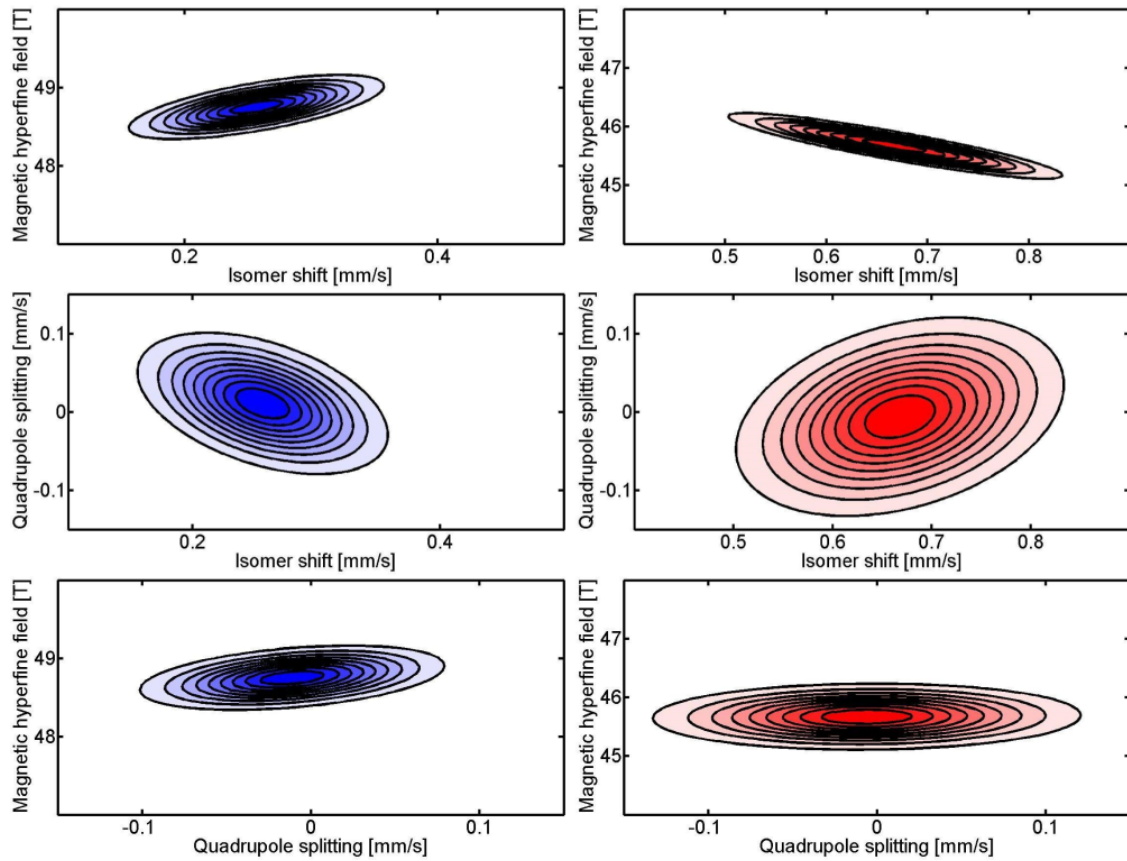


Figure 4.15: Maps of the probability density distributions as 2D projections of isomer shift and magnetic hyperfine field (top), isomer shift and quadrupole splitting (middle) and quadrupole splitting and magnetic hyperfine field (bottom) for the post-sintered composite from magnetite precursor sintered at 700°C. Left column: magnetite A-sites, right column: magnetite B-sites.

4.3.2 Initial particle size $d = 27$ nm

This series of composites was sintered from magnetite precursor with a mean particles size of 27(2) nm in the temperature range from 450°C to 950°C. Exemplary SEM images of the post-sintered samples are shown in the appendix Fig. D.5. Compared to the first series sintered from magnetite precursor, the grain sizes of this grains are smaller. The direct dependence of the grain size from the sintering temperature is shown in Fig. 4.16. Additionally, the mean values of the grain size from the other magnetite precursor are shown.

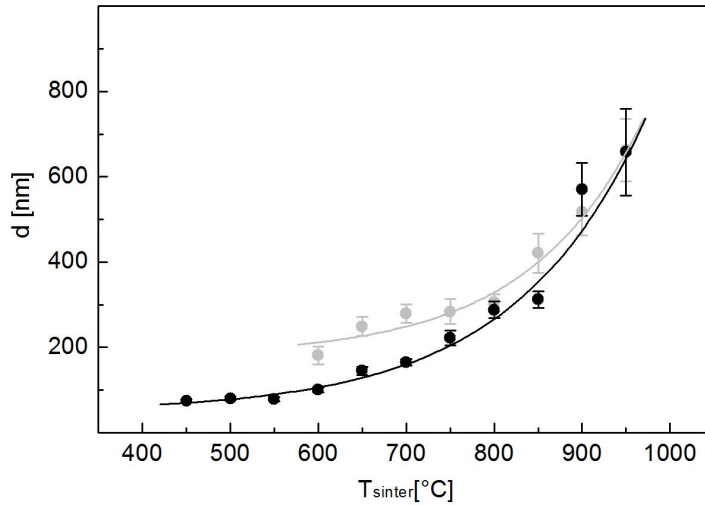


Figure 4.16: Mean grain size d in dependence of the sintering temperature T_{sinter} for the post-sintered samples from both magnetite precursor powders. Black - $d_i = 27$ nm and grey - $d_i = 120$ nm.

An exponential grain growth

with increasing sintering temperature was observed. For sintering temperatures below 850°C, the mean grain size of the series sintered from magnetite with $d_i = 27$ nm is smaller than the mean grain size of the post-sintered composites from the series sintered from magnetite with $d_i = 120$ nm. The grain size in dependence of the sintering temperature can be described by the function $d = (49.0 + 0.161 \cdot \exp(T_{sinter}/148.9/K)) \cdot nm$. Further studies of the sintered series with X-ray diffraction revealed that the main phase in the sintered composites is α -Fe₂O₃, hematite. The X-ray diffractograms are shown in the appendix Fig. D.6. The resulting volume fractions of magnetite and hematite were derived by Rietveld refinement and are presented in Fig. 4.17.

Assuming a solid solution of magnetite and maghemite in the nonstoichiometric precursor magnetite, the amount of maghemite in the powder was 57.7(2.0)%. In this series the present amount of hematite in the post-sintered composites is slightly higher than the calculated amount of maghemite in the precursor powders. Nevertheless, the assumption of the instability of the γ -Fe₂O₃ is supported. The amount of magnetite and hematite in the post-sintered samples can be described by linear functions with $vf_M = (26.20 + 0.0064 \cdot T_{sinter}/K)\%$ and $vf_H = (73.80 - 0.0064 \cdot T_{sinter}/K)\%$, respectively.

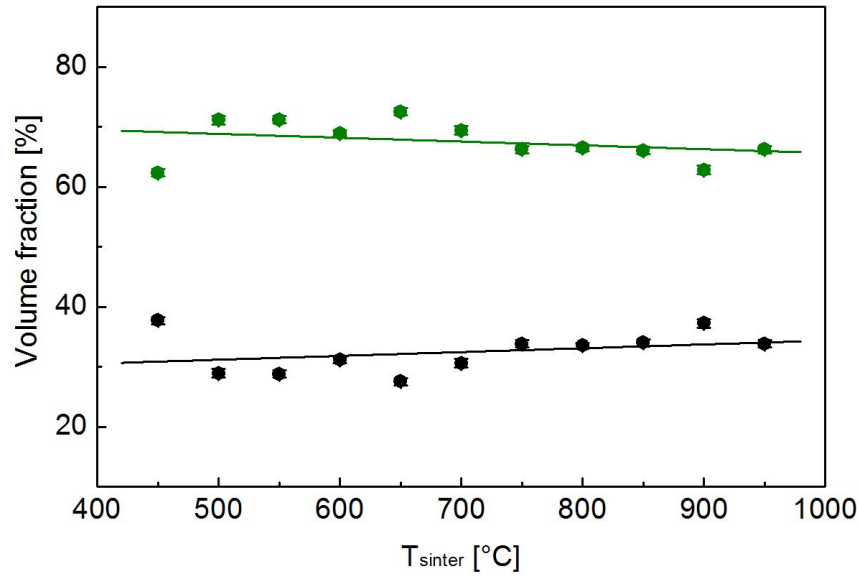


Figure 4.17: Volume fractions of the contributing phase, magnetite (black) and hematite (green) in dependence of the sintering temperature T_{sinter} for the post-sintered composites from magnetite precursor powders.

Furthermore, the calculated crystal unit edge a and the mean crystallite size d_c of the sintered series from magnetite precursors are shown in Fig. 4.18. Additionally presented in Fig. 4.18 are the results from the previously shown series. The crystal unit edge shows small tendencies to change, which can be described as a parabola with $a = (8.36495 + 1.711 \cdot 10^{-4} \cdot T_{sinter}/K - 1.875 \cdot 10^{-7} \cdot T_{sinter}^2/K^2) \cdot \text{Å}$.

The crystallite size shows an exponential growth with increasing sintering temperature, which is comparable to the grain growth of this series. The crystallite size can be described by the function $d_c = (50.06 + 0.00053 \cdot \exp(T_{sinter}/89.70/K)) \cdot \text{nm}$. This behaviour leads to the conclusion, that the observed grains in the

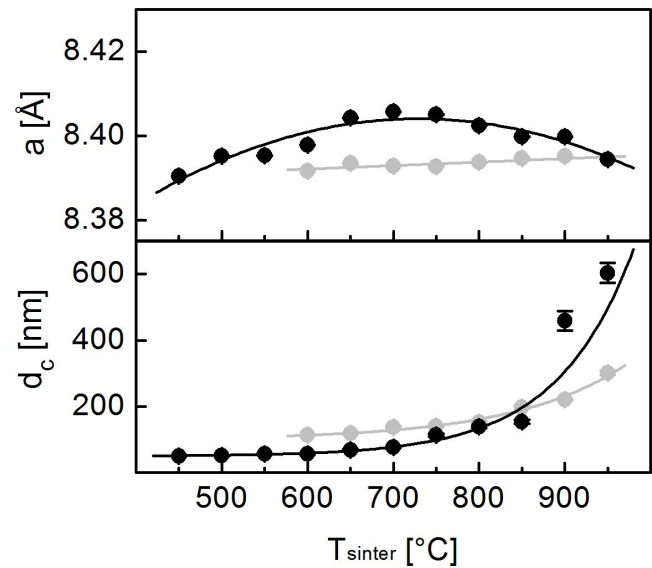


Figure 4.18: Crystal unit edge a and mean crystallite size d_c of magnetite phase in dependence of the sintering temperature T_{sinter} for the post-sintered composites from magnetite precursor powders. Black - $d_i = 27$ nm and grey - $d_i = 120$ nm.

SEM studies are mainly monocrystallites. For small sintering temperatures the crystallite sizes as well as the grain sizes are smaller than the ones sintered from the magnetite precursor with $d_i = 120$ nm, but for high sintering temperature, the grain growth as well as the crystallite growth is stronger in this series.

Fig. D.7 in the appendix shows the taken Mößbauer spectra, as well as the calculated spectra and the corresponding subspectra of each composite sintered in the series from magnetite precursor with an initial particle size of $d_i = 27$ nm.

The dominating spectra in this series corresponds to the hematite phase. Therefore, the calculated spectra for magnetite are influenced by the overlap to the spectra of the hematite phase. Nevertheless, the tendencies which is observed in this series can still be discussed not as an artefact of the fitting procedure but as an effect due to the reduction of the mean grain and crystallite size. The derived relative intensities of the two present phases, magnetite and hematite, are presented in Fig. D.8 in the appendix. It is worth to point out that also here the derived relative intensities are in good agreement with the derived volume fractions from the high energy X-ray diffraction studies.

Furthermore, the determined stoichiometry in form of the number of vacancies per formula unit of magnetite are presented in Fig. 4.19. A strong decrease of the number of vacancies per formula unit can be observed with an increasing sintering temperature. The behaviour can be described by an exponential function $\delta = 0.027 + 20.649 \cdot \exp(-T_{sinter}/140.29/K)$.

The calculated mean values of the hyperfine interaction parameters are presented in Fig. 4.20. In comparison to the series sintered from magnetite powder with $d_i = 120$ nm, the mean values of the hyperfine interaction parameters show significant changes. Especially, the magnetic hyperfine field shows an increase with increasing sintering temperature. It is worth to notice that the isomer shift as well as the magnetic hyperfine field show changes in dependence of the sintering temperatures, while the quadrupole splitting stays constant and only tendencies to de- or increase for magnetite A- and B-sites are seen.

The mean values of the isomer shift can be described by linear functions in dependence of the sintering temperatures with $IS_A = (0.2843 - 5.434 \cdot 10^{-5} \cdot T_{sinter}/K) \cdot \text{mm/s}$ and $IS_B = (0.60376 + 4.4434 \cdot 10^{-5} \cdot T_{sinter}/K) \cdot \text{mm/s}$, for magnetite A- and B-sites respectively.

The mean value of the magnetic hyperfine field can be described by exponential functions for magnetite A- and B-sites: $\mu_0 H_{hfA} = (49.492 - 14.45 \cdot \exp(-T_{sinter}/274.08/K)) \cdot \text{T}$ and $\mu_0 H_{hfB} = (45.805 - 708.46 \cdot \exp(-T_{sinter}/105.13/K)) \cdot \text{T}$, respectively.

The mean values of the quadrupole splitting show only tendencies to de- or increase, which can be described by linear functions. The behaviour of magnetite A-sites can

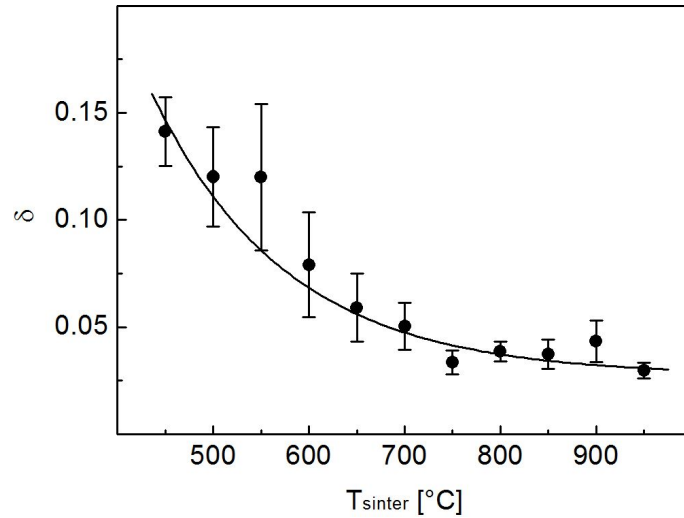


Figure 4.19: Number of vacancies per formula unit of the post-sintered samples in dependence of the sintering temperature T_{sinter} .

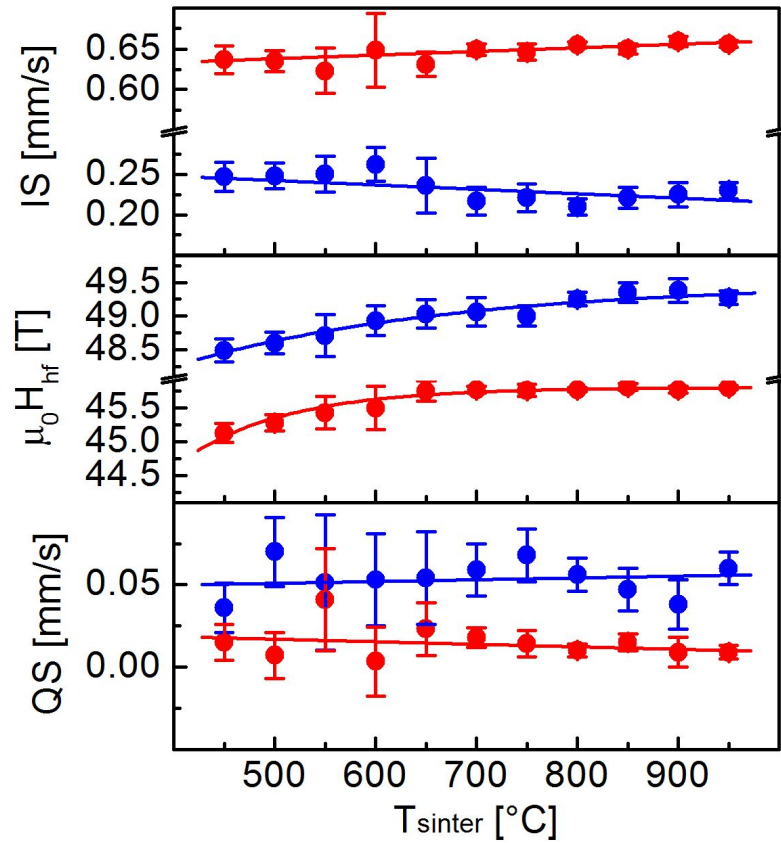


Figure 4.20: Calculated mean values of the hyperfine parameters in dependence of the sintering temperature T_{sinter} for the post-sintered composites from magnetite precursor powders. IS - isomer shift, $\mu_0 H_{hf}$ - magnetic hyperfine field and QS - quadrupole splitting. Hyperfine parameters for magnetite A-sites are presented in blue and magnetite B-sites in red.

be described by $QS_A = (0.0424 + 1.09204 \cdot 10^{-5} \cdot T_{sinter}/K) \cdot \text{mm/s}$ and the behaviour of magnetite B-sites can be described by $QS_B = (0.0288 - 1.5333 \cdot 10^{-5} \cdot T_{sinter}/[^\circ\text{C}]) \cdot \text{mm/s}$.

The observed changes in the hyperfine interaction parameters can have several origins. It is possible that the modifications in the hyperfine parameters are related to the changes in the stoichiometry of the samples with increasing sintering temperature or that they are a result of the small grain and crystallite sizes of the investigated composites.

Also the maps of the probability density distributions of all hyperfine interaction parameters show significant changes for small sintering temperatures. Fig. 4.21 and Fig. 4.22 present the probability density distributions of the hyperfine parameters of magnetite A- and B-sites, respectively. For small sintering temperatures, a broadening of the distributions of the hyperfine parameters can be observed. The broadening of magnetite A-sites is more pronounced which is related to the overlap of the Mößbauer spectrum from this sites with the spectrum from hematite. Nevertheless, the tendencies of additional broadening for small sintering temperatures up to around 600°C can be observed.

For magnetite A-sites, a strong correlation between all hyperfine interaction parameters can be seen in Fig. 4.21. For the isomer shifts and the magnetic hyperfine fields as well as the quadrupole splittings and the magnetic hyperfine fields, the correlations are strong and they are also observed for higher sintering temperatures, while for the isomer shifts and the quadrupole splittings the correlations between these two parameters are vanishing for higher sintering temperatures. The correlations between the hyperfine parameters of magnetite B-sites which are presented in Fig. 4.22, are comparable to the correlations of magnetite A-sites for high sintering temperatures. For lower sintering temperatures, the correlations between the isomer shifts and the quadrupole splittings are weak, however rising with increasing sintering temperatures.

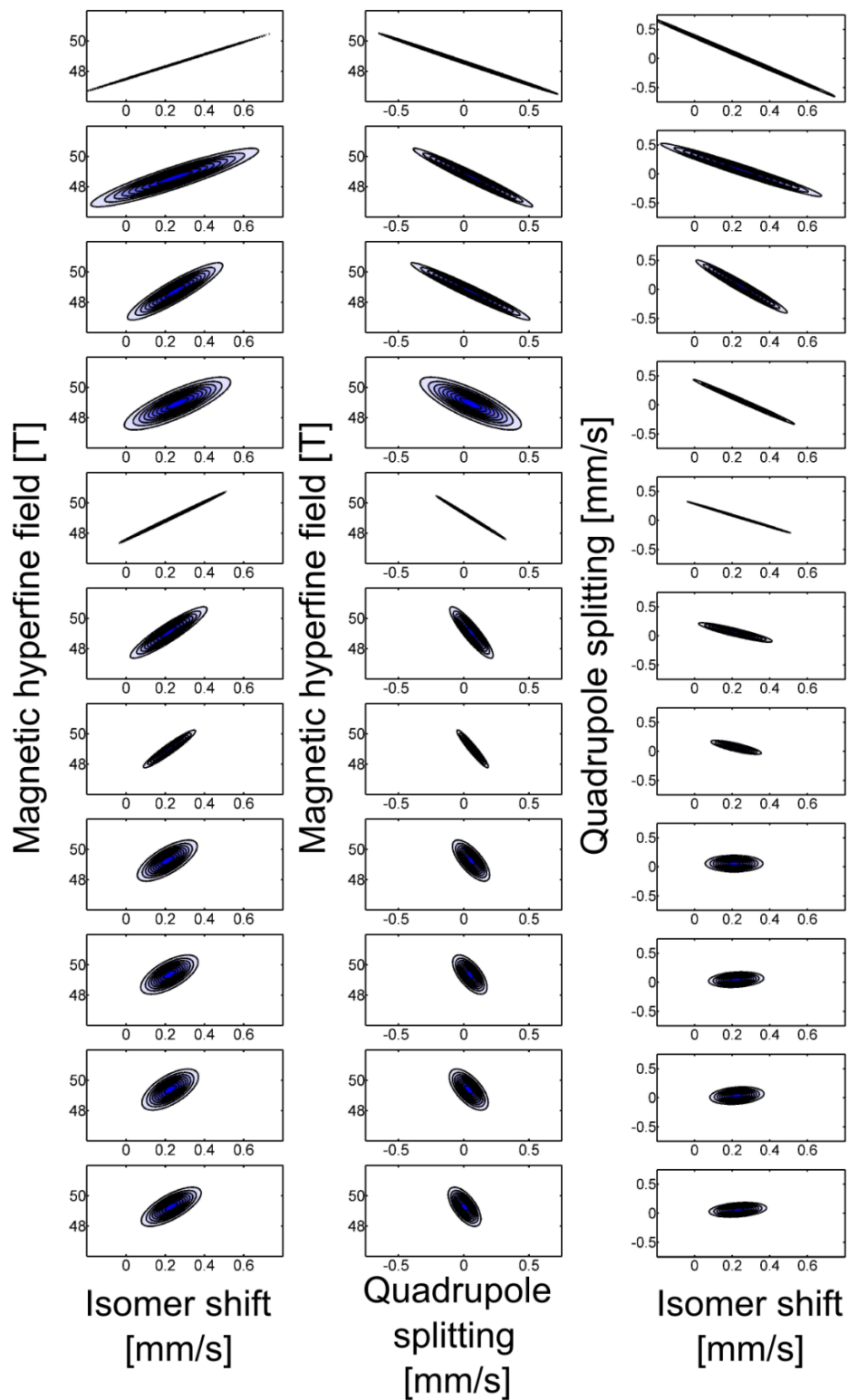


Figure 4.21: Maps of the probability density distributions as 2D projections of isomer shift and magnetic hyperfine field (left) and quadrupole splitting and magnetic hyperfine field (middle) isomer shift and quadrupole splitting (right) for magnetite A-sites. From the top to the bottom with increasing sintering temperature.

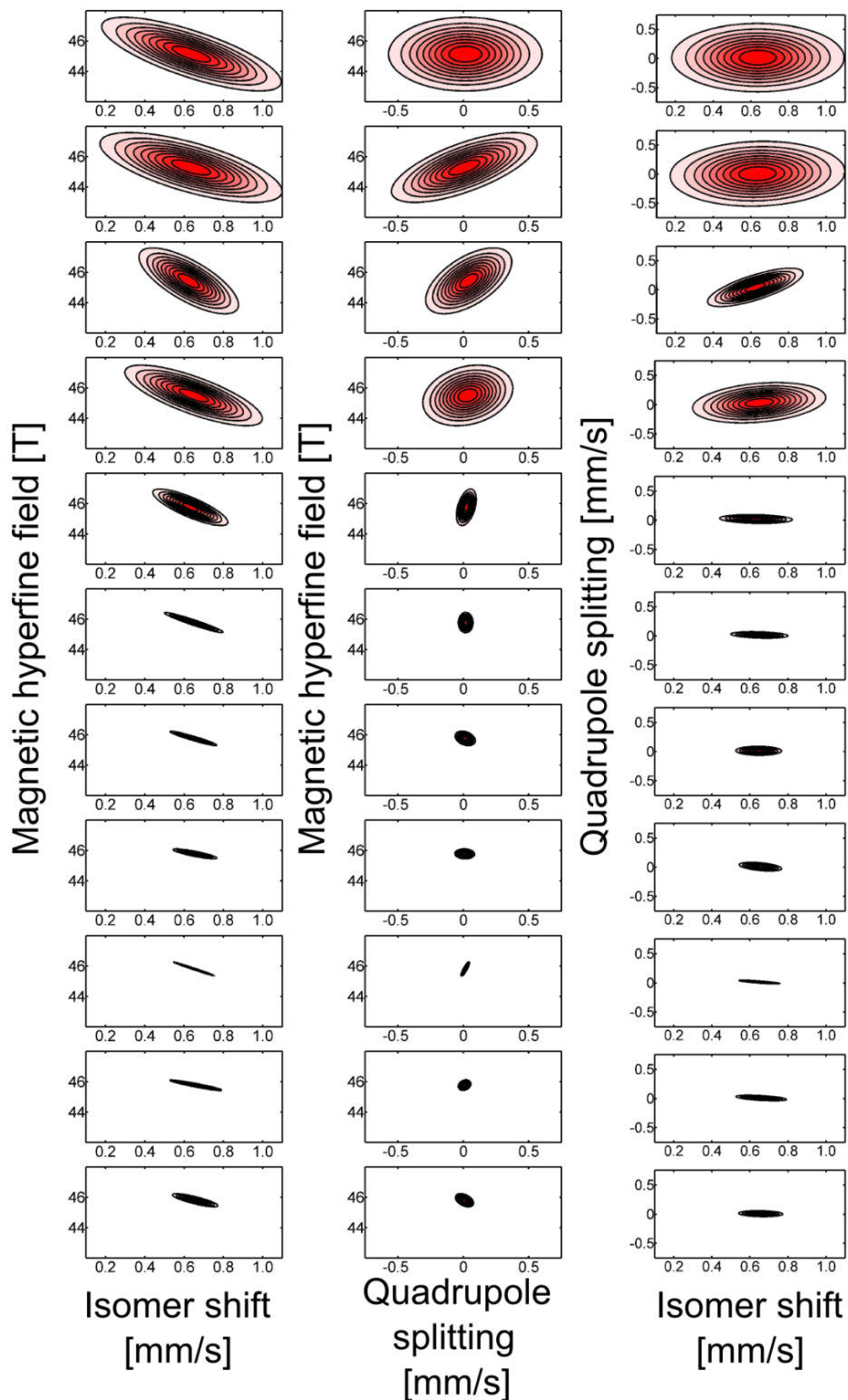


Figure 4.22: Maps of the probability density distributions as 2D projections of isomer shift and magnetic hyperfine field (left) and quadrupole splitting and magnetic hyperfine field (middle) isomer shift and quadrupole splitting (right) for magnetite B-sites. From the top to the bottom with increasing sintering temperature.

Chapter 5

Discussion

The presented work is separated into two main parts. The first part contains the interpretation of Mößbauer spectra in the case of nanostructured materials with a focus on nanoparticles introducing a possible fitting model for nanostructured bulk materials. The second part deals with the synthesis and the characterisation of nanostructured composites with the aim to demonstrate modifications of the hyperfine interaction parameters by the refinement of grain structure of bulk materials to the nanoscale through the treatment of the materials with field assisted sintering.

Interpretation of the Mößbauer spectra. The interpretation of Mößbauer spectra of nanostructured materials is demanding. This is related to the fact that not only structural models but also fitting models need several assumptions and simplifications. These are necessary in order to ensure reliable and reproducible fitting procedures. The chosen laboratory system to investigate the influence of the nanostructure refinement on the hyperfine interaction parameters was magnetite.

Magnetite is ferrimagnetic and it is characteristic of a large single domain size in the regime of 75 nm to 80 nm [7]. Due to this fact interaction as well as grain size effects are seen on longer length scales. The structure of magnetite is cubic with two different positions that iron ions are occupying [18] leading to two sextets in a Mößbauer spectrum at room temperature. The spectra were analysed assuming the pair-localised electron hopping process on the octahedral positions [67]. Due to this fact the fitting procedure of pure magnetite phase is simple compared to hard magnetic phases like $\text{Nd}_2\text{Fe}_{14}\text{B}$. The ^{57}Fe isotope is abundant in iron with an ideal half life of 98.1 ns [56]. This leads to small half widths in the Mößbauer spectra enabling the accurate determination of the hyperfine interaction parameters. Moreover, since most iron oxides are metastable, it is possible to transform iron oxides from antiferromagnetic phases to ferrimagnetic phases and vice versa [11]. Nevertheless, this metastability of iron oxides can also be interpreted as a disadvantage. Since magnetite tends to built vacancies on the octahedral positions, the stoichiometry of magnetite changes. This influences also the hyperfine interaction parameters [22] which further complicates it to resolve the influence of the nanostructure of grains on the hyperfine interaction parameters of bulk materials.

Nevertheless, due to the biocompatibility of magnetite as well as maghemite, these materials offer lots of potential applications in biomedicine [2, 3, 91, 92]. Therefore, a great variety of different synthesis methods have been developed [91, 93–95] and magnetite and maghemite were investigated to a great extend by Mößbauer spectroscopy [22, 23, 75, 76, 80, 87, 88, 90, 96–100].

For the interpretation of the Mößbauer spectra, mainly two models are applied. In the first model, the spectra are only described by simple Lorentzian line shapes correspond-

ing to the introduced Lorentz model, see [82, 90, 101, 102] for example. In the second mainly used model, it is assumed that the particle sizes of the magnetic nanoparticles lead to a distribution of only the magnetic hyperfine field, which would correspond to the described simple Voigt model, see [88, 103–105] for example.

The Lorentz model assumes that a line broadening only appears due to the change of the transition probability between two magnetic easy directions in a nanoparticle resulting in a change of the isomer shift and the magnetic hyperfine field [74, 76]. Magnetic nanoparticles always show a particle size distribution, changing the transition probability between the two energetic easy magnetisation directions [76, 80]. This is furthermore taken into account by the simple Voigt model. Both models were tested on BNF nanoparticles with a mean crystallite size of 22.4(9) nm and a structure characteristic for magnetite with slightly reduced crystal unit edge which is characteristic for nonstoichiometric magnetite [22]. Applying the Lorentzian model led to a goodness of the fit of 9.01 and it was possible to reproduce all features of the spectrum. Applying the simple Voigt model with only one Gaussian distribution resulted in a goodness of the fit of 22.79. Furthermore, introducing more components to describe the magnetic hyperfine field distribution could only reduce the goodness of the fit to 13.51. Also the features of the spectrum could not be reproduced satisfactorily.

Both models basically omit the fact that the influence of the surface becomes more important. Applying Mößbauer spectroscopy, certain nuclei are excited directly leading to an overlap of different signals from different positions inside the particles. Due to this fact, the different local chemical and electronic environment of these nuclei and, thus, their different hyperfine interaction parameters have to be taken into account. Furthermore, the assumption of Lorentzian line shapes in the Mößbauer spectrum is only valid in a completely static case [77]. In the case of magnetic nanoparticles, the transition between the two energetic easy magnetisation directions is a time dependent effect which also influences the Hamiltonian containing the hyperfine interaction parameters, resulting in non-Lorentzian line shapes [77].

This is taken into account by the extended Voigt model. Applying the extended Voigt model, probability density distributions to describe the hyperfine interaction parameters with possible correlations between the three parameters are assumed. It is worth to point out that the direct origin of the distribution of the hyperfine interaction parameters can be a time dependent effect. This can be a result of the transitions between the two energetic easy magnetisation directions or also a result of the different electronic surroundings of the probed nuclei.

The first presented model of extended Voigt models assumed only distributions of isomer shift and the magnetic hyperfine field. This model is best comparable to the Lorentzian and the simple Voigt model. It was already discussed that the transition probability between the two energetic easy magnetisation directions leads on the one hand to a change in the isomer shift and on the other hand to a reduction of the magnetic hyperfine field. Taking into account the particle size distribution of the nanoparticles, or rather crystallites, the extended Voigt model with distributions of the isomer shift and the magnetic hyperfine field is reasonable. The application of this model led to a goodness of the fit of 8.03 and a strong correlation between the isomer shift and the

magnetic hyperfine field for magnetite A-sites but was not observed for magnetite B-sites. Compared to the Lorentz model, a smaller goodness of the fit was observed and also all features of the spectrum could be reproduced.

In the second model of extended Voigt models, it was assumed that the quadrupole splitting and the magnetic hyperfine field show a distribution. Magnetite is a cubic structure. Therefore, it normally does not show a quadrupole splitting. BNF particles are characteristic of a multicore structure with mainly one easy axis of magnetisation, leading to an effectively uniaxial anisotropy. Therefore, the electric field gradient of each crystallite has a random angle to the easy axis of magnetisation of the whole particle [81]. Taking into account the finite size of the nanoparticles, where symmetry breaking of the crystallites is possible close to the surface of the crystallites a quadrupole splitting should be present. Nevertheless, the distribution of the magnetic hyperfine field can still be described by time dependant fluctuations and particle size distributions. Following this approach the goodness of the fit was reduced to 7.86 and again a strong correlation between the two hyperfine parameters was observed for magnetite A-sites but not for magnetite B-sites. The features of the spectrum could be reproduced applying the extended Voigt model with distributions of the quadrupole splitting and the magnetic hyperfine field.

In the third model, basically all hyperfine parameters were assumed to show distributions and correlations between these parameters were allowed. Applying this model, the goodness of the fit was further reduced to 7.53 and all features of the spectrum could be reproduced. The correlation between the isomer shift and the magnetic hyperfine field, as well as, the correlation between the quadrupole splitting and the magnetic hyperfine field stayed comparable to the results of the previous two models. The correlation between the isomer shift and the quadrupole splitting was neglectable for magnetite A-sites but significant for magnetite B-sites. These results indicate that different effects are dominating at the different sites of magnetite. Magnetite B-sites are more affected by the surface to volume ratio of a crystallite. Therefore, they are also more affected by the induced lattice strain than the A-sites [82]. At magnetite B-sites, a pair-localised electron hopping is observed above the Verwey transition temperature. Here, intrinsic effects like lattice strains, stoichiometry, disorder, as well as surface effects appearing in nanoparticles, can be dominant. At the A-sites, including iron ions from magnetite B-sites excluded from the pair-localised hopping process, the behaviour can be dominated by whole-particle effects creating a possibility of observing changes in the hyperfine parameters due to a particle size distribution. Nevertheless this conclusion needs further investigation.

It is also worth to point out that the observed reduction of the goodness of the fit can always be an artefact of an over-parametrisation, especially, when no restrictions concerning the correlations between the hyperfine interaction parameters were taken into account. Since it is not possible to conclude about the over-parametrisation on a single particle system, a series prepared by co-precipitation route was investigated to observe changes in the hyperfine interaction parameters in dependence of the particle size.

Application of the extended Voigt model to nanoparticles. The synthesised nanoparticles did not only consist of magnetite. Also iron and goethite were present in the samples. The magnetite particles were monocrystals and the size of the crystals decreased with the increasing amount of Fe^{3+} ions used during the coprecipitation from 16.3(3) nm to 2.1(3) nm. A similar behaviour was reported in [85]. The Mößbauer spectra of the samples showed a transition from broad sextets to doublets. The two dominating sextets in the spectra were identified to belong to magnetite in the stable ferrimagnetic or in the so called blocked state. The doublet was identified to belong to magnetite in the superparamagnetic state. Furthermore, the presence of ferrihydrates cannot be excluded since the samples showed a poor crystallinity also as a result of their small sizes and due to the fact that the hyperfine interaction parameters of superparamagnetic magnetite and of ferrihydrates are comparable [16]. To describe the sextets as well as the doublets in each spectra the extended Voigt model with correlations between all hyperfine parameters was taken into account.

It was noticed that the mean isomer shift of magnetite A-sites increased while the isomer shift of magnetite B-sites decreased, for magnetite being in the blocked state. Here an increase of the number of vacancies and the decrease of the mean particle size can be the origin of this change [67, 90]. Furthermore, the mean value of the quadrupole splitting of both sites stayed approximately constant. The biggest changes were observed for the mean value of the magnetic hyperfine field. For both sites, a strong decrease of the mean value of the magnetic hyperfine field was observed. The derived values are smaller than the magnetic hyperfine field of large single crystalline magnetite [16]. The decreasing mean value of the magnetic hyperfine fields is originated by fast fluctuations of the magnetisation direction of the particles around the easy axis, where the angle between the easy axis and the magnetisation increases with decreasing particle sizes [76]. The mean value of the magnetic hyperfine field for magnetite B-sites decreased faster than the mean magnetic hyperfine field of magnetite A-sites. This is related to a strong electric field gradient as a result of the huge surface to volume ratio of the particles, which affects magnetite B-sites stronger than magnetite A-sites [82].

The probability density distributions of both sites of magnetite show significant changes with the transition from the blocked into the superparamagnetic state. The strongest changes are observed in the partially integrated probability distributions of the magnetic hyperfine fields. For magnetite A-sites, the isomer shift and the magnetic hyperfine field, the quadrupole splitting and the magnetic hyperfine field show only weak or no correlations over the whole series. Strong correlations were observed between the isomer shift and the quadrupole splitting. For magnetite B-sites, stronger correlations between the isomer shift and the magnetic hyperfine field, as well as, the quadrupole splitting and the magnetic hyperfine field were observed and only weak correlations are seen for the isomer shift and the quadrupole splitting. The observed correlations are different than in the BNF nanoparticles. Nevertheless, the observed correlations are reproducible over the whole series. They are contrary for magnetite A- and B-sites supporting the assumption of the different dominating effects on the two sites of magnetite. The observed differences in the correlations can be influenced by interparticle interactions due to the fact that the BNF nanoparticles possess a starch shell covering the crystallites

and separating the particles from one another. The coprecipitated series of nanoparticles was produced without any further protecting shell giving rise to further agglomeration of the particles.

The observed doublet in the spectra of the nanoparticles was interpreted to belong to the superparamagnetic state of magnetite. The Mößbauer spectrum of superparamagnetic magnetite consists of two overlapping doublets from magnetite A- and B-sites [82]. For an increasing Fe^{3+} ion concentration, meaning a decrease in the mean particle size, changes in the hyperfine parameters of the superparamagnetic doublets and their probability density distributions are observed. The mean value of the isomer shift showed a tendency to increase. The mean value of the quadrupole splitting showed more significant changes. Both need to be results of the small sizes of the particles but they can also be originated by modifications in the stoichiometry [82, 88].

Validation of the extended Voigt model. The presented probability density distributions of the hyperfine interaction parameters in the studied series of nanoparticles showed consistency. Nevertheless, the reduction of the particle size actually led to transitions from the blocked into the superparamagnetic states. Due to this fact, the fits for the Mößbauer spectra which were taken directly in the region of the transition are not reliable since the assumption of the effectively static Hamiltonian [77] is not valid. Nevertheless, the mean values of the hyperfine interaction parameters show the correct tendencies.

Furthermore, the reference material mainly consisting of magnetite with a mean crystallite size of 295(50) nm showed that for huge crystallite sizes the probability density distributions are diminishing. A slight distribution for the isomer shift for magnetite B-sites was observed, which can be a result of the two different oxidation states of the iron ions on the B-sites. The magnetic hyperfine field showed small deviations, which were stronger pronounced for the magnetite B-sites than for the A-sites. This can be a result of the nonstoichiometry in the sample with a number of vacancies per formula unit of $\delta = 0.036(1)$.

These two facts, the consistency in the correlation between the hyperfine parameters and the vanishing of the distributions for large crystals lead to the conclusion that an over-parametrisation was not the reason for a reduction of the goodness of the fit for the studied BNF particles. Two reasons are important to use the extended Voigt model to interpret the Mößbauer spectra of nanoparticles. The Hamiltonian containing the hyperfine interaction parameters of the excited nuclei is not static anymore. This leads to non-Lorentzian line shapes. Additionally, the reduction of the particle size results in a bigger surface to volume ratio, which leads to contributions in the Mößbauer spectrum from different local electronic environments and, therefore, to additional broadening of the lines.

In the case of nanostructured iron oxide composites, the basic line shapes should be Lorentzians, since the Hamiltonian is static. Nevertheless, the mean grain size is orders of magnitudes smaller than in conventionally prepared bulk materials. Due to this fact, the interface areas at the grain boundaries are also orders of magnitudes larger than in conventionally prepared bulk materials. The influence of the different positions in

the nanostructured material should lead to distributions of the hyperfine parameters, leading to Mößbauer lines with non-Lorentzian shapes in the spectrum. Therefore, an extended Voigt model with possible correlations between all hyperfine parameters was used to describe the Mößbauer spectra of the nanostructured iron oxide composites.

Iron oxides prepared by FAST. The densification of iron oxide under FAST conditions was already investigated by several researchers [10–14, 106]. It was shown that the sintering of γ -Fe₂O₃ under various temperatures leads to mixtures of cubic and hexagonal iron oxides with significantly changes of the saturation magnetisations and coercivities [10–13]. Nanostructured composites composed of soft magnetic Fe₃O₄ and hard magnetic CoFe₂O₄ showed significant changes in the hysteresis behaviour in dependence of the sintering temperature. Furthermore, it was also shown that FAST enables the synthesis of transparent magnetic bulk materials containing Fe₃O₄ nanoparticles [106].

The mentioned research mainly focussed on the change of the coercivity and the saturation magnetisation, as well as, the exchange field in dependence of the mean grain size. It was also pointed out that the observed changes in the behaviour of nanostructured hematite - maghemite composites have an increased area of interfaces between these two components. Therefore a material with exchange bias is built [10, 12].

Changes in the hysteresis behaviour of the magnets are a result of three main factors, the Curie temperature, the saturation magnetisation and the uniaxial anisotropy field [107]. The actual observed coercivity is only up to approximately 20% of the uniaxial anisotropy field [107]. Therefore, the driving force of investigating nanostructured bulk materials is furthermore related to the coercivity dependence of nanoparticles in dependence of their size, as shown in Fig. 1.1 [1, 108]. It shows a significant change of the coercivity with the reduction of the particle size in the regime of the single domain transition. Therefore, it is natural to investigate the influence of the mean grain size on the coercivity of bulk materials. The increasing coercivity can be originated by a rearrangement of the domains due to reduction of the grain sizes and due to changes in the overall electronic structures as a result of the increasing areas of interfaces. Due to these facts, the changes in the electronic structure studied by the hyperfine interaction parameters were in the main focus of the presented work.

Synthesis of nanostructured composites. Two different routes were followed to obtain nanostructured iron oxide composites containing magnetite. In the first approach, a stoichiometric mixture of hematite and iron according to Eq. (4.1) was blended and synthesised under FAST conditions. In the second approach, magnetite was taken directly as a precursor. The sintering applying FAST was performed with a constant process time to ensure comparable processes applying 50 MPa uniaxial pressure onto the sample, a holding time of a certain temperature in the regime of 450°C to 950°C of 5 min and a natural cooling of 30 min for each sample. For both precursor systems two different initial particles sizes of the used precursor materials were used, to observed the influence of the initial particle size on the densification behaviour and the influence on the grain sizes of the post-sintered samples.

Synthesis of magnetite by a stoichiometric mixture of hematite and iron.

Utilising a stoichiometric mixture of hematite and iron was promising due to the fact that the initial grain size of magnetite was 0. The synthesis of hematite and iron with an initial particle size of 190(10) nm and 220(60) nm, respectively, led to stable bulk materials in the temperature regime of 600°C to 950°C. The post-sintered samples showed an exponential grain growth with increasing sintering temperature which is in agreement with the description of grain growth in [25] where the grain growth depends on the reaction rate which is an exponential function in dependence of the sintering temperature. Furthermore, X-ray diffraction was performed on the post-sintered samples. The refinement of the diffractograms showed that the assumed transition Eq. (4.1) does actually take place in two steps. In the first step, hematite and iron form magnetite and wustite, see Eq. (4.2). In the second step, wustite and hematite form pure magnetite, see Eq. (4.3). The synthesis of magnetite via a stoichiometric mixture of hematite and iron was shown by ball-milling in an inert atmosphere [109]. It was pointed out that the role of the iron in this transition is not clear in the process since hematite forms magnetite at temperatures around 350°C to 500°C, magnetite and, furthermore, maghemite at temperatures around 250°C to 350°C [110]. Hematite forms wustite in a hydrogen atmosphere at temperatures below 570°C [111]. In the case of the stoichiometric mixture of hematite and iron in vacuum, iron reduces the hematite to magnetite while oxidising to wustite. Additionally, wustite is thermodynamically unstable below 570°C and it exhibits strong deviations from stoichiometry [112]. With this nonstoichiometric structure wustite enables magnetite to nucleate and to form islands [112] leading with hematite to nearly pure magnetite at higher sintering temperatures.

The crystal unit edge of magnetite stayed approximately constant for all sintering temperatures, only a tendency of the crystal unit edge to decrease was observed. Furthermore the mean crystallite size was determined by Rietveld refinement. The crystallite size showed the same behaviour as the mean value of the grain size leading to the conclusion that the determined grains are actual single crystals.

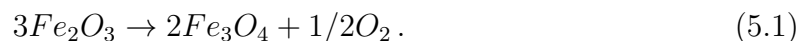
The fitting models for the Mößbauer spectra were built on the results of the X-ray diffraction. The relative intensities of the contributing phases, hematite, iron, magnetite and wustite were also identified and showed the same behaviour as in the diffraction studies. From the contributions of the different sites of magnetite also the stoichiometry was determined, according to Eq. (3.2). It was shown that the number of vacancies is small in the regime of 0.016, showing only a tendency to increase with increasing sintering temperature. This showed that the derived magnetite is nearly stoichiometric which is supported by the used stoichiometry of hematite and iron precursor mixture. The derived hyperfine interaction parameters showed changes for small sintering temperatures, which were mainly observed on magnetite A-sites. The hyperfine interaction parameters on magnetite B-sites only showed small deviations from being constant. The origin of these changes in the hyperfine parameters for magnetite A-sites can have several origins. They can be related to changes in the grain structure or to changing stoichiometry. Furthermore, they can be an artefact of the fitting procedure due to the changing ratio of hematite to magnetite. The changes in the stoichiometry can be excluded as the origin of the changes in the hyperfine interaction parameters of

magnetite A-sites, since the stoichiometry was determined to be constant for all sintering temperatures. The derived minimal crystallite size of the post-sintered sample sintered at 600°C was 124(1) nm. Therefore, it is possible that the observed effects are a result of finite sizes of the grains. Nevertheless, the probability density distributions showed no significant changes for any post-sintered composites. Due to this fact, it is assumed that the observed changes are an artefact of the fitting procedure and not actual changes in the electronic structure due to an increase of the area of interfaces at the grain boundaries.

Since the mean grain sizes of the previous samples sintered from hematite and iron precursors led to huge grains, in a further approach smaller initial particle sizes of the precursor were used. The hematite precursor had a mean particle size of 26(3) nm. Since no iron powder was available with such a mean particle size, the previously used powder was grinded in a planetary ball for 10 h, the mean grain size did only reduce to 160(40) nm, but the actual crystallite size of the particles reduced to 27(2) nm. The sintering of these precursors led to stable samples in the temperature regime from 450°C to 950°C. The mean grain size of the post-sintered samples showed that the sintering of the smaller initial precursor powders led to bigger grain sizes of the post-sintered samples. Furthermore, comparable results were obtained in this series.

The transition described in Eq. (4.1) shows that the standard enthalpy for the products is smaller than the ones of the reactants [113]. Due to this fact, the reaction should be exothermal. Considering a smaller initial particle size of the reactants for the hematite and iron mixture with 26(3) nm compared to the 190(10) nm, the free energy of the smaller particles is bigger. Therefore, the energy barrier separating the reactants from the products in the Eq. (4.1) is smaller and a bigger reaction rate and an enhanced crystallite growth can be observed.

Synthesis of magnetite from magnetite precursor. For the sintering of pure magnetite two different precursor powders with 120(35) nm and 27(2) nm mean particle sizes were used. The sintering of the precursor powders with 120(35) nm initial particle size led to composite bulk materials which were stable in the temperature regime from 600°C to 950°C. The smallest determined grain size was 181(29) nm for the smallest sintering temperature. Furthermore, the observed grain growth in dependence of the sintering temperature was exponential. The high energy X-ray diffraction revealed that the composition of the post-sintered samples is approximately 70% magnetite and 30% hematite. The volume fraction of magnetite shows a tendency to increase from 66.5(5)% from the smallest sintering temperature to 73.6(7)% for the highest sintering temperature. Nevertheless, for high sintering temperatures no abrupt change in the composition due to a reduction of hematite above 600°C [12] was observed. A reduction of hematite would also result in an oxygen release according to



An increase in the pressure inside the furnace was not observed in any sintering procedure.

The observed changes in the composition can be related to the nonstoichiometry of the precursor powder. The number of vacancies per formula unit of the precursor magnetite was 0.125(3). Considering the approach of a solid solution of magnetite and maghemite in nonstoichiometric magnetite and equal Lamb-Mössbauer factors for magnetite A- and B-sites and for maghemite, this leads to the conclusion of 34.9(1.5)% maghemite in the precursor powder. Following this approach, it is emphasised that the γ -Fe₂O₃ is not stable under FAST conditions and it transforms into the stable α -Fe₂O₃, hematite. The tendency of the increasing volume fraction of magnetite can be interpreted as a partial reduction of hematite, according to [12], even if no significant change in the pressure inside the furnace was observed.

The crystal unit edge of magnetite was approximately constant and only tentatively increased with increasing sintering temperature. The derived crystallite sizes of magnetite also showed an exponential growth in dependence of the sintering temperature. The observed crystallite size was approximately half of the grain size leading to the conclusion that the observed grains are not single crystals but were an agglomeration of several crystals.

The hypothesis that the maghemite in the solid solution is not stable and transformed to hematite while the stoichiometric part of the magnetite powder is stable under FAST conditions is supported by the determined stoichiometry of magnetite in the post-sintered samples. The number of vacancies per formula unit was determined to be around 0.025 with a tendency to decrease.

Furthermore, the determined hyperfine interaction parameters are constant for all sintering temperatures and only show slight tendencies to decrease or increase. Also the probability density distributions of the hyperfine parameters do not show significant changes for the whole series. Due to this fact it can be concluded, that for crystallite sizes above 100 nm probably not influence of the grain size on the electronic structure can be shown.

Hyperfine interactions of nanostructured composites sintered from magnetite precursor. The sintering of magnetite precursor powder with an initial particle of 27(2) nm led to significantly smaller grain sizes for small sintering temperature. Stable bulk materials were obtained in the temperature regime from 450°C to 950°C. Nevertheless, the determined volume fraction of magnetite and hematite phases present in the samples showed that the main part of the post-sintered samples consisted of hematite. Only approximately 30% of the volume fraction was magnetite in each sample. Assuming a solid solution of magnetite and maghemite in nonstoichiometric magnetite the contribution of maghemite in the precursor powder was 57.7(2.0)%. The volume fraction of hematite was bigger by 10%. However, this can also be a result of possibly different Lamb-Mössbauer factors of the contributing subspectra in the Mössbauer spectra or other artefacts.

The crystal unit edge of magnetite showed small changes which could be described by parabolic variation. Nevertheless, the changes in the crystal unit edge were not significant. Furthermore, the crystallite sizes of the particles were determined to be smaller than 80 nm, therefore to be in the regime of the single domain size of magnetite,

for the first six samples. The crystallite sizes increased exponentially with increasing sintering temperature and showed a similar behaviour as the grain sizes of the samples. The Mößbauer spectroscopy results revealed that the stoichiometry of the sample changed in dependence of the sintering temperature. With an increase in the sintering temperature the number of vacancies per formula unit of magnetite decreased, leading to stoichiometric magnetite phase for higher sintering temperatures. Furthermore, changes in the hyperfine interaction parameters were observed for magnetite A-, as well as, B-sites.

The isomer shift of magnetite A-sites showed a tendency to increase, while the mean value of the isomer shift of magnetite B-sites tend to decrease. The mean magnetic hyperfine field for both sites of magnetite showed an increase with increasing sintering temperature. Furthermore, the quadrupole splitting was approximately constant for magnetite A- and B-sites. Additionally, the probability density distributions of magnetite A- and B-sites showed changes in dependence of the sintering temperature. For smaller sintering temperatures broader partially integrated probability distributions were observed, while for higher sintering temperatures the probability density distributions were comparable to the probability density distributions of the reference material. For magnetite A-sites, strong correlations between all hyperfine interaction parameters were observed for small sintering temperatures. For magnetite B-sites, only strong correlations for the isomer shift and the magnetic hyperfine field were observed for small sintering temperatures. For the quadrupole splitting and the magnetic hyperfine field a medium correlation was observed, while for the isomer shift and the quadrupole splitting no significant correlations were present.

The changes in the mean values of the hyperfine interaction parameters can have several origins as mentioned before. The changes as an artefact of the fitting procedure due to an overlap of the hematite and the magnetite phases can be excluded, since no significant changes in the volume fractions of this two materials were observed.

Furthermore, it is possible that the observed changes in the hyperfine parameters, their distributions as well as their correlations are a result of the changing stoichiometry of magnetite. Since magnetite is one of the most investigated materials by Mößbauer spectroscopy, the influence of the stoichiometry on the hyperfine parameters of magnetite is well known. It was reported that magnetite B-sites do not show any significant changes in the isomer shift and in the magnetic hyperfine field for the number of vacancies per formula unit δ smaller than 0.14 [24]. For magnetite A-sites, the isomer shift should increase with increasing δ , and also the magnetic hyperfine field should show an increase [24]. Tab. 5.1 presents the influence of the stoichiometry in comparison to the observed mean hyperfine interaction parameters determined for the sintered series from the magnetite precursor with an initial particle size of 27(2) nm.

The meaning of the arrows in Tab. 5.1 correlates to the observed changes in dependence of the sintering temperature. It is to be seen, that most of the observed changes cannot be explained by the changes in the stoichiometry of the sintered samples. Additionally, the broadening of the partially integrated density distributions of the hyperfine interaction parameters cannot be explained by these changes. It is possible that the stoichiometry has an influence on the observed changes in the hyperfine parameters,

	observation		stoichiometry	
	A	B	A	B
IS	↓	↑	↓	-
$\mu_0 H_{hf}$	↑	↑	↓	-
QS	-	-	-	-

Table 5.1: Observed changes in the mean values of the hyperfine parameters of magnetite in comparison with the changes of the hyperfine parameters due to changes in the stoichiometry of magnetite.

but they cannot be the origin.

Due to this facts, it is shown that the actual changes in the hyperfine parameters can only be a result of the different positions of the Mößbauer nuclei inside the nanostructured iron oxide composites due to a reduction of the grain size below 80 nm. These changes are actually representing changes in the electronic structures of the post sintered composites, which will have furthermore influence on the macroscopic properties of these materials.

Chapter 6

Conclusions

The presented work was divided into two parts. The first part contained the interpretation of Mößbauer spectra of nanostructured materials, while the second part had the main focus on the synthesis and characterisation of nanostructured bulk materials. The chosen material systems were the iron oxides, due to the metastability of the iron oxides and the huge single domain size of magnetite.

The Lorentz and the simple Voigt model are the mainly used fitting routines in the available literature. The application of the Lorentz model results in reasonable fits which can reproduce the Mößbauer spectra of iron oxide nanoparticles. With the simple Voigt model in contrary, the features of the Mößbauer spectra were not reproduced satisfactorily. It was emphasised that the best suitable fitting procedure to interpret Mößbauer spectra of nanostructured materials is an extended Voigt model. The assumption of probability density distributions of all hyperfine interaction parameters with possible correlations is most reasonable. Nevertheless, due to the huge number of fitting parameters in this model an over-parametrisation is possible.

The application of the extended Voigt model onto a series of co-precipitated nanoparticles showed that the resulting mean hyperfine parameters, as well as, their probability density distributions and the correlations between these parameters are consistent over the whole series leading to the conclusion that the resulting fits lead to reliable hyperfine interaction parameters, probability density distributions and correlations between these distributions.

Furthermore, it was shown that different correlations between the hyperfine parameters are present at the two different sites of magnetite. These different correlations indicate that different effects are dominating magnetite A- and B-sites. Due to the fast electron hopping on the B-sites of magnetite intrinsic effects like lattice strain, stoichiometry, disorder, as well as, surface effects appearing in nanoparticles can be dominant. At the A-sites including iron ions excluded from the pair-localised hopping process from the B-sites, the behaviour can be dominated by whole-particle effects creating a possibility of observing changes in the hyperfine parameters which can be dominated by the actual particle size distribution. Nevertheless, this needs further investigation.

While the application of the extended Voigt model on nanoparticles has its limitations due to the time dependence of the Hamiltonian containing the hyperfine interaction parameters, the application of this model on nanostructured bulk materials has no limitations due to the fact that the Hamiltonian is static.

The synthesis of nanostructured iron oxide composites was realised via two routes. In the first approach magnetite was synthesised by a stoichiometric mixture of hematite and iron. In both cases, the grain growth and the crystallite growth of magnetite showed an exponential increase. The actual transition of hematite and iron to magnetite takes

place in two steps. In the first step, hematite and iron form magnetite and wustite and in the second step hematite and wustite form magnetite. The synthesised magnetite showed only small number of vacancies per formula unit. Furthermore, the crystal unit edge for magnetite in the two series sintered from hematite and iron was approximately constant. The hyperfine parameters showed slight variations for the series sintered from the bigger initial particle size, but these changes are probably related to an artefact of the fitting procedure due to an overlap of contributing subspectra from magnetite and hematite in the Mößbauer spectra. The probability density distributions also did not show significant changes for over both series.

It is worth to point out that the actual synthesis of magnetite from the smaller initial particles size of the precursor powders led to bigger grain and crystallite sizes. This is a result of the exothermic reaction of hematite and iron to magnetite and the bigger surface energy in the smaller particles.

The synthesis of magnetite directly from magnetite precursors showed that nonstoichiometric magnetite is not stable under FAST conditions. The nonstoichiometric magnetite splits into mainly stoichiometric magnetite and hematite for a wide temperature range. The grain and crystallite growth was shown to be exponentially increasing with rising sintering temperature. The sintering of nonstoichiometric magnetite with the bigger initial particle size resulted in constant hyperfine interaction parameters for all sintering temperatures. Additionally, the probability density distributions of this hyperfine parameters, as well as, their correlations did not vary with temperature.

In the series sintered from magnetite with the smaller initial particle size, the mean grain size and the mean crystallite size was below the single-domain size for magnetite for small sintering temperatures. It was shown that the hyperfine parameters, their distributions, as well as, the correlation between these parameters exhibit changes for small sintering temperatures which cannot be an artefact of the fitting procedure or the changing stoichiometry. Ipso facto these changes are a result of changes in the electronic structure in the nanostructured bulk material and are originated by the small size of the grains in the range of the single domain size.

Furthermore, the investigation of nanostructured iron oxide bulk materials with Mößbauer spectroscopy is also an interesting research field to understand the behaviour of magnetic nanoparticles. The Mößbauer spectra of nanostructured bulk materials can be interpreted as strongly interacting magnetic nanoparticles. Therefore, the Hamiltonian describing the Mößbauer nuclei is static and only the influence from different positions inside the samples are contributing to the collected spectra.

Chapter 7

Outlook

It was indicated that on magnetite A- and B-sites different effects are dominant which are influencing the hyperfine interaction parameters and their correlations. To verify this, further studies on magnetite nanoparticles are necessary. Since many parameters can influence the Mößbauer spectra of magnetite, the particles have to be characterised concerning their sizes, agglomeration behaviour, exact composition, stoichiometry and possible particle interactions.

Furthermore, temperature dependent Mößbauer spectroscopy can be helpful to study the influence of the different dominant effects. Since the same particles are investigated, the composition and stoichiometry of the particles and the exchange interactions between the particles should not change. Due to this fact, the broadening of Mößbauer lines in dependence of the temperature can give information about the changes in the correlations of the nanoparticles helping to understand the origin of the correlations between the hyperfine interaction parameters. Here, also time dependent measurements applying synchrotron radiation are suitable. The correlations between the hyperfine interaction parameters should also influence the beating pattern in nuclear resonant scattering experiments.

The physical properties of nanostructured bulk materials, especially soft and hard magnetic materials are widely unknown and due to this fact further research in this area is possible. Due to the metastability of iron oxides and the large single domains of magnetite and also maghemite, influences of grain sizes offer great possibilities of describing these physical properties in dependence of the mean grain size. Also exchange interactions between antiferromagnetic and ferrimagnetic materials can be studied.

The further exchange of iron to cobalt or nickel also gives the opportunity to synthesise composites of soft and hard magnetic materials and to study their exchange interactions as functions of the composition and grain size.

For the ongoing research in the direction of nanostructured magnetic materials the possibility to obtain hysteresis curves is essential and this is also necessary in the ongoing work in the case of iron oxide composites.

It was shown that the first changes of the electronic structure studied by the hyperfine interaction parameters derived by Mößbauer spectroscopy can be seen for grain sizes below 80 nm for magnetite. To further study the changing hyperfine interactions in dependence of the grain sizes, composites containing a bigger amount of magnetite would be obtained. Nevertheless, purchasing magnetite with a better stoichiometry and small particle size is difficult since magnetite ages. Magnetite oxidises to maghemite which further transforms into hematite. Therefore, it is necessary to find a simple synthesis route like the co-precipitation of magnetite from iron chlorides and to use the synthesised magnetite nanoparticles as precursors for the consolidation process. The

advantage of the self-prepared nanoparticles is, that the exact age of the nanoparticles is known. Chemically prepared nanoparticles also have a great disadvantage. In a single synthesis of nanoparticles, only a few gram of particles maximum can be synthesised. When the amounts of materials used in the synthesis is oversized, the conditions during the synthesis are not homogenous and the resulting nanoparticles cannot be reproduced. Furthermore, the used consolidation process can be further optimised to minimise grain growth. The heating rate of the samples can be increased and the holding time could be reduced. The Tycho sintering laboratory in Rostock offers the world wide unique possibility to use rapid gas cooling in the cooling process of the samples, which shortens the cooling time of each sample significantly and can be used in further studies.

Appendix A

Reference sample and nanoparticles

A.1 Reference sample

Fig. A.1 shows an exemplary TEM picture of the reference material.

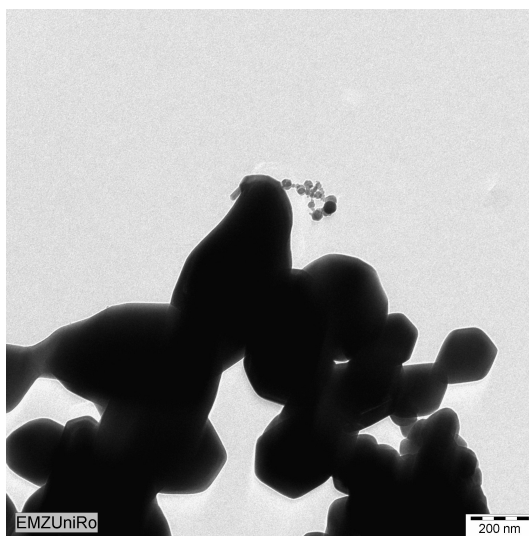


Figure A.1: Exemplary TEM pictures of the reference material.

A.2 Nanoparticles

An overview of the used materials used for the synthesis of the nanoparticles are listed in Tab. A.1. Additionally, the fraction of Fe^{3+} ions resulting from the mixed precursors used during the synthesis is given.

TEM images of the precipitated nanoparticles are shown in Fig. A.2.

Sample	m_{NaOH} [g]	$m_{FeCl_2 \cdot 4H_2O}$ [g]	$m_{FeCl_3 \cdot 6H_2O}$ [g]	$\zeta(Fe^{3+})$
S1	5	5	0	0
S2	5	4	1	0.16
S3	5	3	2	0.33
S4	5	2	3	0.52
S5	5	1	4	0.75
S6	5	0	5	1.00

Table A.1: Overview of the materials used in the synthesis and $\zeta(Fe^{3+})$ - the initial weight fraction of Fe^{3+} ions.

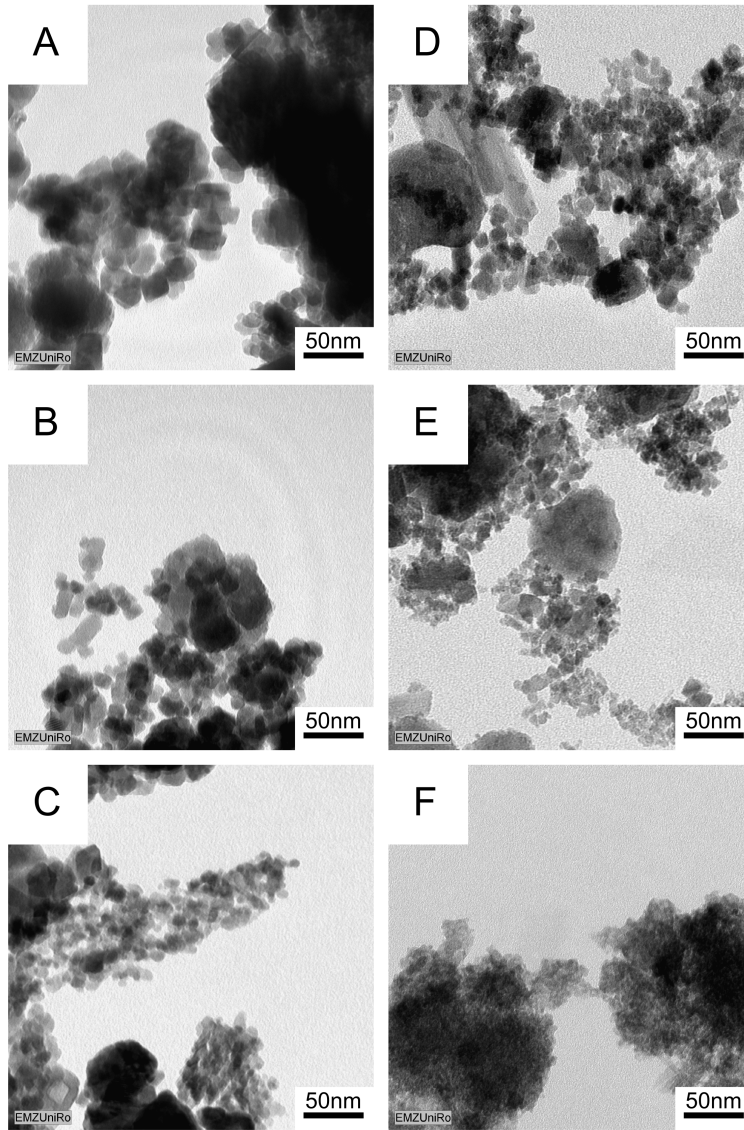


Figure A.2: Exemplary TEM pictures of the prepared samples. A) $\zeta = 0$, B) $\zeta = 0.16$, C) $\zeta = 0.33$, D) $\zeta = 0.52$, E) $\zeta = 0.75$ and F) $\zeta = 1.0$.

Appendix B

Precursor materials

In this chapter the chosen precursor materials are described in detail. All powders were purchased from Alfa Aesar with a purity above 99%. Since iron with smaller particles sizes than 220 nm were commercially not available, the powder was ball milled for 10 h in a planetary ball mill with a ball-to-powder-weight ratio of 10:1 in stainless steel jars with 200 rpm in hexane. The materials were investigated by transmission electron microscopy, high energy X-ray diffraction and Mößbauer spectroscopy. Exemplary TEM pictures of the precursors are shown in Fig. B.1.

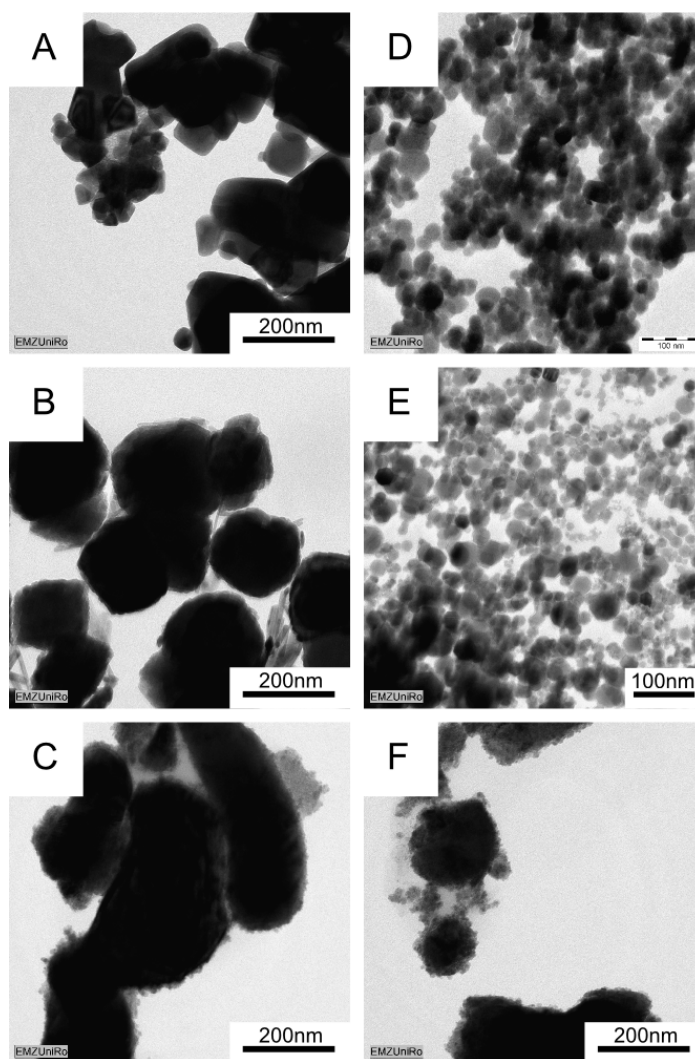


Figure B.1: Exemplary TEM pictures of the used precursor materials. A) magnetite $d_1 = 120$ nm, B) hematite $d_1 = 190$ nm, C) iron $d_1 = 220$ nm, D) magnetite $d_2 = 27$ nm, E) hematite $d_2 = 26$ nm and F) iron $d_2 = 160$ nm.

The particles in Fig. B.1 A,B and C are significantly bigger than in D,E and F. For the magnetite and hematite precursor images, particles can be identified directly. For the iron precursor images, the big dark ovals are particles, but additionally smaller particles around these particles are agglomerated. This can be a result of direct oxidation of the iron particles at the surface or during the preparation of the materials for the transmission electron microscope. Furthermore, iron particles with $d_2 = 160$ nm seem to build bigger agglomerations which are built out of small crystallites. The mean values of the particle sizes derived by TEM are listed in Tab. 4.1.

Precursor	d [nm]	phase	a [Å]	c [Å]	d_c [nm]
magnetite	120	M	8.3842(1)	-	108(4)
magnetite	27	M	8.3584(2)	-	32(2)
hematite	190	H	5.0326(1)	13.7638(6)	207(5)
hematite	26	M	8.3375(7)	-	38(4)
iron	220	I	2.86495(2)	-	346(40)
iron	160	I	2.86512(3)	-	27(2)

Table B.1: Resulting parameters for the precursor powders determined by Rietveld refinement procedure. d - mean particle size determined by TEM, a and c - crystal unit edges and d_c - mean crystallite size. For the determined phase M corresponds to magnetite or maghemite, H to hematite and I to iron.

The high energy X-ray diffraction revealed, that the magnetite precursors are built only of iron oxides in the $Fd\bar{3}m$ state, which is consistent with the specifications from the supplier. For the hematite precursors, the powder with $d_1 = 190$ nm shows a structure typical for α - Fe_2O_3 , while the powder with $d_2 = 26$ nm shows mostly amorphous scattering and a small amount of an iron oxide in the $Fd\bar{3}m$ state, which was identified as maghemite according to the lattice constant [22]. The iron precursors only showed scattering from the cubic iron belonging to the space group $Im\bar{3}m$. Therefore, also the ball milling and further storage of the powder did not lead to further oxidation of the material. The mean crystallite size of the powder was determined to be 27(2) nm. Further details on the X-ray diffraction results are listed in Tab. B.1.

It is worth to mention, that the crystallite size for the precursor powders magnetite and for hematite are in good agreement with the particle size determined by transmission electron microscopy. This leads to the conclusion, that the particles consist of single crystallites. The resulting crystallite size for the iron powder is inconclusive since the crystallite size is significantly bigger than the particle size. The ball milled iron powder consists of small crystallites which tend to agglomerate.

Further details on the composition, structure and hyperfine interaction parameters were determined by Mößbauer spectroscopy. Fig. B.2 shows the Mößbauer spectra of all precursor powders.

Fig. B.2 shows the experimental and the calculated spectra of the investigated materials. Furthermore, if a spectrum consists of several subspectra, these subspectra are presented in colour. Both magnetite samples show only subspectra belonging to magnetite A- and B-sites. A significant change in the intensity ratio of the contributing subspectra is to be

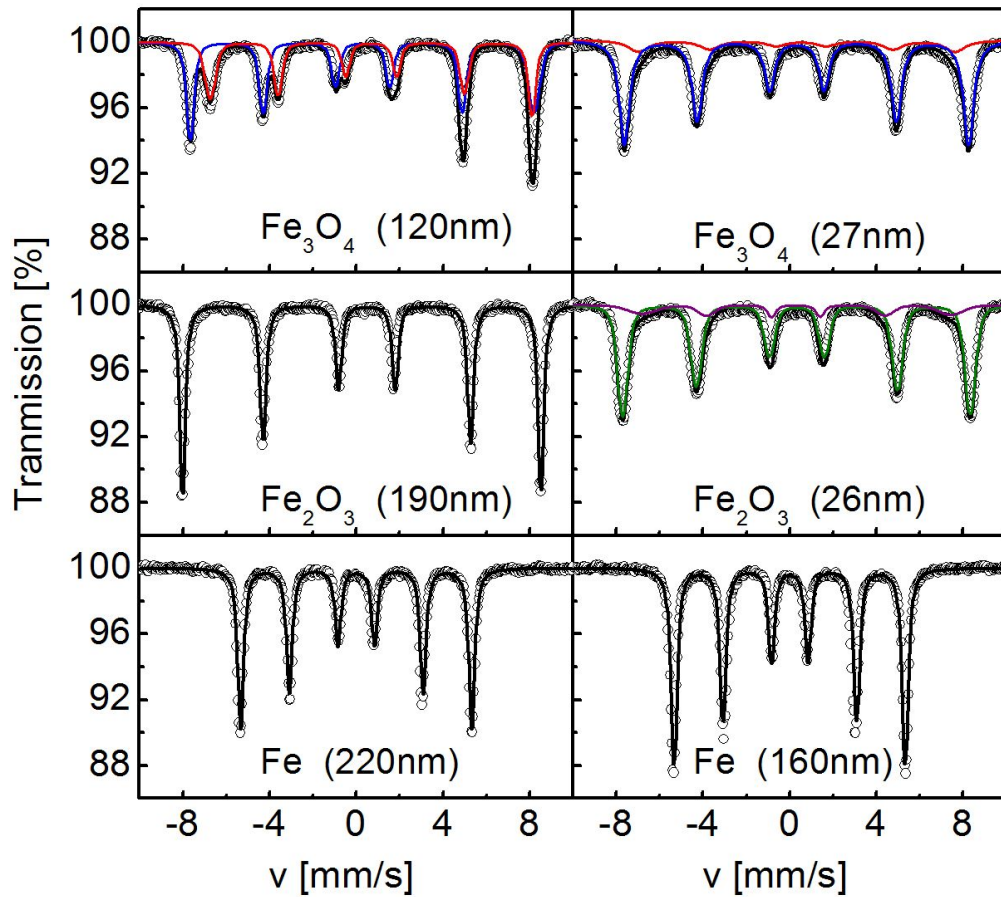


Figure B.2: Mössbauer spectra of the precursor powders. The experimental and calculated spectra are shown in open dots and as a black line, respectively. Additionally for spectra with subspectra, the subspectra are presented in colour. Blue - magnetite A-sites, red - magnetite B-sites, green - hematite and purple - maghemite.

seen. The stoichiometry for both magnetite powders was determined according to Eq. (3.2). For magnetite with $d_1 = 120$ nm particle size the vacancies per formula unit are 0.125(9) and for the magnetite with $d_2 = 27$ nm 0.202(12). These results correspond to the diminishment of the lattice constants listed in Tab. B.1 as the number of vacancies increases [22].

The hematite precursor powders show different spectra for the different particle sizes. For the spectrum from hematite powder with $d_1 = 190$ nm only a single sextet is observed, while for the spectrum from hematite with $d_2 = 26$ nm two subspectra are noticed. The subspectrum presented in green in Fig. B.2 corresponds to hematite and the second subspectrum presented in purple to small maghemite particles with slightly reduced magnetic hyperfine field but a broad line width. The additional amount of maghemite in the powder leads to the conclusion, that the hematite powder was obtained in an oxidation process of magnetite particles over maghemite, where the transformation to hematite was not complete.

For both iron precursors only a single sextet corresponding to α -Fe was observed. The hyperfine parameters do not change significantly also with the reduction of the crystal-

precursor χ^2	c	RI [%]	IS [mm/s]	QS [mm/s]	$\mu_0 H_{hf}$ [T]	ρ_{ISQS}	ρ_{ISz}	ρ_{QSz}
magnetite d ₁ 4.13	MA	56.6(4)	0.287(4) 0.095*	-0.011(3) 0.094*	49.17(3) 0.31*	0.27	0.79	0.80
	MB	43.4(4)	0.688(5) 0.067*	-0.002(4) 0.069*	46.02(4) 0.67*	-0.26	-0.30	-0.37
magnetite d ₂ 2.79	MA	71.8(3)	0.323(3) 0.115*	-0.007(3) 0.117*	49.25(3) 0.38*	0.04	-0.06	0.41
	MB	28.2(2)	0.433(38) 0.383*	-0.036(20) 0.375*	45.70(37) 0.62*	-0.28	-0.15	-0.91
hematite d ₁ 5.36	H	100	0.370(1) 0.037*	-0.118(1) 0.038*	51.25(1) 0.04*	-0.32	-0.10	0.97
hematite d ₂ 2.89	H	84.5(4)	0.322(3) 0.128*	-0.090(3) 0.131*	49.70(3) 0.07*	-0.05	-0.47	0.90
	M	15.5(4)	0.310(31) 0.036*	-0.019(34) 0.048*	44.17(87) 3.5*	-0.51	-0.49	-0.51
iron d ₁ 4.21	I	100	-0.002(1) 0.037*	-0.000(1) 0.038*	33.05(1) 0.000*	0.00	0.00	0.00
iron d ₁ 3.67	I	100	-0.001(1) 0.048*	-0.003(1) 0.048*	33.04(1) 0.01*	-0.00	0.03	-0.04

Table B.2: Composition and hyperfine parameters of the precursor powders: c - component (Ma - magnetite A-sites, MB - magnetite B-sites, H - hematite, M - magnetite and I - iron), RI - relative intensity, IS - mean isomer shift, QS - mean quadrupole splitting, $\mu_0 H_{hf}$ - mean magnetic hyperfine field. Standard deviations of the mean value are indicated by *. ρ_{ISQS} , ρ_{ISz} , and ρ_{QSz} are the correlation parameters between the isomer shift and the quadrupole splitting, the isomer shift and the magnetic hyperfine field, and the quadrupole splitting and the magnetic hyperfine field, respectively. Additionally, the goodness of the fit χ^2 is mentioned below the name of the precursor.

lite size.

Detailed information on the hyperfine parameters of the corresponding subspectra for each precursor material are listed in Tab. B.2.

Appendix C

Composites sintered from hematite and iron precursor

C.1 Initial particle size $d = 190$ nm

Fig. D.5 shows exemplary SEM images of breaking edges of composites sintered from hematite and iron precursor powders with an initial particles size of around 190 nm. With an increasing sintering temperature also a direct increase of the mean grain size can be observed. Additionally, more necks are formed between the separate grains, especially for high sintering temperature a rather homogeneous surface is formed.

Fig. C.2 shows the diffractograms of all sintered composites. For each composite additionally the calculated pattern and the differential pattern are shown. Below the diffractograms the Bragg reflexes of magnetite and hematite are presented. It is worth to mention that additional reflexes in the diffractograms do not belong to an additional phase present in the sample but to magnetite and hematite. These reflexes are a result of the second harmonic not filtered out by the optics in the experimental set-up.

Fig. C.3 shows the Mößbauer spectra of all post-sintered composites from the series sintered from hematite and iron precursor with $d_i = 190$ nm. Additionally the calculated spectrum and the contributing subspectra are shown for every sample.

Fig. C.4 presents the calculated relative intensities derived from the Mößbauer spectra. The resulting relative intensities are comparable to the derived volume fractions of magnetite, hematite, iron and wustite from high energy X-ray diffraction.

The relative intensity of magnetite in dependence of the sintering temperature can be described by a logistic function $f_M = (100.00 - 98.00 / (1 + ([T_{sinter} - 273.15K] / 670.88/K)^{9.00})) \%$. The behaviour of hematite can be described by $f_H = (76.58 / (1 + ([T_{sinter} - 273.15K] / 691.06/K)^{10.98})) \%$. The relative intensity of the iron phase can be presented by a linear function $f_I = (13.50 - 0.0129 \cdot T_{sinter}/K) \%$ and the relative intensity of the wustite phase can be presented by a Gaussian distribution with $f_W = (6.049 \cdot \exp(-(T_{sinter} - 1006.82)^2 / 10043.4/K^2)) \cdot \%$.

C.2 Initial particle size $d = 26$ nm

Fig. C.5 shows exemplary SEM images of breaking edges of composites sintered from hematite and iron precursor powders with an initial particles size of 26 nm. With an increasing sintering temperature also a direct increase of the mean grain size can be observed. Additionally, more necks are formed between the separate grains. It is worth to point out that an exemplary SEM image from the post-sintered composites sintered

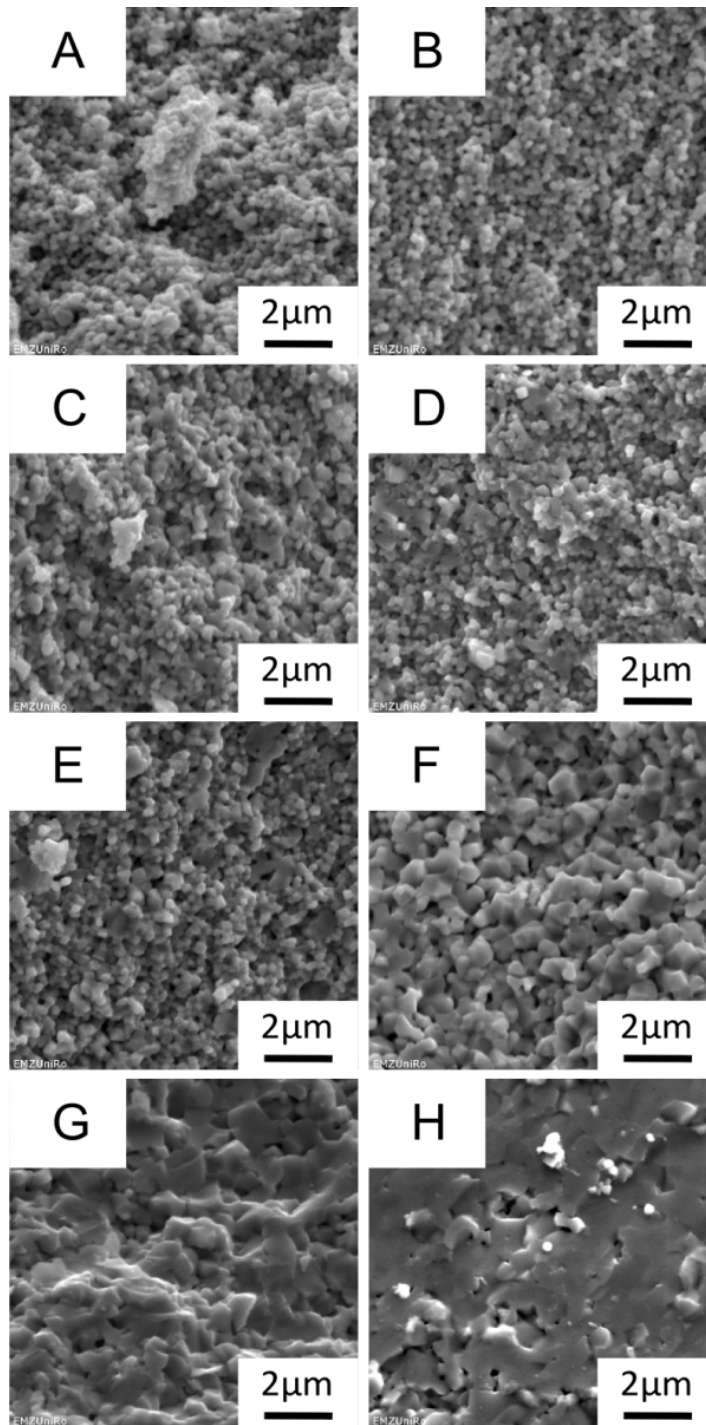


Figure C.1: Exemplary SEM images of breaking edges of post-sintered composites from hematite and iron precursor powders sintered at A) 600°C, B) 650°C, C) 750°C, D) 800°C, E) 850°C, F) 900°C and G) 950°C.

at 700°C is not shown due to editorial reasons. An increased grain growth compared to Fig. D.5 is to be seen.

Fig. C.6 shows the diffractograms of all sintered composites from the stoichiometric mixture of hematite and iron precursor with $d_i = 26$ nm. For each sample additionally the calculated pattern and the differential pattern are shown. Below the diffractograms

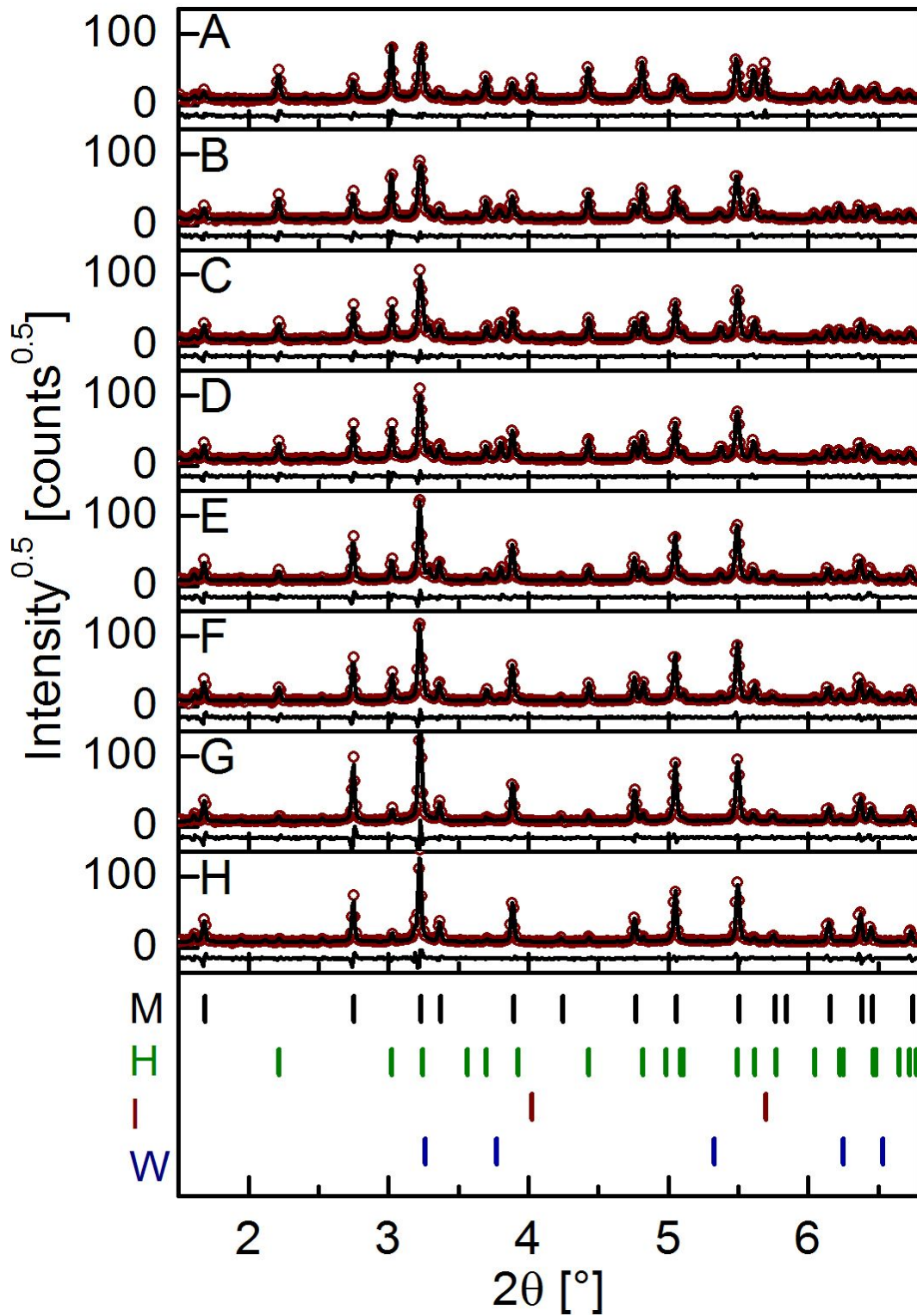


Figure C.2: High energy X-ray diffractograms of post-sintered composites from hematite and iron precursor powders sintered at A) 600°C, B) 650°C, C) 700°C, D) 750°C, E) 800°C, E) 850°C, F) 900°C and G) 950°C. For each diffractogram additionally the calculated and the differential pattern are shown. Below the diffractograms the Bragg positions of magnetite (M), hematite (H), iron (I) and wustite (W) are presented.

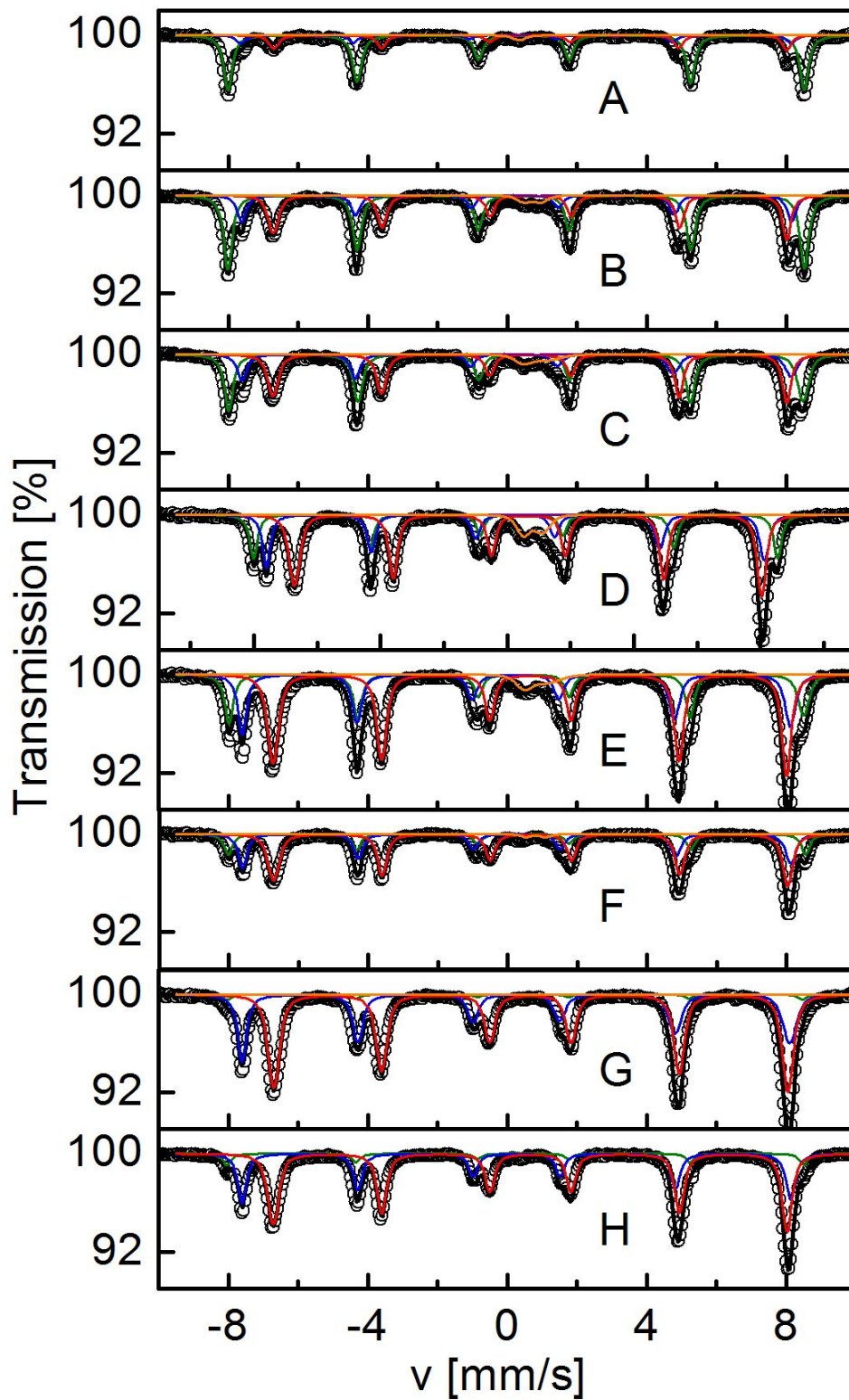


Figure C.3: Mössbauer spectra of post-sintered composites sintered at A) 600°C, B) 650°C, C) 700°C, D) 750°C, E) 800°C, E) 850°C, F) 900°C and G) 950°C. The experimental data are presented in open dots, the calculated spectra with a black line and the contributing subspectra in colour. Blue - magnetite A-sites, red - magnetite B-sites, green - hematite, purple - iron and orange - wustite.

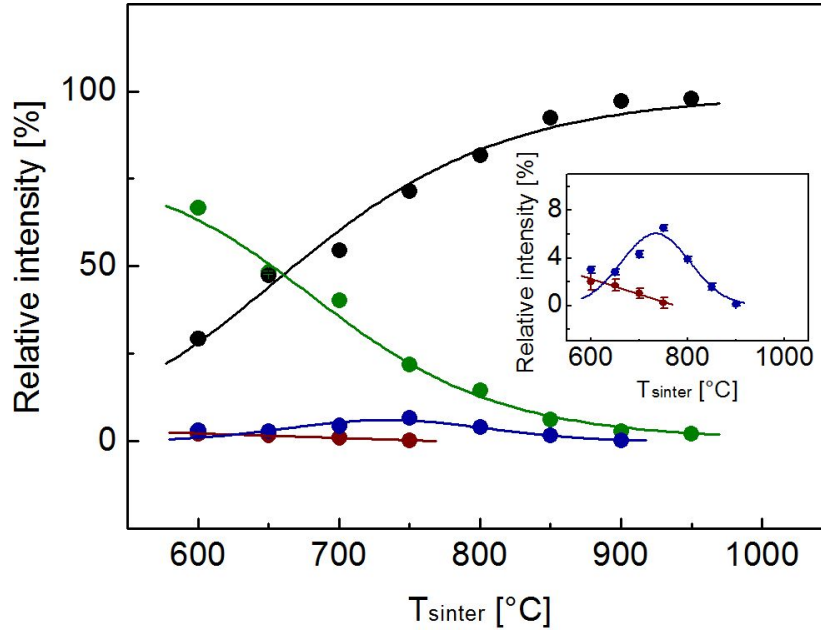


Figure C.4: Relative intensities of the contributing phase, magnetite (black), hematite (green), iron (red) and wustite (blue) in dependence of the sintering temperature T_{sinter} for the post-sintered composites from hematite and iron precursor powders.

the Bragg reflexes of magnetite, hematite, iron and wustite are presented. It is worth to mention that additional reflexes in the diffractograms do not belong to an additional phase present in the samples.

Additional to the expected hematite, iron and magnetite phase additional wustite is present in the samples as in the previous presented series. The resulting volume fractions of magnetite, hematite, iron and wustite were derived by Rietveld refinement and are presented in Fig. C.7. First a decreasing amount of iron and hematite is observed, while the volume fraction of magnetite increases. Additionally the volume fraction of wustite is increasing and reaches a maximum when the iron phase is disappearing. For high sintering temperatures nearly pure magnetite is observed. The volume fraction of hematite and magnetite phase can be described by logistic functions. It is worth to point out that the increase in magnetite phase can be described by two logistic function.

The behaviour of magnetite can be described by $vf_M = (62.11 - 62.11/[1 + ((T_{sinter} - 273.15K)/428.01/K)^{11.64}]) \%$ in the regime from 400°C to 600°C and $vf_M = (100 - 42.92/[1 + ((T_{sinter} - 273.15K)/728.84/K)^{13.16}]) \%$ from 600°C to 950°C. The changes in the volume fraction of hematite can be described by $vf_H = (85.71/[1 + ((T_{sinter} - 273.15K)/509.71/K)^{4.90}]) \cdot \%$. The amount of iron present in the sample can be described by a linear function with $vf_I = (9.092 - 0.00677 \cdot T_{sinter}/K) \%$ and wustite can be described by the formula $vf_W = (12.33 \cdot \exp(-(T_{sinter} - 934.01K)^2/3405.06/K^2)) \%$.

The repeated appearing of the additional amount of wustite in the composites supports the hypothesis that the assumed transition to magnetite of hematite and iron takes place in a two step procedure.

The crystal unit edges and the mean crystallite sizes derived by Rietveld refinement are shown in Fig. C.8. The crystal unit edge shows a tendency to decrease with increasing sintering temperature which can be described by a linear function with $a = (8.40598 - 8.22 \cdot 10^{-6} \cdot T_{sinter}/K) \cdot \text{Å}$. The crystallite size shows also an exponential grain growth which is described by $d_c = (98.12 + 0.00011 \cdot \exp(T_{sinter}/53.06/K)) \cdot \text{nm}$ in the regime between 450°C to 700°C. The crystallite size could not be determined for the other samples due to the fact that the changes in half width of the diffraction peaks were too small. It is worth to point out that these discrepancies between the resulting grain size from the SEM images and the diffractograms are a result of the huge crystallite size itself,

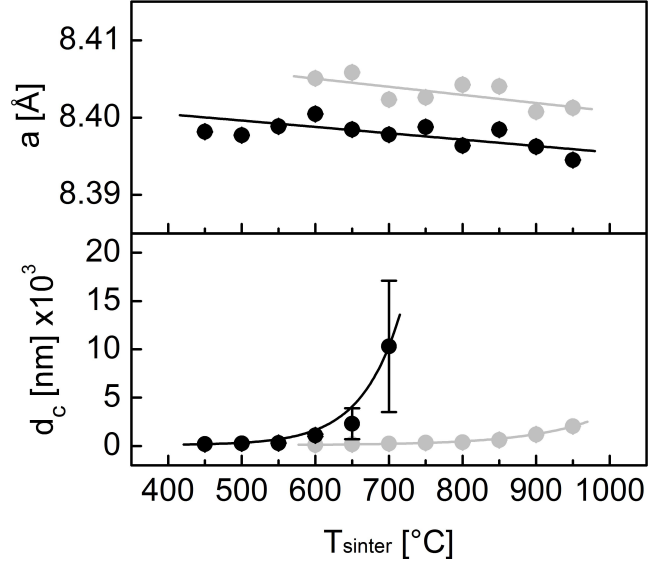


Figure C.8: Crystal unit edge a and mean crystallite size d_c of magnetite phase in dependence of the sintering temperature T_{sinter} for the post-sintered composites from hematite and iron precursor powders. Black - $d_i = 26$ nm and grey - $d_i = 190$ nm.

which makes the determination of the mean crystallite size with the XRD difficult and it is also possible that the breaking of the samples as a preparation for the imaging with the SEM led to an alternation of the actual grain structure of the composites.

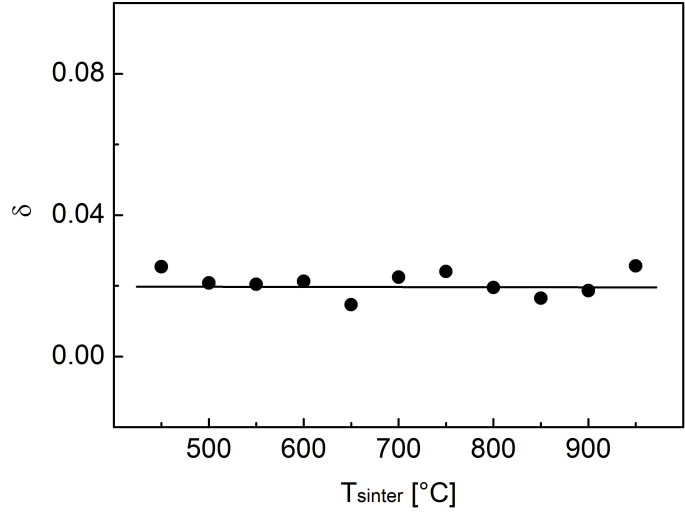
Fig. C.9 shows the Mößbauer spectra of all post-sintered composites from the series sintered from hematite and iron precursor with $d_i = 26$ nm. Additionally, the calculated spectrum and the contributing subspectra are shown for every sample.

Fig. C.10 presents the calculated relative intensities derived from the Mößbauer spectra. The resulting relative intensities are comparable to the derived volume fractions of magnetite, hematite, iron and wustite from high energy X-ray diffraction. Also in the Mößbauer spectra the additional wustite phase was observed, which had its maximum when the iron phase was disappearing from the post-sintered composites supporting the assumption of a two-step transition from hematite and iron to magnetite.

The relative intensity of magnetite in dependence of the sintering temperature can be described by a logistic function $f_M = (100.00 - 98.57 / (1 + ([T_{sinter} - 273.15K] / 536.42 / K)^{3.55})) \%$. The behaviour of hematite can be described by $f_H = (87.43 / (1 + ([T_{sinter} - 273.15K] / 547.35 / K)^{3.92})) \%$. The relative intensity of the iron phase can be presented by a linear function $f_I = (14.871 - 0.0148 \cdot T_{sinter}/K) \%$ and the relative intensity of the wustite phase can be presented by a Gaussian distribution with $f_W = (6.450 \cdot \exp(-(T_{sinter} - 964.68)^2 / 4016.00 / K^2)) \%$.

Furthermore, the stoichiometry determined from the Mößbauer spectra utilising the relative intensities from magnetite A- and B-sites are presented by the number of vacancies per formula unit in Fig. C.11.

It is to be seen that the number of vacancies per formula unit is very small. This means that the synthesised magnetite is nearly stoichiometric. The number of vacancies per formula unit magnetite can be described by a linear function with $\delta = 0.019998 - 3.581 \cdot 10^{-7} \cdot T_{sinter}/K$. The number of vacancies per formula unit only shows a small tendency to decrease with an increasing sintering temperature.



The determined hyperfine interaction parameters for magnetite A- and B-sites are shown in Fig. C.12. The hyperfine interaction parameters do not show significant

Figure C.11: Number of vacancies per formula unit of the post-sintered composites in dependence of the sintering temperature T_{sinter} .

changes as in the case of the post-sintered samples from hematite and iron precursor with an initial particle size of 190 nm. The changes in the hyperfine parameters for magnetite A- and B-sites can be described mainly by linear functions.

The changes in the mean isomer shift for magnetite A-sites can be described by $IS_A = (0.25869 + 1.096 \cdot 10^{-5} \cdot T_{sinter}/K) \cdot \text{mm/s}$ and the changes in the isomer shift for magnetite B-sites can be described by $IS_B = (0.65863 + 0.758 \cdot 10^{-5} \cdot T_{sinter}/K) \cdot \text{mm/s}$.

The mean magnetic hyperfine field can in both cases also be described by linear functions with $\mu_0 H_{hfA} = (49.084 - 3.094 \cdot 10^{-5} \cdot T_{sinter}/K) \cdot \text{T}$ and $\mu_0 H_{hfB} = (45.9450 - 2.526 \cdot 10^{-5} \cdot T_{sinter}/K) \cdot \text{T}$ for magnetite A- and B-sites, respectively.

The mean quadrupole splitting for magnetite A-sites can be described by the exponential function $QS_A = (-0.0036 - 7.779 \cdot 10^5 \cdot \exp(-T_{sinter}/41.67/K)) \cdot \text{mm/s}$. The mean quadrupole splitting for magnetite B-sites is constant and only shows a tendency to decrease which can be presented by a linear function with $QS_B = (0.014087 - 3.14 \cdot 10^{-6} \cdot T_{sinter}/K) \cdot \text{mm/s}$.

Fig. C.13 shows exemplarily the maps of the probability density distributions the hyperfine interaction parameters for the post-sintered composite sintered at 700°C. The probability density distribution do not show any significant changes with changing sintering temperatures. Also the probability density distributions and with this also the correlations between the hyperfine parameters are comparable to the results from the series sintered from magnetite precursor with an initial particle size of 120 nm shown in Fig. 4.15. Due to this fact it is concluded that the observed changes in the mean values of the hyperfine interaction parameters cannot be related to grain size effects for this series.

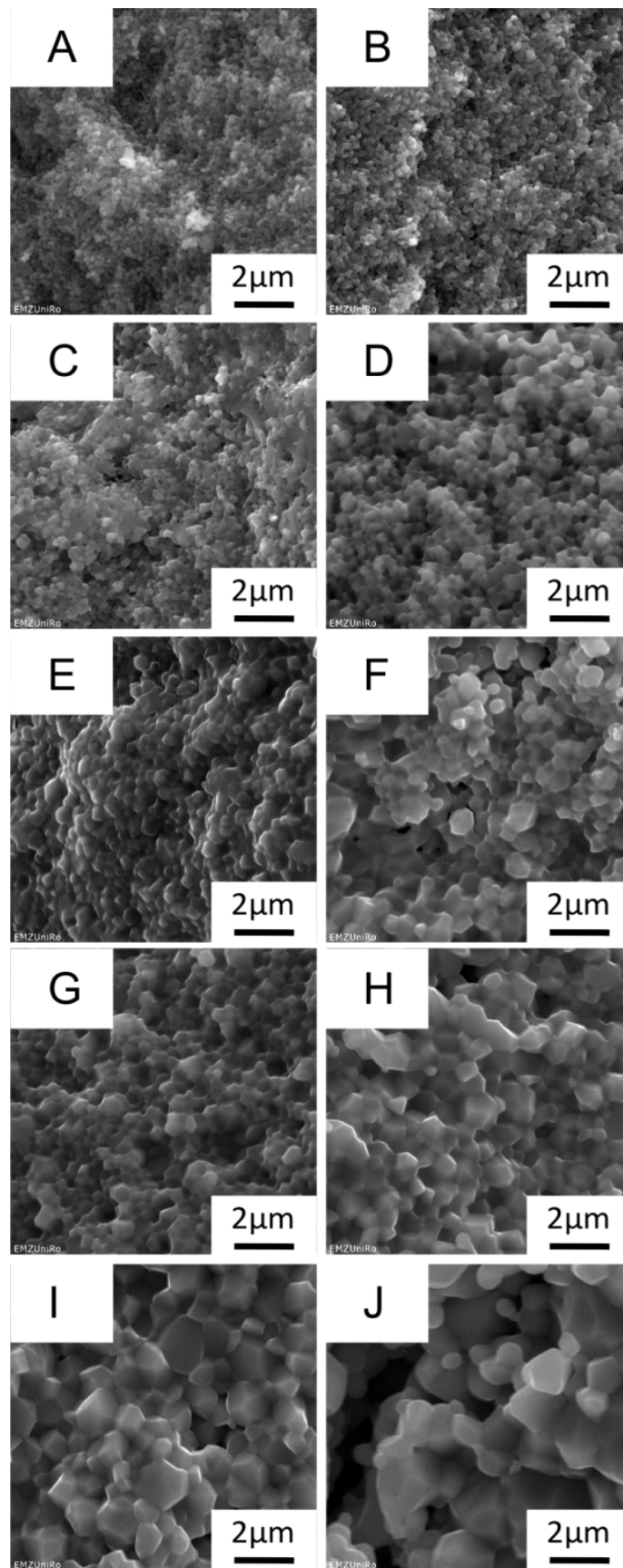


Figure C.5: Exemplary SEM images of breaking edges of post-sintered composites from magnetite precursor powders sintered at A) 450°C, B) 500°C, C) 550°C, D) 600°C, E) 650°C, F) 750°C, G) 800°C, H) 850°C, I) 900°C and J) 950°C.

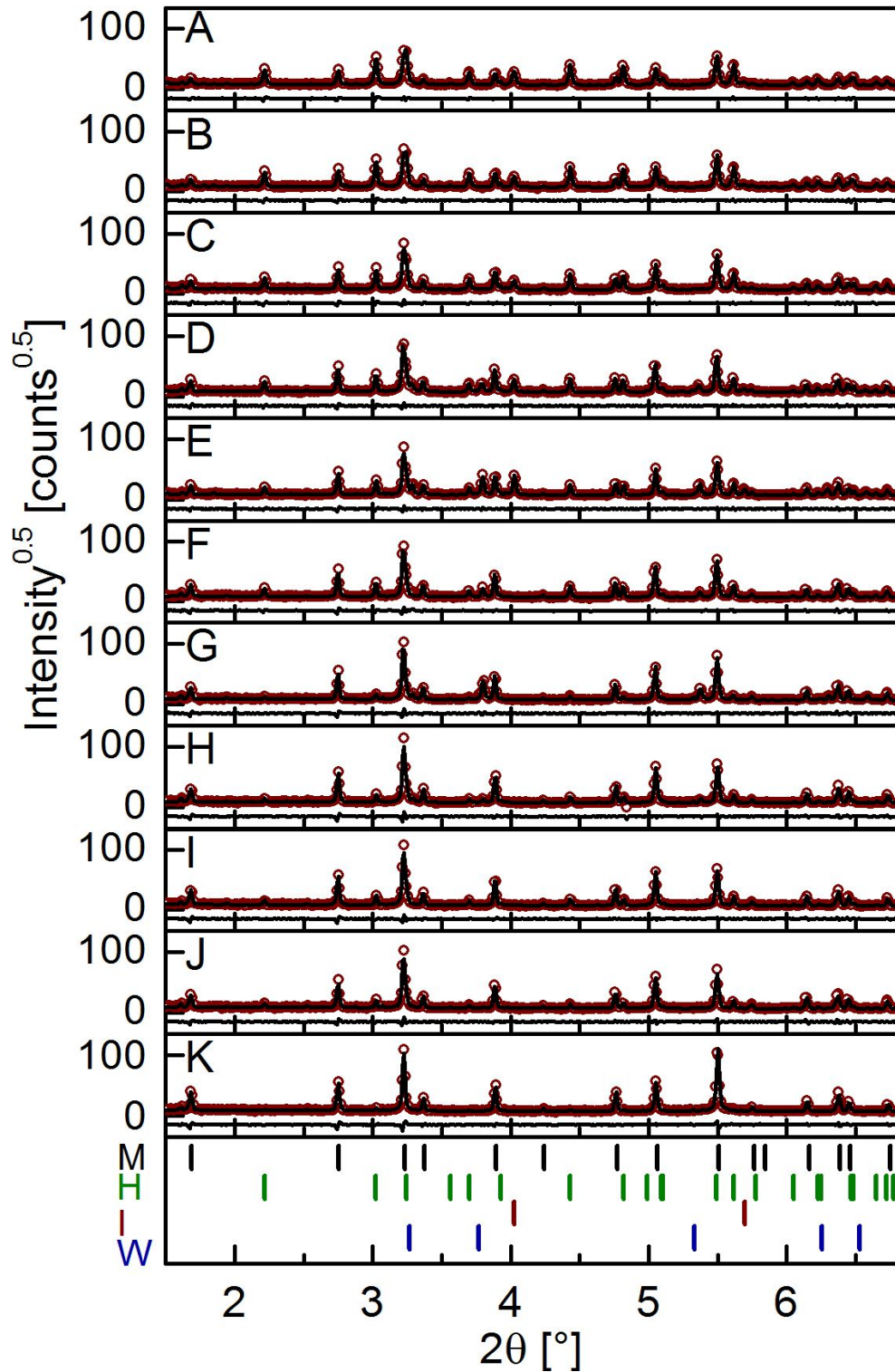


Figure C.6: High energy X-ray diffractograms of post-sintered composites from hematite and iron precursor powders sintered at A) 450°C, B) 500°C, C) 550°C, D) 600°C, E) 650°C, F) 700°C, G) 750°C, H) 800°C, I) 850°C, J) 900°C and K) 950°C. For each diffractogram additionally the calculated and the differential pattern are shown. Below the diffractograms the Bragg positions of magnetite (M), hematite (H), iron (I) and wustite (W) are presented.

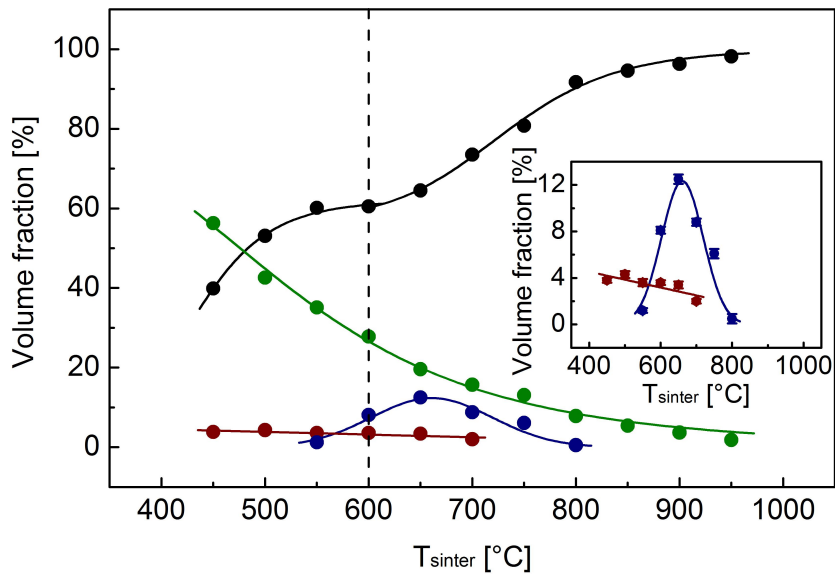


Figure C.7: Volume fractions of the contributing phase, magnetite (black), hematite (green), iron (red) and wustite (blue) in dependence of the sintering temperature T_{sinter} for the post-sintered composites from hematite and iron precursor powders.

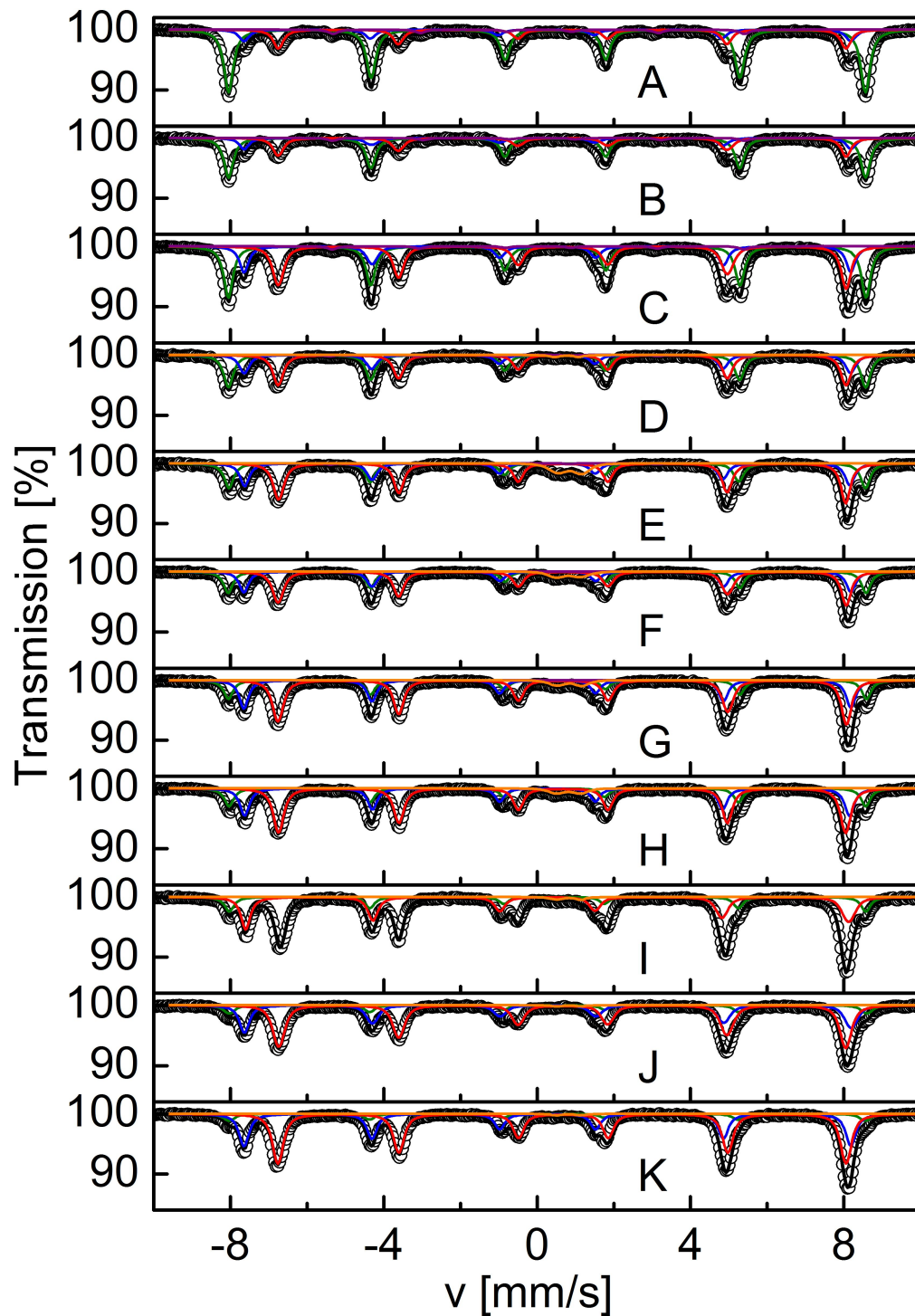


Figure C.9: Mössbauer spectra of post-sintered composites sintered at A) 450°C, B) 500°C, C) 550°C, D) 600°C, E) 650°C, F) 700°C, G) 750°C, H) 800°C, I) 850°C, J) 900°C and K) 950°C. The experimental data are presented in open dots, the calculated spectra with a black line and the contributing subspectra in colour. Blue - magnetite A-sites, red - magnetite B-sites, green - hematite, purple - iron and orange - wustite.

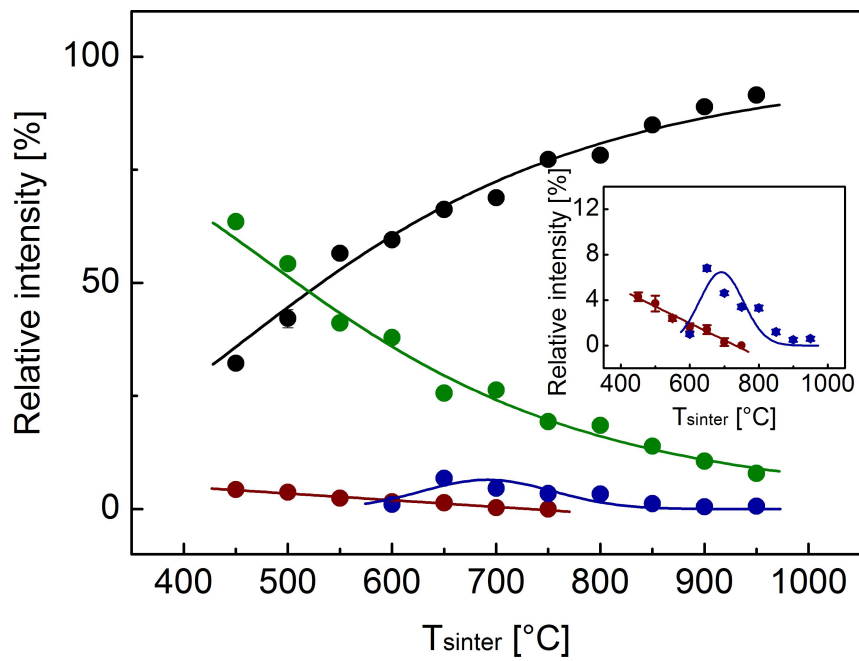


Figure C.10: Relative intensities of the contributing phase, magnetite (black), hematite (green), iron (red) and wustite (blue) in dependence of the sintering temperature T_{sinter} for the post-sintered composites from hematite and iron precursor powders.

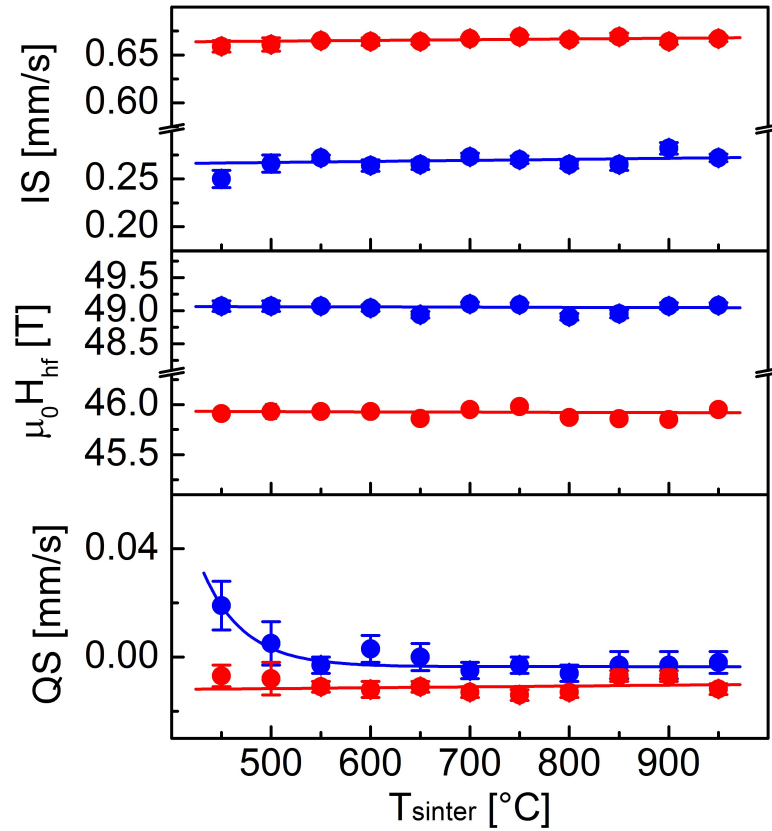


Figure C.12: Calculated mean values of the hyperfine parameters in dependence of the sintering temperature T_{sinter} for the post-sintered composites from hematite and iron precursor powders. IS - isomer shift, $\mu_0 H_{hf}$ - magnetic hyperfine field and QS - quadrupole splitting. Hyperfine parameters for magnetite A-sites are presented in blue and magnetite B-sites in red.

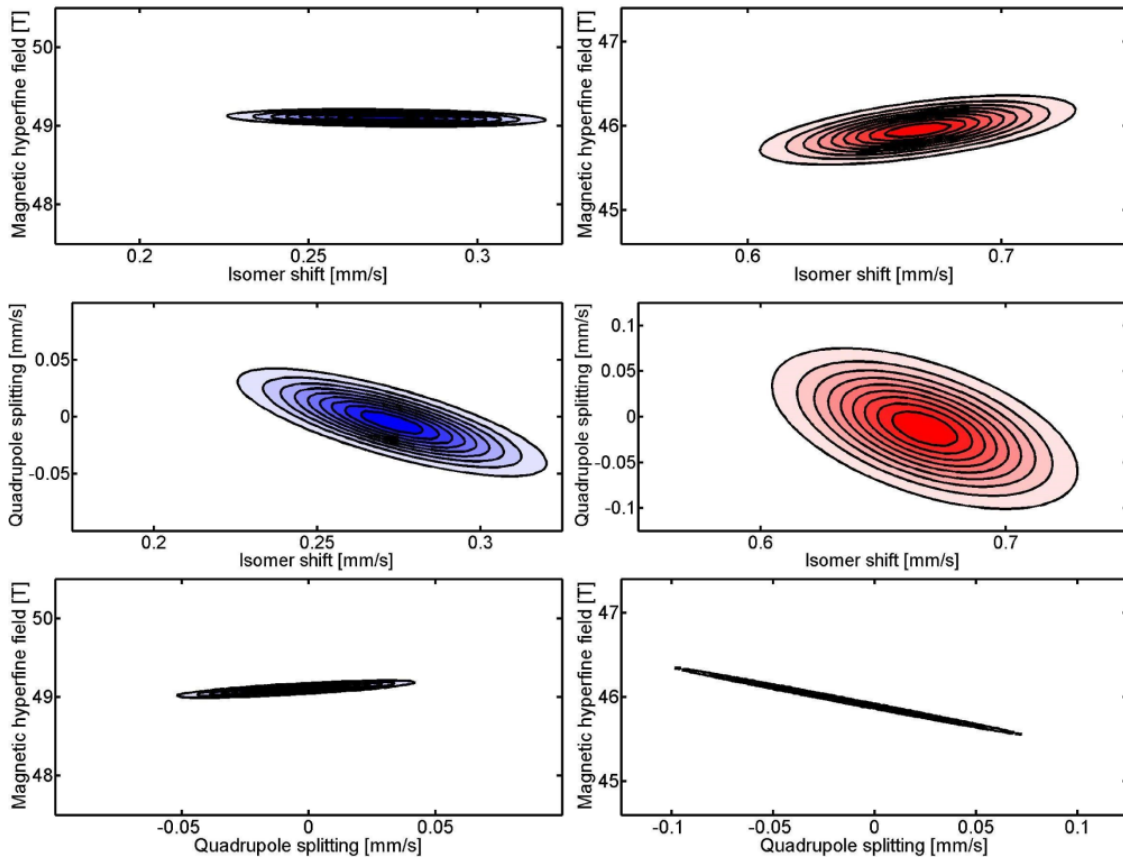


Figure C.13: Maps of the probability density distributions as 2D projections of isomer shift and magnetic hyperfine field (top), isomer shift and quadrupole splitting (middle) and quadrupole splitting and magnetic hyperfine field (bottom) for the post-sintered sample from hematite and iron precursor sintered at 700°C. Left column: magnetite A-sites, right column: magnetite B-sites.

Appendix D

Composites sintered from magnetite precursor

D.1 Initial particle size $d = 120$ nm

Fig. D.1 shows exemplary SEM images of breaking edges of all composites sintered from magnetite precursor powders with an initial particles size of 120 nm. With an increasing sintering temperature also a direct increase of the mean grain size can be observed. Additionally, more necks are formed between the separate grains.

Fig. D.2 shows the diffractograms of all sintered composites. For each sample additionally the calculated pattern and the differential pattern are shown. Below the diffractograms the Bragg reflexes of magnetite and hematite are presented. It is worth to mention that additional reflexes in the diffractograms do not belong to an additional phase present in the sample but to magnetite and hematite.

Fig. D.3 shows the Mößbauer spectra of all post-sintered composites from this series. Additionally the calculated spectrum and the contributing subspectra are shown for every sample.

Fig. D.4 presents the calculated relative intensities derived from the Mößbauer spectra. The calculated relative intensities from the Mößbauer spectra are in good agreement with the calculated volume fractions from Rietveld refinement procedures. Magnetite phase has a small tendency to increase with increasing sintering temperature, while the hematite phase is decreasing. This behaviour can be described by linear functions. The relative intensity of magnetite subspectra can be described by $f_M = (65.89 + 0.0048 \cdot T_{sinter}/K)$ % and the relative intensity of hematite phase $f_H = (34.11 - 0.0048 \cdot T_{sinter}/K)$ %.

D.2 Initial particle size $d = 27$ nm

Fig. D.5 shows exemplary SEM images of breaking edges of composites sintered from magnetite precursor powders with an initial particles size of 27 nm. With an increasing sintering temperature also a direct increase of the mean grain size can be observed. Additionally, more necks are formed between the separate grains. It is worth to point out that an exemplary SEM image from the post-sintered composite sintered at 700°C is not shown due to editorial reasons.

Fig. D.6 shows the diffractograms of all sintered composites from the magnetite precursor with $d_i = 27$ nm. For each composite additionally the calculated pattern and the differential pattern is presented. Below the diffractograms the Bragg reflexes of

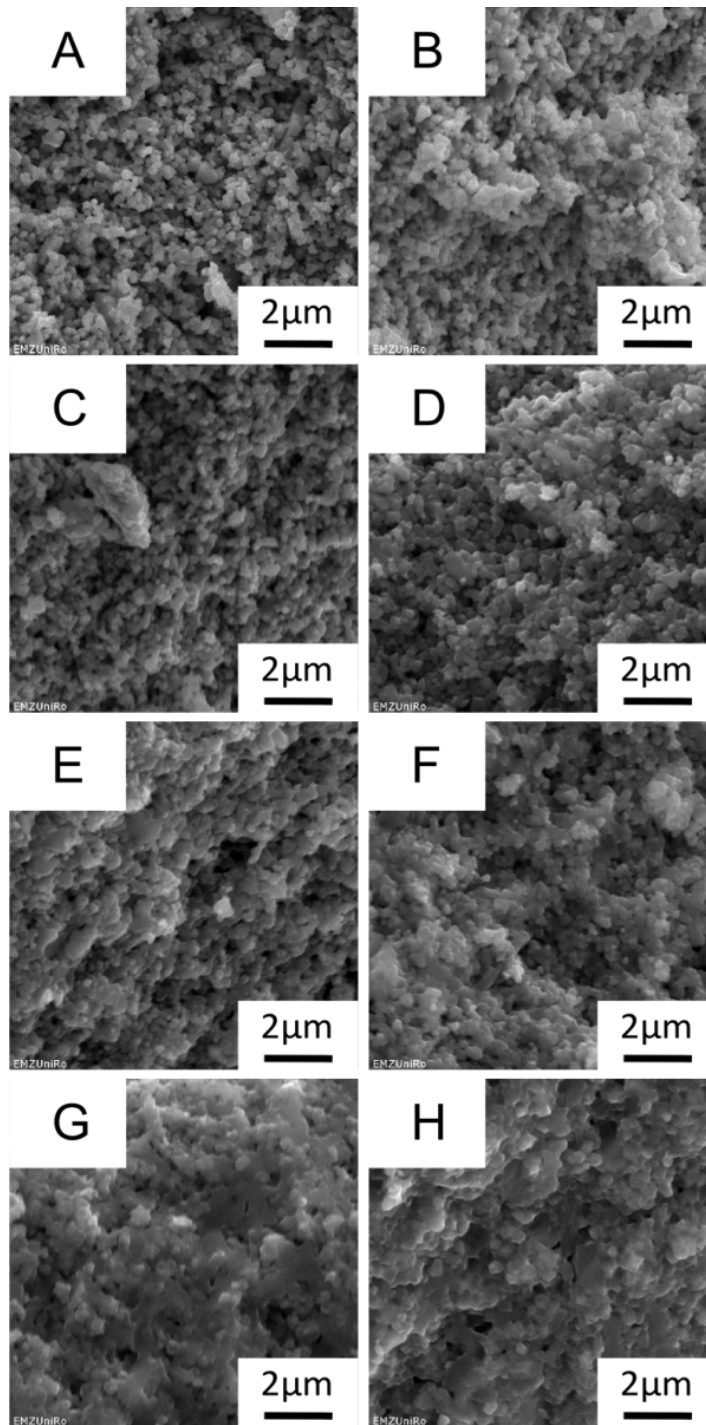


Figure D.1: Exemplary SEM images of breaking edges of post-sintered composites from magnetite precursor powders sintered at A) 600°C, B) 650°C, C) 700°C, D) 750°C, E) 800°C, F) 850°C, G) 900°C and H) 950°C.

magnetite and hematite are to be seen. It is worth to mention that additional reflexes in the diffractograms do not belong to an additional phase present in the sample but belong to magnetite and hematite.

Fig. D.7 shows the Mößbauer spectra of all post-sintered composites from the series sintered from magnetite precursor with $d_i = 27$ nm. Additionally, the calculated spectrum

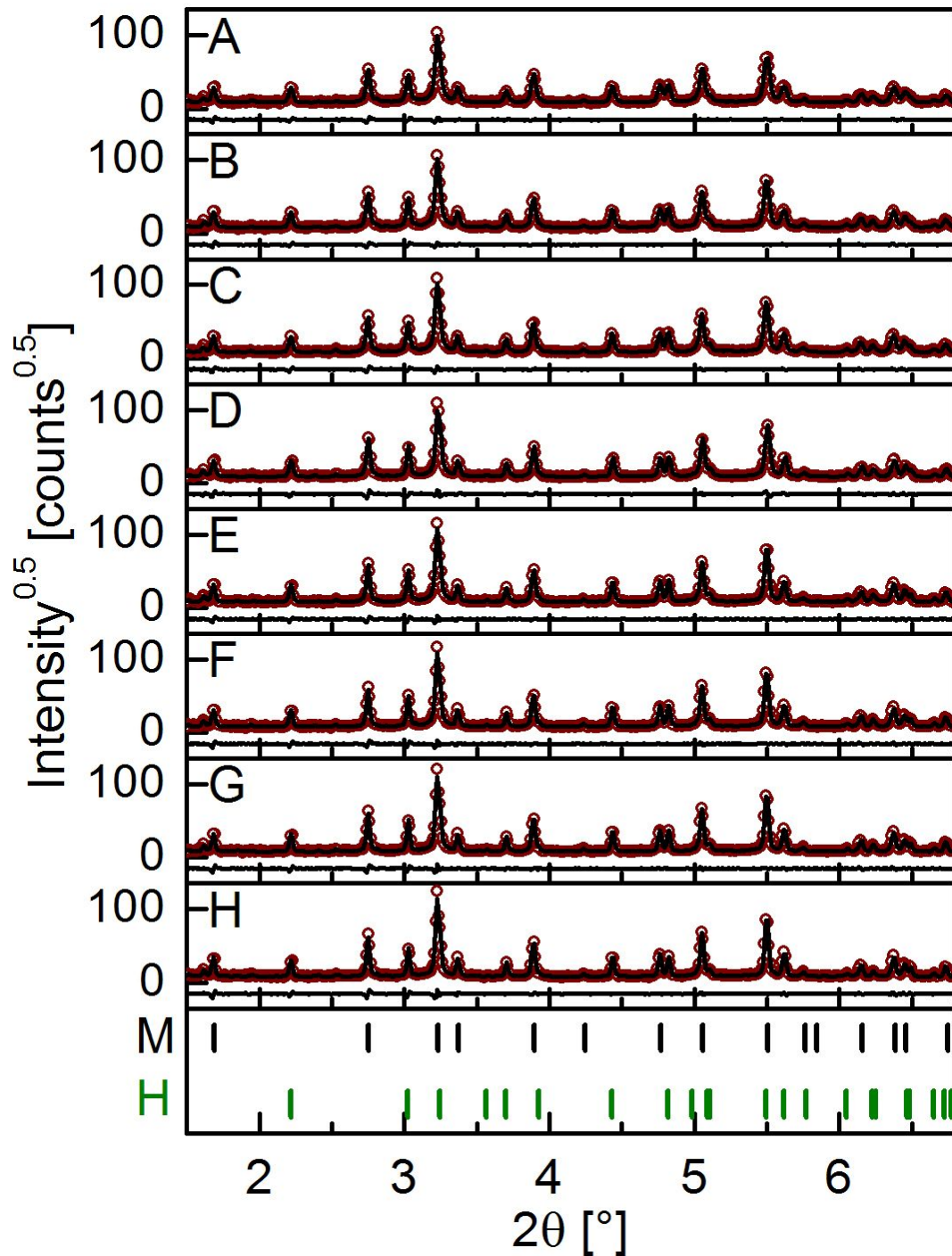


Figure D.2: High energy X-ray diffractograms of post-sintered composites from magnetite precursor powders sintered at A) 600°C, B) 650°C, C) 700°C, D) 750°C, E) 800°C, E) 850°C, F) 900°C and G) 950°C. For each diffractogram additionally the calculated and the differential pattern are shown. Below the diffractograms the Bragg positions of magnetite (M) and hematite (H) are presented.

and the contributing subspectra are shown for each composite.

Fig. D.8 presents the calculated relative intensities derived from the Mößbauer spectra. The resulting relative intensities are comparable to the derived volume fractions of

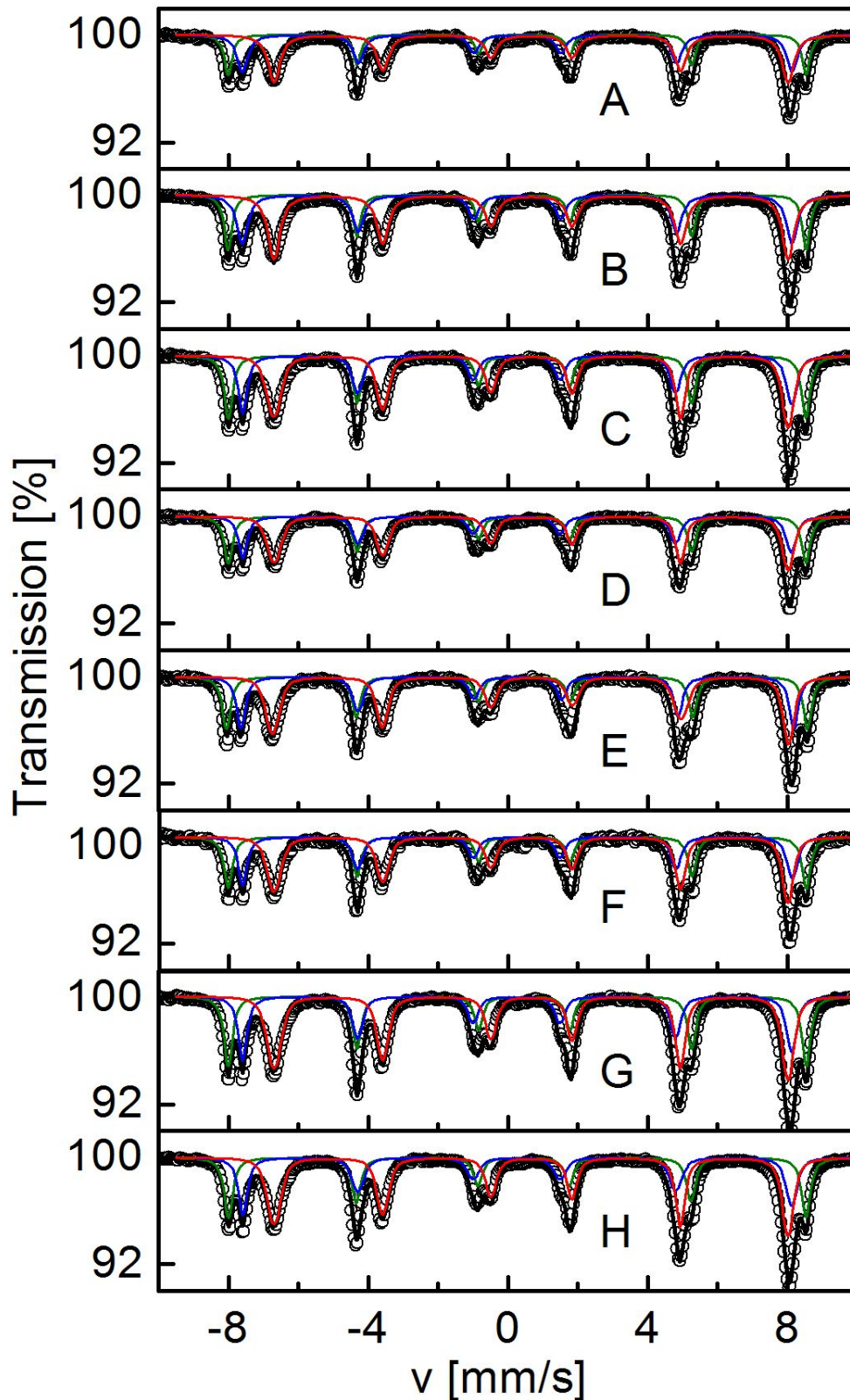


Figure D.3: Mössbauer spectra of post-sintered composites sintered at A) 600°C, B) 650°C, C) 700°C, D) 750°C, E) 800°C, E) 850°C, F) 900°C and G) 950°C. The experimental data are presented in open dots, the calculated spectra with a black line and the contributing subspectra in colour. Blue - magnetite A-sites, red - magnetite B-sites and green - hematite.

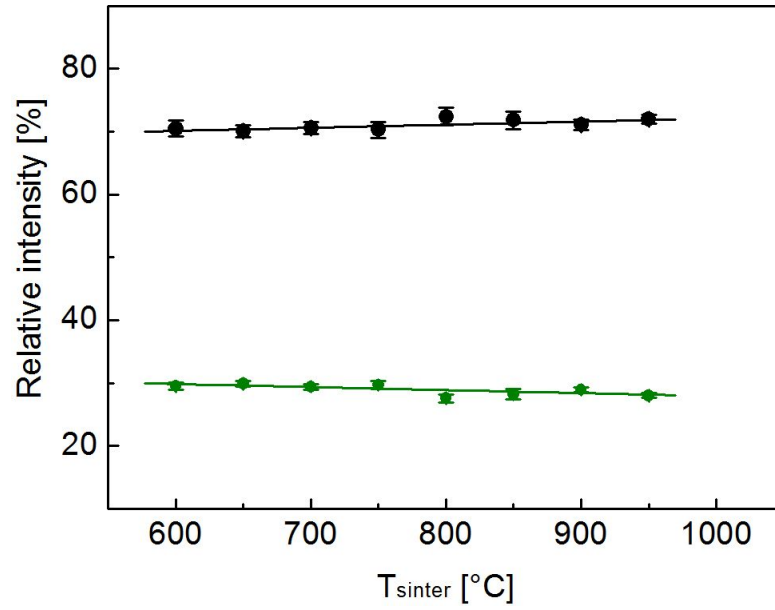


Figure D.4: Relative intensities of the contributing phase, magnetite (black) and hematite (green) in dependence of the sintering temperature T_{sinter} for the post-sintered composites from magnetite precursor powders.

magnetite and hematite from high energy X-ray diffraction.

The relative intensity of magnetite in dependence of the sintering temperature can be described by a linear function $f_M = (22.335 + 0.00789 \cdot T_{sinter}/K)\%$. The behaviour of hematite can be described by $f_H = (77.825 - 0.00789 \cdot T_{sinter}/K)\%$

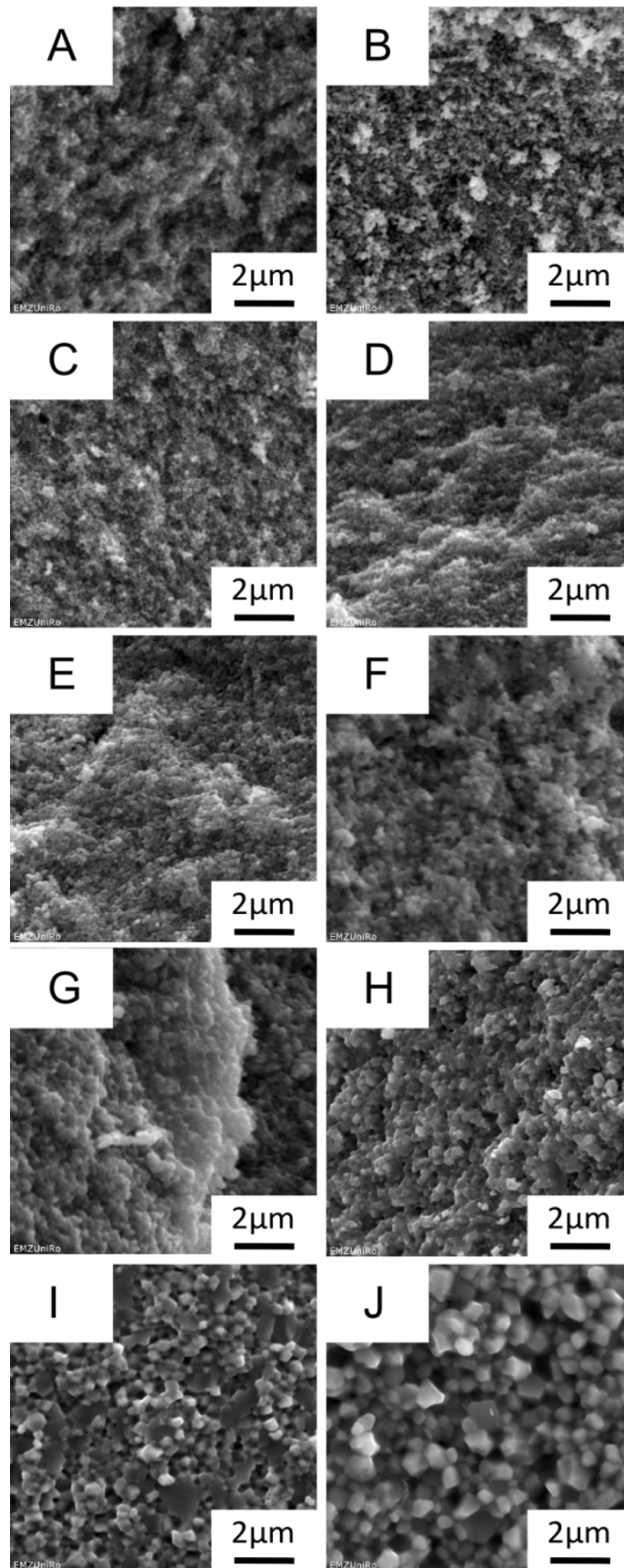


Figure D.5: Exemplary SEM images of breaking edges of post-sintered composites from magnetite precursor powders sintered at A) 450°C, B) 500°C, C) 550°C, D) 600°C, E) 650°C, F) 750°C, G) 800°C, H) 850°C, I) 900°C and J) 950°C.

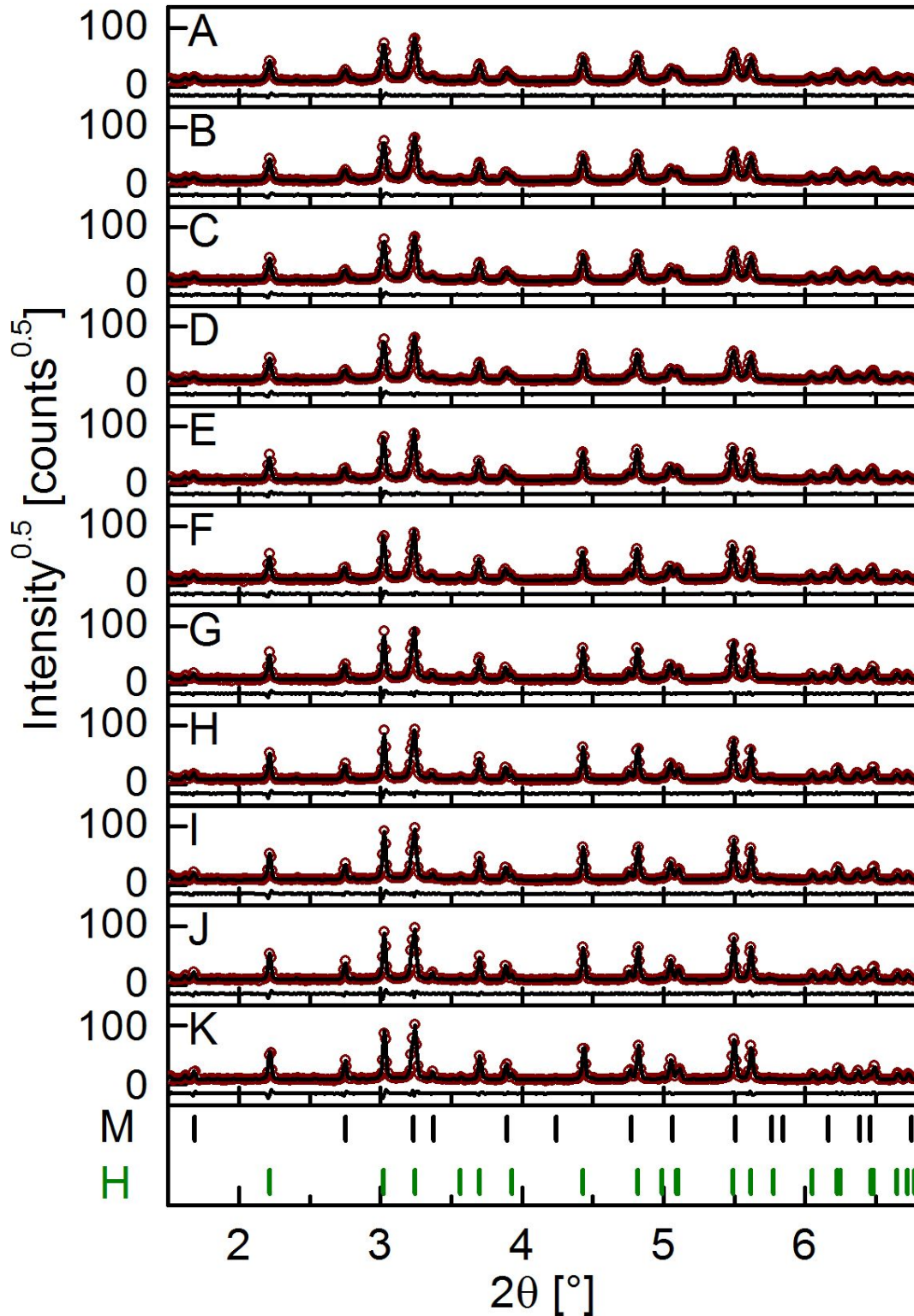


Figure D.6: High energy X-ray diffractograms of post-sintered composites from magnetite precursor powders sintered at A) 450°C, B) 500°C, C) 550°C, D) 600°C, E) 650°C, F) 700°C, G) 750°C, H) 800°C, I) 850°C, J) 900°C and K) 950°C. For each diffractogram additionally the calculated and the differential pattern are shown. Below the diffractograms the Bragg positions of magnetite (M) and hematite (H) are presented.

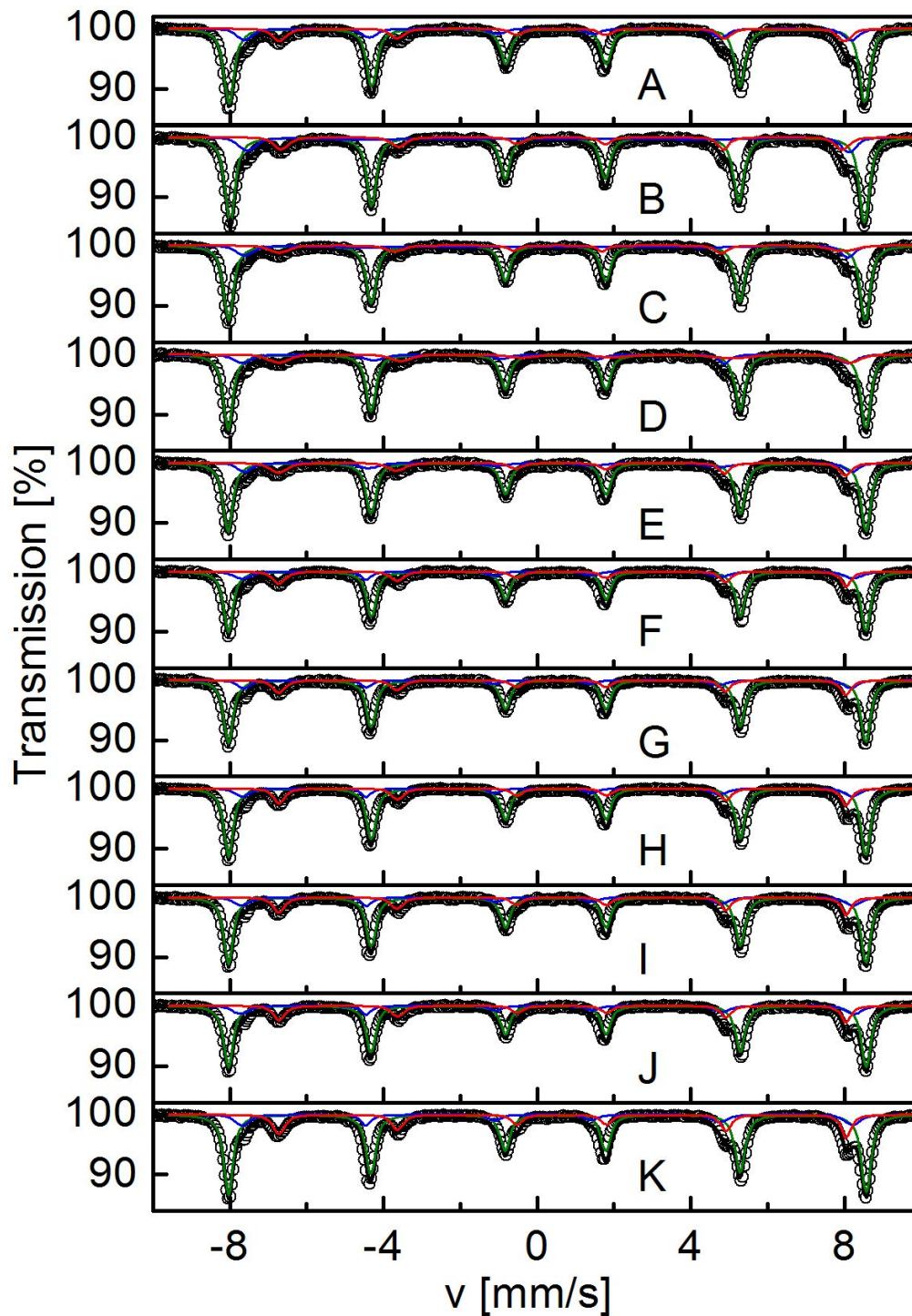


Figure D.7: Mössbauer spectra of post-sintered composites sintered at A) 450°C, B) 500°C, C) 550°C, D) 600°C, E) 650°C, F) 700°C, G) 750°C, H) 800°C, I) 850°C, J) 900°C and K) 950°C. The experimental data are presented in open dots, the calculated spectra with a black line and the contributing subspectra in colour. Blue - magnetite A-sites, red - magnetite B-sites and green - hematite.

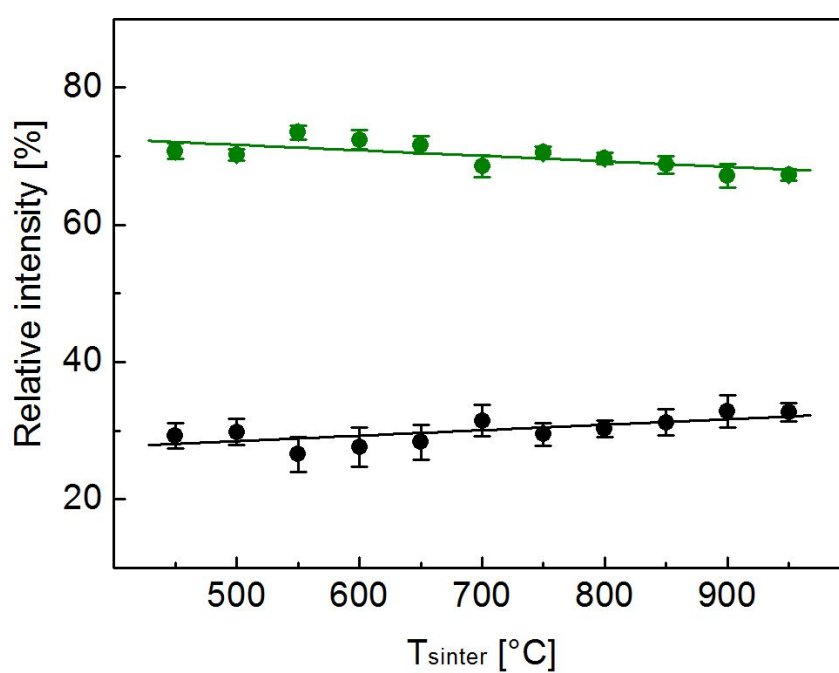


Figure D.8: Relative intensities of the contributing phase, magnetite (black) and hematite (green) in dependence of the sintering temperature T_{sinter} for the post-sintered composites from magnetite precursor powders.

Bibliography

- [1] G. Hadjipanayis, “Nanophase hard magnets,” *Journal of Magnetism and Magnetic Materials*, vol. 200, p. 373, 1999.
 - [2] M. Colombo, S. Carregal-Romero, M. Casula, L. Gutierrez, M. Morales, I. Böhm, J. Heverhagen, D. Rosperi, and W. Parak, “Biological applications of magnetic nanoparticles,” *Chemical Society Reviews*, vol. 41, p. 4306, 2012.
 - [3] Q. Pankhurst, “The magnetism of fine particle iron oxides and oxyhydroxides in applied fields,” *Hyperfine Interactions*, vol. 90, p. 201, 1994.
 - [4] C. Bean and J. Livingston, “Superparamagnetism,” *Journal of Applied Physics*, vol. 30, p. 120, 1959.
 - [5] A. Fert, P. Grünberg, A. Barthelemy, F. Petroff, and W. Zinn, “Layered magnetic structures: interlayer exchange coupling and giant magnetoresistance,” *Journal of Magnetism and Magnetic Materials*, vol. 140-144, p. 1, 1995.
 - [6] R. Skomski and J. Coey, “Giant energy product in nanostructured two-phase magnets,” *Physical Review B*, vol. 48, p. 15812, 1993.
 - [7] K. Witte, K. Porath, and E. Burkel, “Magnetic nanoparticles and their potential for contrast enhancement in magnetic resonance imaging,” *Journal of Spintronics and Magnetic Nanomaterials*, vol. 1, p. 40, 2012.
 - [8] J. E. Garay, “Current-activated, pressure-assisted densification of materials,” *Annual Review of Materials Research*, vol. 40, p. 445, 2010.
 - [9] R. Orru, R. Licheri, A. Locci, A. Cincotti, and G. Cao, “Consolidation/synthesis of materials by electric current activated/assisted sintering,” *Materials Science and Engineering: R: Reports*, vol. 63, p. 127, 2009.
 - [10] J. Morales, J. Garay, M. Biasini, and W. Beyermann, “Magnetic characterization of bulk nanostructured iron oxides,” *Applied Physics Letters*, vol. 93, p. 022511, 2008.
 - [11] J. Alaniz, J. Morales, and J. Garay, “The current activated pressure assisted densification technique for producing nanocrystalline materials,” *The Member Journal of The Minerals, Metals and Materials Society*, p. 58, 2010.
 - [12] J. Morales, S. Tanju, W. Beyermann, and J. Garay, “Exchange bias in large three dimensional iron oxide nanocomposites,” *Applied Physics Letters*, vol. 96, p. 013102, 2010.
-

-
- [13] P. Saravanan, J.-H. Hsu, D. Sivaprahasam, and S. Kamat, "Structural and magnetic properties of γ - Fe_2O_3 nanostructured compacts processed by spark plasma sintering," *Journal of Magnetism and Magnetic Materials*, vol. 346, p. 175, 2013.
- [14] C. Fei, Y. Zhang, Z. Yang, Y. Liu, R. Xiong, J. Shi, and X. Ruand, "Synthesis and magnetic properties of hard magnetic (CoFe_2O_4)-soft magnetic (Fe_3O_4) nanocomposite ceramics by sps technology," *Journal of Magnetism and Magnetic Materials*, vol. 323, p. 1811, 2011.
- [15] Y. Yoshida and G. Langouche, eds., *Mössbauer spectroscopy*. Springer Verlag Berlin Heidelberg, 2013.
- [16] R. Cornell and U. Schwertmann, *The iron oxides - structure, properties, reactions, occurrence and uses*. VCH: New York, 1996.
- [17] E. Maslen, V. Streltsov, N. Streltsova, and N. Ishizawa, "Synchrotron x-ray study of the electron density in α - Fe_2O_3 ," *Acta Crystallographica Section B*, vol. 50(4), p. 435, 1994.
- [18] V. Montoro, "Miscibilità fra gli ossidi salini di ferro e di manganese," *Gazzetta Chimica Italiana*, vol. 68, p. 728, 1938.
- [19] E. Jette and F. Foote, "An x-ray study of the wuestite (feo) solid solutions," *Journal of Chemical Physics*, vol. 1, p. 29, 1933.
- [20] E. Owen and G. Williams, "A low-temperature x-ray camera," *Journal of Scientific Instruments*, vol. 31, p. 49, 1954.
- [21] E. Verwey and P. Haayman, "Electronic conductivity and transition point of magnetite (" Fe_3O_4 ")," *Physica*, vol. 8, p. 979, 1941.
- [22] C. Gorski and M. Scherer, "Determination of nanoparticulate magnetite stoichiometry by Mössbauer spectroscopy, acidic dissolution, and powder x-ray diffraction: A critical review," *American Mineralogist*, vol. 95, p. 1017, 2010.
- [23] E. Schmidbauer and M. Keller, "Magnetic hysteresis properties, Mössbauer spectra and structural data of spherical 250nm particles of solid solutions Fe_3O_4 - γ - Fe_2O_3 ," *Journal of Magnetism and Magnetic Materials*, vol. 297, p. 107, 2006.
- [24] K. Volenik, M. Seberini, and J. Neid, "A Mössbauer and x-ray diffraction study of nonstoichiometry in magnetite," *Czech Journal of Physics B*, vol. 25, p. 1063, 1975.
- [25] R. Castro and K. van Benthem, eds., *Sintering; Mechanism of convention, nanodensification and field assisted process*. Springer Verlag Berlin Heidelberg, 2013.
- [26] Z. Munir, U. Anselmi-Tamburini, and M. Ohyanagi, "The process of electric field and pressure on the synthesis and consolidation of materials: a review of the spark plasma sintering method," *Journal of Material Science*, vol. 41, p. 763, 2006.
-

- [27] Z. A. Munir, D. V. Quach, and M. Ohyanagi, "Electric current activation of sintering: a review of the pulsed electric sintering process," *Journal of American Ceramic Society*, vol. 94, pp. 1–19, 2011.
- [28] S. Munoz and U. Anselmi-Tamburini, "Temperature and stress field evolution during spark plasma sintering process," *Journal of Material Science*, vol. 45, p. 6528, 2010.
- [29] J. M. Frei, U. Anselmi-Tamburini, and Z. A. Munir, "Current effects on neck growth in the sintering of copper spheres to copper plates by the pulsed electric current method," *Journal of applied physics*, vol. 101, p. 114914, 2007.
- [30] D. Hulbert, A. Anders, D. Dudina, J. Andersson, D. Jiang, C. Unuvar, U. Anselmi-Tamburini, E. Lavernia, and A. Mukherjee, "The absence of plasma in spark plasma sintering," *Journal of Applied Physics*, vol. 104, p. 0333050, 2008.
- [31] K. Mackenzie and M. Ryan, "Effect of electric fields on solid-state reactions between oxides," *Journal of Material Science*, vol. 16, p. 579, 1981.
- [32] J. Jeong, J. Han, and D. Kim, "Effect of electric field on the migration of grain boundaries in alumina," *Journal of American Ceramic Society*, vol. 83, p. 915, 2000.
- [33] D. Quach, H. Avila-Paredes, S. Kim, M. Martin, and Z. Munir, "Pressure effects and grain growth kinetics in the consolidation of nanostructured fully stabilized zirconia by pulsed electric current sintering," *Acta Materialia*, vol. 58, p. 5022, 2010.
- [34] K. Smith and C. Oatley, "The scanning electron microscope and its fields of applications," *British Journal of Applied Physics*, vol. 6, p. 391, 1955.
- [35] R. Pease and W. Nixon, "High resolution scanning electron microscopy," *Journal of Scientific Instruments*, vol. 42, p. 81, 1965.
- [36] L. Reimer, *Scanning electron microscopy - Physics of image formation and microanalysis*. Springer Verlag Berlin Heidelberg, 1985.
- [37] H. Seiler, "Secondary electron emission in the scanning electron microscope," *Journal of Applied Physics*, vol. 54, p. R1, 1983.
- [38] E. Burkel, "Introduction to x-ray scattering," *Journal of Physics: Condensed Matter*, vol. 13, p. 7477, 2001.
- [39] L. van Hove, "Correlations in space and time and born approximation scattering in systems of interacting particles," *Physical Review*, vol. 95, p. 249, 1954.
- [40] E. Lifshin, ed., *X-ray characterization of materials*. Wiley-VHC, 1999.
- [41] W. Bragg and W. Bragg, "The reflection of x-rays by crystals," *Proceedings of the Royal Society of London Series A*, vol. 88, p. 428, 1913.
-

-
- [42] M. von Laue, *Röntgenstrahlinterferenzen*. Akademische Verlagsgesellschaft Frankfurt am Main, 1960.
- [43] H. M. Rietveld, "A profile refinement method for nuclear and magnetic structures," *Journal of Applied Crystallography*, vol. 2, p. 65, 1969.
- [44] H. Rietveld, "Line profiles of neutron powder-diffraction peaks for structure refinement," *Acta Crystallographica*, vol. 22, p. 151, 1967.
- [45] L. Lutterotti and S. Gialanella, "X-ray diffraction characterization of heavily deformed metallic specimens," *Acta Materialia*, vol. 46, p. 101, 1998.
- [46] L. Lutterotti, P. Scardi, and P. Maistrelli, "Ls1 - a computer program for simultaneous refinement of material structure and microstructure," *Journal of Applied Crystallography*, vol. 25, p. 459, 1992.
- [47] L. Lutterotti and P. Scardi, "Simultaneous structure and size-strain refinement by the rietveld method," *Journal of Applied Crystallography*, vol. 23, p. 246, 1990.
- [48] G. Caglioti, A. Paoletti, and F. Ricci, "Choice of collimators for a crystal spectrometer for neutron diffraction," *Nuclear Instruments*, vol. 3, p. 223, 1958.
- [49] P. Scardi, L. Lutterotti, R. D. Maggio, and P. Maistrelli, "Influence of crystallite size and microstrain on structure refinement," *Material Science Forum*, vol. 79, p. 233, 1991.
- [50] R. Nandi, H. Kuo, W. Schlosberg, G. Wissler, J. Cohen, and B. Crist, "Single-peak methods for fourier analysis of peak shapes," *Journal of Applied Crystallography*, vol. 17, p. 22, 1984.
- [51] N. Schell, A. King, F. Beckmann, H. U. Ruhnau, R. Kirchhof, R. Kiehn, M. Müller, and A. Schreyer, "The high energy materials science beamline at petra iii," *AIP Conference Proceeding*, vol. 1234, p. 391, 2010.
- [52] N. Schell, A. King, F. Beckmann, T. Fischer, M. Müller, and A. Schreyer, "The high energy materials science beamline at petra iii," *Material Science Forum*, vol. 772, p. 57, 2014.
- [53] L. Lutterotti, M. Bortolotti, G. Ischia, I. Lonardelli, and H. Wenk, "Rietveld texture analysis from diffraction images," *Zeitschrift für Kristallographie Supplements*, vol. 2007, p. 125, 2007.
- [54] L. Lutterotti, S. Matthies, H. Wenk, A. Schultz, and J. Richardson, "Combined texture and structure analysis of deformed limestone from time-of-flight neutron diffraction spectra," *Journal of Applied Physics*, vol. 81, p. 594, 1997.
- [55] L. McCusker, R. von Dreele, D. Cox, D. Louer, and P. Scardi, "Rietveld refinement guidelines," *Journal of Applied Crystallography*, vol. 32, p. 36, 1999.
-

- [56] Y. Chen and D. Yang, *Mössbauer effect in lattice dynamics - experimental techniques and applications*. Wiley-VHC, 2007.
- [57] D. Barb, *Grundlagen und Anwendungen der Mössbauerspektroskopie*. Akademie-Verlag Berlin, 1980.
- [58] N. Greenwood and T. Gibb, *Mössbauer Spectroscopy*. Chapman and Hall Ltd London, 1971.
- [59] R. Mößbauer, “Kernresonanzfluoreszenz von gammastrahlung in ir^{191} ,” *Zeitschrift für Physik*, vol. 151, p. 124, 1958.
- [60] W. Lamb, “Capture of neutrons by atoms in a crystal,” *Physical Review*, vol. 55, p. 190, 1939.
- [61] C. Kittel, *Einführung in die Festkörperphysik*. Oldenburg Verlag, 2013.
- [62] P. Gütlich, E. Bill, and A. Trautwein, *Mössbauer spectroscopy and transition metal chemistry - Fundamentals and applications*. Springer Heidelberg Dordrecht London New York, 2011.
- [63] G. Martínez-Pinedo, P. Schwerdtfeger, E. Caurier, K. Langanke, W. Nazarewicz, and T. Söhnel, “Nuclear quadrupole moment of ^{57}Fe from microscopic nuclear and atomic calculations,” *Physical review letters*, vol. 87, p. 062701, 2001.
- [64] G. Breit, “Theory of isotope shift,” *Reviews of Modern Physics*, vol. 30, p. 507, 1958.
- [65] A. Freeman and R. Watson, “Antishielding of magnetic and electric hyperfine interactions in open shell ions,” *Physical Review*, vol. 131, p. 2566, 1963.
- [66] G. da Costa, E. de Grave, P. de Bakker, and R. Vandenberghe, “Influence of nonstoichiometry and the presence of maghemite on the mössbauer spectrum of magnetite,” *Clays and Clay Minerals*, vol. 43, p. 656, 1995.
- [67] J. Daniels and A. Rosencwaig, “Mössbauer spectroscopy of stoichiometric and non-stoichiometric magnetite,” *Journal of Physics and Chemistry of Solids*, vol. 30, p. 1561, 1969.
- [68] J. Cullen and E. Callen, “Collective electron theory of metal-semiconductor transition in magnetite,” *Journal of Applied Physics*, vol. 41, p. 879, 1970.
- [69] D. Ihle and B. Lorenz, “Small-polaron band versus hopping conduction in Fe_3O_4 ,” *Journal of Physics C: Solid State Physics*, vol. 18, p. L647, 1985.
- [70] N. Popa, “The (hkl) dependence of diffraction-line broadening caused by strain and size for all laue groups in rietveld refinement,” *Journal of Applied Crystallography*, vol. 31, p. 176, 1998.
-

-
- [71] D. Rancourt, "Mössbauer spectroscopy in clay science," *Hyperfine Interactions*, vol. 117, p. 3, 1998.
- [72] K. Lagarec and D. G. Rancourt, *Recoil: Mössbauer spectral analysis software for windows*, 1998.
- [73] E. Murad, "Magnetic properties of microcrystalline iron(iii) oxides and related materials as reflected in their mössbauer spectra," *Physics and chemistry of minerals*, vol. 23, p. 248, 1996.
- [74] M. Blume and J. Tjon, "Mössbauer spectra in a fluctuating environment," *Physical Review*, vol. 165, p. 446, 1967.
- [75] S. Mørup and H. Topsøe, "Mössbauer studies of thermal excitations in magnetically ordered microcrystals," *Applied Physics*, vol. 11, p. 63, 1967.
- [76] S. Mørup, H. Topsøe, and J. Lipka, "Modified theory for mössbauer spectra of superparamagnetic particles: Application to Fe_3O_4 ," *Le Journal de Physique Colloques*, vol. 37, pp. C6–287, 1976.
- [77] D. Rancourt and J. Ping, "Voigt-based methods for arbitrary-shape static hyperfine parameter distributions in mössbauer spectroscopy," *Nuclear Instruments and Methodes in Physics Research B*, vol. 58, p. 85, 1991.
- [78] J. Puerta and P. Martin, "Three and four generalized lorentzian approximations for the voigt line shape," *Applied Optics*, vol. 20, p. 3923, 1981.
- [79] K. Lagarec and D. Rancourt, "Extended voigt-based analytic lineshape method for determining n-dimensional correlated hyperfine parameter distributions in mössbauer spectroscopy," *Nuclear Instruments and Methodes in Physics Research B*, vol. 129, p. 266, 1997.
- [80] E. Tronc, "Nanoparticles," *II nuovo Cimento D*, vol. 18, p. 163, 1996.
- [81] T. McNab, R. Fox, and A. Boyle, "Some magnetic properties of magnetite (Fe_3O_4) microcrystals," *Journal of Applied Physics*, vol. 39, p. 5703, 1968.
- [82] A. Hartridge, A. Bhattacharya, M. Sengupta, C. Majumdar, D. Das, and S. Chitalapudi, "Crystallite size dependence on the magnetic poperties of nanocrystalline magnetite powders," *Journal of Magnetism and Magnetic Materials*, vol. 176, p. L89, 1997.
- [83] C. Frandsen and S. Mørup, "Inter-particle interactions in composites of antiferromagnetic nanoparticles," *Journal of Magnetism and Magnetic Materials*, vol. 266, p. 36, 2003.
- [84] L. Häggström, H. Annersten, T. Ericsson, R. Wäppling, W. Karner, and S. Bjarman, "Magnetic dipolar and electric quadrupolar effects on the mössbauer spectra of magnetite above the verwey transistion," *Hyperfine Interactions*, vol. 5, p. 201, 1978.
-

- [85] D. Herea, H. Chiriac, and N. Lupu, "Preparation and characterization of magnetic nanoparticles with controlled magnetization," *Journal of Nanoparticle Research*, vol. 13, p. 4357, 2011.
- [86] R. Vandenberghe, C. Barrero, G. D. Costa, E. V. San, and E. D. Grave, "Mössbauer characterization of iron oxides and (oxy)hydroxides: the present state of the art," *Hyperfine Interactions*, vol. 126, p. 247, 2000.
- [87] S. Mørup, C. Frandsen, and M. Hansen, "Uniform excitations in magnetic nanoparticles," *Beilstein Journal of Nanotechnology*, vol. 1, p. 48, 2010.
- [88] R. Vandenberghe, I. Nedkov, T. Merodiiska, and L. Slavov, "Surface oxidation control of nanosized magnetite and mössbauer measurements," *Hyperfine Interactions*, vol. 165, p. 267, 2005.
- [89] J. Mürbe, A. Rechtenbach, and J. Töpfer, "Synthesis and physical characterization of magnetite nanoparticles for biomedical applications," *Materials Chemistry and Physics*, vol. 110, p. 426, 2008.
- [90] A. Roca, J. Marco, M. Morales, and C. Serna, "Effect of nature and particle size on properties of uniform magnetite and maghemite nanoparticles," *The Journal of Physical Chemistry C*, vol. 111, p. 18577, 2007.
- [91] P. Tartaj, M. Morales, S. Veintemillas-Verdaguer, T. Gonzalez-Carreno, and C. Serna, "The preparation of magnetic nanoparticles for applications in biomedicine," *Journal of Applied Physics D: Applied Physics*, vol. 36, p. R182, 2003.
- [92] P. Tartaj, M. Morales, T. Gonzalez-Carreno, S. Veintemillas-Verdaguer, and C. Serna, "The iron oxides strike back: from biomedical applications to energy storage devices and photoelectrochemical water splitting," *Advanced Materials*, vol. 2011, p. 5243, 2011.
- [93] H. Reddy, J. Arias, J. Nicolas, and P. Couvreur, "Magnetic nanoparticles: design and characterization, toxicity and biocompatibility, pharmaceutical and biomedical applications," *Chemical Reviews*, vol. 112, p. 5818, 2012.
- [94] A. Akbarzadeh, M. Samiei, and S. Davaran, "Magnetic nanoparticles: preparation, physical properties, and applications in biomedicine," *Nanoscale Research Letters*, vol. 7, p. 144, 2012.
- [95] M. Willard, L. Kurihara, E. Carpenter, S. Calvin, and V. Harris, "Chemically prepared magnetic nanoparticles," *International Materials Reviews*, vol. 49, p. 125, 2004.
- [96] S. Mørup, "Mössbauer effect in small particles," *Hyperfine Interactions*, vol. 60, p. 959, 1990.
-

- [97] I. Nedkov, E. Vandenberghe, G. Vissokov, T. M. M. Kolev, and K. Krezhov, "Phase and structural particularities of nanosized granular inverse spinels," *Physica status solidi (a)*, vol. 201, p. 1001, 2004.
- [98] L. T. Kuhn, A. Bojesen, L. Timmermann, K. Fauth, E. Goering, E. Johnson, M. M. Nielsen, and S. Morup, "Core-shell iron-iron oxide nanoparticles: magnetic properties and interactions," *Journal of Magnetism and Magnetic Materials*, vol. 272-276, p. 1485, 2004.
- [99] A.-F. Lehlooh and S. Mahmood, "Mössbauer spectroscopy of Fe_3O_4 ultrafine particles," *Journal of Magnetism and Magnetic Materials*, vol. 151, p. 163, 1995.
- [100] P. Roggwiler and W. Kündig, "Mössbauer spectra of superparamagnetic Fe_3O_4 ," *Solid State Communications*, vol. 12, p. 901, 1973.
- [101] M. Darbandi, F. Stromberg, J. Landers, N. Reckers, B. Sanyal, W. Keune, and H. Wende, "Nanoscale size effect on surface spin canting in iron oxide nanoparticles synthesized by the microemulsion method," *Journal of Physics D: Applied Physics*, vol. 45, no. 195001, 2012.
- [102] S. Bid, A. Banerjee, S. Kumar, S. Pradhan, U. De, and D. Banerjee, "Nanophase iron oxides by ball-mill grinding and their mössbauer characterization," *Journal of Alloys and Compounds*, vol. 326, p. 292, 2001.
- [103] M. Jean, V. Nachbaur, and J.-M. L. Breton, "Synthesis and characterization of magnetite powders obtained by solvothermal method: influence of the Fe^{3+} concentration," *Journal of Alloys and Compounds*, vol. 513, p. 425, 2012.
- [104] G. Goya, T. Berquo, and F. Fonseca, "Static and dynamic magnetic properties of spherical magnetite nanoparticles," *Journal of Applied Physics*, vol. 94, no. 3520, 2003.
- [105] J. R. Guivar, A. Bustamante, J. Flores, M. M. Santillan, A. Osorio, A. Martinez, L. D. L. S. Valladares, and C. Barnes, "Mössbauer study of intermediate superparamagnetic relaxation of maghemite ($\gamma\text{-Fe}_2\text{O}_3$) nanoparticles," *Hyperfine Interactions*, vol. 224, p. 89, 2014.
- [106] N. Mahmed, J. Larismaa, O. Heczko, M. Cura, and S.-P. Hannula, "Influence of sintering temperature on the properties of pulsed electric current sintered hybrid coreshell powders," *Journal of the European Ceramic Society*, vol. 33, p. 2232, 2013.
- [107] J. Coey, "Novel permanent magnetic materials," *Physica Scripta*, vol. T39, p. 21, 1991.
- [108] A. Morish, *The physical principles of magnetism*. The Institute of Electrical and Electronics Engineers, New York, 2001.
-

-
- [109] E. Petrovsky, M. Alcalá, J. Criado, T. Grygar, A. Kapicka, and J. Subrt, “Magnetic properties of magnetite prepared by ball-mill of hematite and iron,” *Journal of Magnetism and Magnetic Materials*, vol. 210, p. 257, 2000.
- [110] W. Kaczmarek and B. Ninham, “Preparation of Fe_3O_4 and $\gamma\text{-Fe}_2\text{O}_3$ powders by magnetochemical activation of hematite,” *IEEE Transactions on Magnetics*, vol. 30, p. 732, 1994.
- [111] V. Romanov, L. Checherskaya, and P. Tatsienko, “Peculiarities of wustite formed below 570°C ,” *Physica status solidi (a)*, vol. 15, p. 721, 1973.
- [112] Z. Inglot, D. Wiarda, K. Lieb, T. Wenzel, and M. Uhrmacher, “Defects in Fe_{1-x}O and the $\text{Fe}_{1-x}\text{O} \rightarrow \text{Fe}_3\text{O}_4$ phase transition studied by the perturbed angular correlation method,” *Journal of Physics: Condensed Matter*, vol. 3, p. 4569, 1991.
- [113] R. Weast, S. Selby, and C. Hodgman, eds., *Handbook of chemistry and physics*. The Chemical Rubber Co., 45 ed., 1964.
-

Acknowledgements

First of all I would like to thank Prof. Eberhard Burkel for the possibility to work in the group Physics of New Materials and under his supervision. I am really grateful for his constant support and also the possibility to follow my own ideas for the realisation of projects. Furthermore, I would like to thank Ulrike Schröder. Her encouraging being and the permanent supply with coffee really helped to push this work forward.

I especially would like to thank Dr. Witkor Bodnar. He introduced to me the Mößbauer spectroscopy and for constant support during the PhD study.

Furthermore, I would like to appreciate the support of Dr. Norbert Schell from Helmholtz-Center Geesthacht at the beamline in Hamburg and of Dipl.-Phys. Gerd Fulda from the EMZ University of Rostock for the help at the transmission and scanning electron microscope.

I also would like to thank the whole group Physics of New Materials for the friendly working atmosphere. Especially, I want to thank M. Sc. Rico Schnierer who always had some cheering words in the correct moment.

I would like to thank also Dr. Cordula Grüttner, Dipl.-Phys. Fritz Westphal and all the other members of micromod Partikeltechnology GmbH for the possibility of focusing first on my thesis and for the moral support.

Finally, I am thankful for my family and friends. Their steady support help me to accomplish my goals.

Eidesstattliche Erklärung

Hiermit versichere ich, dass ich die vorliegende Arbeit selbstständig angefertigt und ohne fremde Hilfe verfasst habe, keine außer den von mir angegebenen Hilfsmitteln und Quellen dazu verwendet habe.

Kerstin Witte

23.01.2015, Rostock